2018-06

FAILURE MODEL FOR FIBROUS COMPOSITES USING MULTISCALE MODELING

Darcy, Joseph

Monterey, CA; Naval Postgraduate School

NAVAL POSTGRADUATE SCHOOL

MONTEREY, CALIFORNIA

DISSERTATION

FAILURE MODEL FOR FIBROUS COMPOSITES USING MULTISCALE MODELING

by

Joseph Darcy

June 2018

Dissertation Supervisor: Young W. Kwon

THIS PAGE INTENTIONALLY LEFT BLANK

REPORT DOCUMENTATION PAGE			*Form Approved OMB No. 0704-0188*

1. AGENCY USE ONLY *(Leave blank)*	**2. REPORT DATE** June 2018	**3. REPORT TYPE AND DATES COVERED** Dissertation

4. TITLE AND SUBTITLE FAILURE MODEL FOR FIBROUS COMPOSITES USING MULTISCALE MODELING	**5. FUNDING NUMBERS**
6. AUTHOR(S) Joseph Darcy	
7. PERFORMING ORGANIZATION NAME(S) AND ADDRESS(ES) Naval Postgraduate School Monterey, CA 93943-5000	**8. PERFORMING ORGANIZATION REPORT NUMBER**
9. SPONSORING / MONITORING AGENCY NAME(S) AND ADDRESS(ES) N/A	**10. SPONSORING / MONITORING AGENCY REPORT NUMBER**

11. SUPPLEMENTARY NOTES The views expressed in this thesis are those of the author and do not reflect the official policy or position of the Department of Defense or the U.S. Government.

12a. DISTRIBUTION / AVAILABILITY STATEMENT Approved for public release. Distribution is unlimited.	**12b. DISTRIBUTION CODE** A

13. ABSTRACT (maximum 200 words)

An established multiscale model for materials is used as the basis for a failure model for fiber composites. The model's computation is explained so that its results can be used to formulate the inputs to the failure model. The failure model proposed employs homogenization and disaggregation methods that are enabled by micro-scale modeling of the material's constituents. This failure model is then used to define strength reductions in the composite at the micro-level. The strength reductions enable the definition of a progressive failure methodology for application to the micro-scale, and ultimately, the macro-scale composite. The failure model, the degradation model, and the multi-scale model they are based upon are combined in a computational program for inclusion in finite element software for efficient solving and prediction of intact and failed composite structural response. The model is then tested against existing experimental data as well as by experiments conducted by the author.

14. SUBJECT TERMS composite failure, multiscale composite model, worldwide failure exercise, WWFE, fiber composite, finite element, progressive damage, composite degradation	**15. NUMBER OF PAGES** 141
	16. PRICE CODE

17. SECURITY CLASSIFICATION OF REPORT	**18. SECURITY CLASSIFICATION OF THIS PAGE**	**19. SECURITY CLASSIFICATION OF ABSTRACT**	**20. LIMITATION OF ABSTRACT**
Unclassified	Unclassified	Unclassified	UU

NSN 7540-01-280-5500 Standard Form 298 (Rev. 2-89) Prescribed by ANSI Std. 239-18

THIS PAGE INTENTIONALLY LEFT BLANK

Approved for public release. Distribution is unlimited.

FAILURE MODEL FOR FIBROUS COMPOSITES USING MULTISCALE MODELING

Joseph Darcy
Commander, United States Navy
BS, U.S. Naval Academy, 2001
NavE, Massachusetts Institute of Technology, 2009
MS, Massachusetts Institute of Technology, 2009

Submitted in partial fulfillment of the
requirements for the degree of

DOCTOR OF PHILOSOPHY IN MECHANICAL ENGINEERING

from the

NAVAL POSTGRADUATE SCHOOL
June 2018

Approved by:

Young W. Kwon
Department of Mechanical and Aerospace Engineering
Dissertation Supervisor

Erick S. Alley
Department of Mechanical and Aerospace Engineering

Anthony J. Gannon
Department of Mechanical and Aerospace Engineering

Joshua H. Gordis
Department of Mechanical and Aerospace Engineering

Jeremy E. Kozdon
Department of Applied Mathematics

John Molitoris
Lawrence Livermore National Laboratory

Approved by:

Garth V. Hobson, Chair
Department of Mechanical and Aerospace Engineering

Douglas Moses, Vice Provost of Academic Affairs

THIS PAGE INTENTIONALLY LEFT BLANK

ABSTRACT

An established multiscale model for materials is used as the basis for a failure model for fiber composites. The model's computation is explained so that its results can be used to formulate the inputs to the failure model. The failure model proposed employs homogenization and disaggregation methods that are enabled by micro-scale modeling of the material's constituents. This failure model is then used to define strength reductions in the composite at the micro-level. The strength reductions enable the definition of a progressive failure methodology for application to the micro-scale, and ultimately, the macro-scale composite. The failure model, the degradation model, and the multi-scale model they are based upon are combined in a computational program for inclusion in finite element software for efficient solving and prediction of intact and failed composite structural response. The model is then tested against existing experimental data as well as by experiments conducted by the author.

THIS PAGE INTENTIONALLY LEFT BLANK

Table of Contents

THIS PAGE INTENTIONALLY LEFT BLANK

List of Figures

List of Tables

THIS PAGE INTENTIONALLY LEFT BLANK

List of Acronyms and Abbreviations

BLAS	Basic Linear Algebra Subroutines
DAQ	Data acquisition
DIC	Digital image correlation
FE	Finite element(s)
LAPACK	Linear Algebra Package
LLNL	Lawrence Livermore National Laboratory
N	Newton (unit of force)
NPS	Naval Postgraduate School
Pa	Pascal (unit of pressure)
RVE	Representative volume element
UMAT	User-defined material subroutine
VUMAT	Vectorized user-defined material subroutine
WWFE	World-Wide Failure Exercise

THIS PAGE INTENTIONALLY LEFT BLANK

Acknowledgments

I would like to first thank my advisor, Distinguished Professor Young Kwon, for providing guidance and mentorship during my studies at NPS. I am grateful for his support in completing my research.

I am also grateful for the members of my dissertation committee, Drs. Erick Alley, Anthony Gannon, Joshua Gordis, Jeremy Kozdon, and John Molitoris. Their time in and out of the classroom as mentors at NPS is greatly appreciated.

My studies at NPS were made possible by the Navy's Graduate Education Program with the endorsement and support of the Engineering Duty Officer community. I gratefully thank the Engineering Duty community for this opportunity: Seapower through Engineering.

In support of my research, I thank the Lawrence Livermore National Laboratory's Office of Defense Coordination headed by Assistant Director for Military Affairs George Sakaldasis, COL, USAF (ret) for promoting and funding the invaluable academic collaboration between NPS and Lawrence Livermore National Laboratory. Thanks also go to the Defense Threat Reduction Agency and Project Svarog for providing a basis for this research.

The organizers and participants of the World-Wide Failure Exercise contributed an enormous amount to the exploration of composites. They provided a perfect environment in which to develop and against which to compare my work.

I was fortunate to have a great office mate, Jarema Didoszak. I thank him for his help, feedback, lab assistance, photographic expertise, mentorship and friendship.

Thanks also to my family for their encouragement and support.

Most importantly I thank my wife, Christine, for her patience, persistence, encouragement and selfless support through this extraordinary opportunity.

ad maiorem Dei gloriam

THIS PAGE INTENTIONALLY LEFT BLANK

CHAPTER 1:
Failure Modeling of Composites

In recent years, the characterization and prediction of composite failure have been rich topics of discussion. Two prominent investigations have been initiated and completed in 2004 and 2013 called the World-Wide Failure Exercise I and II. They explore the effectiveness and utility of many different composite failure theories against many sets of experimental data. The World-Wide Failure Exercise was prompted mostly because many theories have been put forth to understand the ultimate strength of composites. Most of these theories begin from the better-understood homogeneous and isotropic metals and plastics and add correction factors to account for the observed differences. Few of the failure theories, however, approach composites from the direction that a composite is an assemblage of various parts, each of them with particular properties, ways of interacting, and ultimate failure conditions. This research attempts to reconcile the performance of a composite as the collection of constituent materials and their interactions for a range of composite materials.

1.1 Literature Review of Existing Failure Models

An excellent overview of composite failure theories can be found in Sun et al. [1], where different failure theories were evaluated. The categories used in the evaluation were limit criteria, interactive criteria, and separate mode criteria.

The maximum stress and maximum strain criteria belong to the limit criteria while Hill-Tsai and Tsai-Wu criteria [2] are the examples of interactive criteria. Alternatively, Hashin-Rotem [3] and Hashin [4] criteria are the separate mode criteria. While the theories listed here are popular choices for designers and finite element software manufacturers, there are many additional criteria proposed (see Sun et al. [1] for a more comprehensive listing). All of the theories relied exclusively on the in situ composite-level uniaxial failure values to predict failures in the quadrants, i.e., the combined stress states.

1.1.1 Non-Interactive or Limit Criteria

A simple separate mode model is a rectangle formed by the limits of longitudinal tension and compression and transverse tension and compression.

Examples of limit criteria are maximum stress or maximum strain criteria, which compare the global stress or strain to a limit value, usually obtained by experiments. The drawback for these criteria is that they are primarily (if not exclusively) used for the specific material and composite layup for which they were tested. A limit criteria for a zero-degree composite would not be applicable for a symmetric composite composed of ±45-degree layers ($[\pm 45]_s$) composite. Simple models like the rectangle described above fail to adequately represent any interaction between failure types or progression through many types.

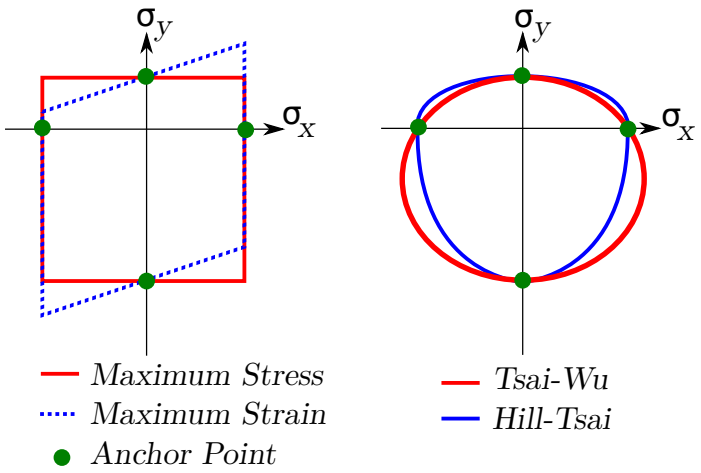

Figure 1.1. Examples of other theory failure envelopes

1.1.2 Interactive Models

Interactive models are failure models that include the influence of different aspects of a material failure model as a continuum. They are typically a single quadratic or higher order polynomial involving some or all of the components of composite stress or strain. They seek to combine a failure caused by one mode (e.g., longitudinal tension) with additional modes (transverse tension and/or others) into a combined mode. These models are useful in modeling the failure surface in the middle of the loading quadrants where limit criteria provide a poor representation of real failures.

One of the benefits of an interactive model is that it provides a continuous failure surface without facets, kinks or nodes, and provides smooth transitions between failure areas of influence. A drawback to these models is that they are seen as mostly curve-fitting combinations of known failure quantities to data representing failures resulting from combinations of those failure modes. This may require a non-trivial dataset with which to tune the model's fit.

Examples of interactive criteria are Tsai-Wu or Hill-Tsai, which are quadratic criteria that compare stresses to limit criteria and then combine these comparisons in a single formula, thus allowing interactions between the limiting values.

1.1.3 Separate Mode Macro-Scale Models

The separate mode models are those models that, unlike the interactive models, model failure as the locus of individual types (or modes) of failures. At their simplest, a separate mode model is a subset of a limit criterion. For instance, portions of Hashin's model [4] are longitudinal limit stress while other portions are interactive combinations of two limit criteria. More likely, however, a separate mode model mixes the simplicity of a limit criterion with mode-specific interaction. Individual failure modes can be interactive or a simple limit criteria.

1.1.4 Micro-Scale Modeling

Other methods to model failure in composites rely on the modeling of the individual materials in the composite and their interaction. Heretofore the models presented could be considered "macro scale" models, inasmuch as they seek to use macro-level failure stresses or strains as a basis to determine the failure of a composite structure—a top-down approach. Alternatively, the modeler may use a bottom-up approach and start at the level of the materials that constitute the composite, define their interactions and generate not only their undamaged properties from the homogenization of the constituent properties, but also determine failure levels based on the interactions of the constituents at less than macro scale due to loads applied at the macro level.

The actual application of micro-scale modeling varies from theory to theory. In some cases, the only use of the model is estimating macro-properties from micro-properties

and geometrical relationships. In others, the micro-model is used as a computational or conceptual basis for a macro-level formulation (frequently the basis for the macro-models above). Some of the varied uses are described below.

A frequently used concept is the representative volume element (RVE) of the composite, usually a repeated cell or a stochastic representation of fibers in a matrix material. The use of RVEs is very common since it allows flexibility to the modeler in the choice of shape of the RVE (cylindrical, triangular prism, cube, hexagonal prism, etc.), as well as the makeup of the RVE to include various materials, voids or other inclusions in a composite. This RVE or other representation is then modeled in finite element software and subjected to the loading conditions that are expected to cause failure. The major difference between the uses of RVEs is the method used to relate the micro scale of the RVE to the macro scale of the composite material. The states of stress and strain between the portions of the RVE observed in this simulation help to determine the states of stress and strain that define failure for the macro structure constructed from this RVE.

Chamis [5] also uses RVE to formulate a method to estimate composite substresses in intra-fiber, inter-matrix and inter-fiber regions of the RVE. Then Gotsis et al. [6] upscale the microstresses calculated to determine macro-level stresses which are used in a quadratic failure criteria. González and LLorca [7] use an RVE to model a portion of a notched beam (the notched portion of interest) with the constituent properties and cohesive contact in finite element software.

Alternatively, Robbins [8] explores a micro-scale model through a finely discretized RVE. He states that the computational cost of solving the stress-state of the RVE at each solution point is too high. To avoid this cost, the RVE is solved for general or "fundamental" stress cases, which provide a set of transfer functions for application to the micro-scale.

1.1.5 Progressive Damage

Many failure models are conjoined with an originator's effort to employ their failure criteria beyond initial indications of failure. In most cases, the failure models take some form of degraded properties of the constituents or plies that make up the composite. Once the degradation has been applied, the damage models then rely on classical laminate theory to re-establish a new set of aggregate properties. The damage can be applied in three forms: the

ply's macro-level properties are directly degraded, the ply is degraded by a predetermined amount based on failure type, or the constituent material or interface in an RVE is degraded and the RVE properties recalculated and upscaled to the macro-level ply values.

The simplest progressive damage model is that of the "parallel spring" model, which treats each lamina in a laminate as a spring with longitudinal and transverse elastic properties. Sun et al. [1] use the parallel spring model in their evaluation of failure models. Following a model's indication of failure, the failed "spring's" properties are decremented and recombined according to the modeling technique used for the structure. Another name for this method is termed the "ply discount method." Boghetti et al. [9] use a similar method in which they reduce properties related to the type of failure detected by the criterion in use (in their case, maximum strain).

1.1.6 The World-Wide Failure Exercise

The World-Wide Failure Exercise (WWFE) [10] was an academic exploration of current composite failure theories. The exercise was conducted in two phases, the first phase provided the participants with basic data regarding composites of interest and asked them to first describe their theories, then to use their theories to predict failure envelopes and/or stress-strain curves for various uniaxial composites and laminate layups. The WWFE included contributions from many failure theories, most from each theory's originators or their colleagues.

The WWFE provides an enormous resource in that it collates and evaluates alternative composite failure theories and provides a consolidated and extraordinarily varied set of experimental data against which to compare their performance. The experimental data provided was used extensively to devise the failure theory proposed by this research as well as to test its efficacy.

1.2 Objective

The multi-scale model method will be used to develop a failure model for fiber composites. With that failure model, a method for stiffness reduction following partial failure will be proposed such that the failure model can be applied to laminated composites. Once the failure model and the stiffness reduction method are developed, they will be transferred

into a subroutine that can be efficiently implemented into finite element codes. The finite element code with failure subroutine will then be used to generate failure envelopes for unidirectional lamina as well as laminated composites.

Using the multi-scale model as a representation of fibrous composites, the response of a composite structure can be examined as the sum of the responses of its constituents. Additionally, we are able to examine the failure of a composite structure as a function of the interactions of its constituents. This research is expected to propose a simple criterion definable with the use of existing tools. The criteria can then be applied to advance the definition and understanding of composite failure.

1.3 Expected Outcomes

This research begins with the explanation of the multi-scale model and its computational foundations. Also necessary to this discussion is understanding the shortcomings of the theory—where its representation of reality is questionable—most importantly so they can be mitigated and the range of applicability of the theory understood.

Following the definition of the Multi-scale Cellular model, the failure model for fibrous composites based on the elements of the multi-scale model is defined. Initial damage, defined in Chapter 3, is then expanded so that individual failure of a lamina can contribute to the progressive damage of a multilayer, multi-angle laminate.

In order to increase the utility of the failure model based on multi-scale modeling, the multi-scale model, the failure initiation criteria as well as the damage progression model is then implemented in a Fortran code suitable for use in most finite element solvers (3DS's Abaqus, in this case). The Fortran implementation is then tested against five sets of WWFE data as well as three different sets of experiments completed by the author.

Lastly, the multi-scale model is then explored through a parametric analysis of the inputs of the method: constituent modulus, fiber volume fraction, temperature variations, and small angle perturbations.

CHAPTER 2:
Multiscale Modeling of Fibrous Composites

Parts of this chapter were previously published in *Multiscale and Multidisciplinary Modeling, Experiments and Design* [11]. [1]

2.1 Multiscale Modeling

Multiscale modeling of a fibrous composite relates the material properties, stresses and strains at the lamina level (called macro-level) to those at the constituent material level (called micro-level). Both levels are connected bi-directionally. Figure 2.1 shows the schematic for coupling the macro-scale and micro-scale levels. The essential link for the coupling is through the unit-cell model.

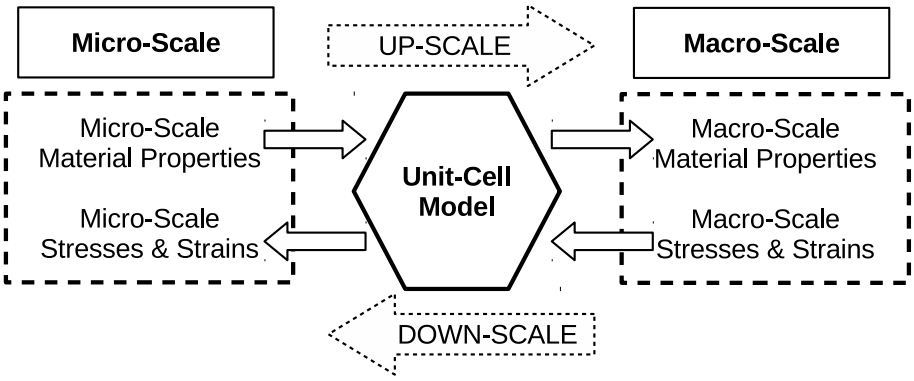

Figure 2.1. Schematic diagram of multiscale coupling

The unit-cell model for the representative composite strand has eight subcells. For a fibrous composite, only four subcells are strictly necessary. However, the model to be described was developed not only for the fibrous composite but also for particulate and whisker composites,

[1]Reprinted, with permission, from Y. Kwon and J.Darcy, "Failure criteria for fibrous composites based on multiscale modeling," *Multiscale and Multidisciplinary Modeling, Experiments and Design*, March 2018. This publication is a work of the U.S. Government as defined in Title 17, United States Code, Section 101. Copyright protection is not available for this work in the United States. Springer Nature will claim and protect its copyright in international jurisdictions where permission from Springer must be obtained for all other uses, in any current or future media, including reprinting/republishing this material for advertising or promotional purposes, creating new collective works, for resale or redistribution to servers or lists, or reuse of any copyrighted component of this work in other works.

and is unmodified in this research to retain its flexibility. As a result, the unit-cell model used here has eight subcells. Material properties are assigned to each subcell. A sketch of the unit cell is given in Figure 2.2. The assignment of properties and the relative sizes of the subcells are based on the constituents' material properties and the fiber volume fraction. For instance, a fibrous composite would be represented by fiber properties (moduli, volume fraction, coefficients of thermal expansion, Poisson's ratio, etc.) assigned to subcells 1 and 2, while the matrix properties are assigned to the remaining subcells. In addition, inclusions, voids and alternative materials as well as different cellular aspect ratios can also be modeled.

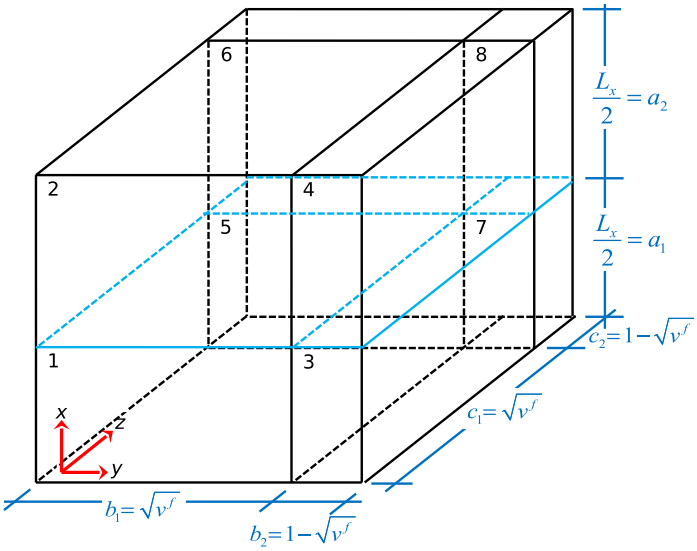

Figure 2.2. Unit cell model. Adapted from [12].

For this discussion, the following terms are defined:

- Strand: the entire unit cell containing connected fiber and matrix portions; the strand is the macro-level composite
- Subcell: the lowest division of the composite unit cell, one of eight rectangular prisms with assigned material properties; stresses and strains assigned to a subcell are denoted by, for example, σ_x^1 and ε_z^3 indicating x-directional normal stress in the 1st subcell and z-directional normal strain in the 3rd subcell, respectively
- Quarter-cell: the combination of two subcells in a particular direction; for instance, a fibrous composite assigns fiber properties to subcells 1 and 2, therefore the fiber lies in the 1-2 quarter-cell; stresses and strains are denoted similarly to subcells; a second

superscript indicates the included subcell such as σ_x^{12} indicating the fiber-directional stress in the 1-2 quarter-cell

- Half-cell: similar to the quarter-cell, describing a whole side of the unit cell; stresses in this case are denoted with the addition of superscripts: σ_z^{3478} which represents the z-directional stress in the 3-4-7-8 half-cell
- Upscale: to use constituent mechanical properties in order to predict composite macro properties
- Downscale: to decompose the macro level strains of a composite into stresses and strains in each of the subcells in the unit cell

In this discussion, the coordinates are always described as below:

- x - the longitudinal fiber direction
- y - the first transverse direction, starting in the 1-2 quarter-cell, with the direction toward the 3-4 quarter-cell; the y-direction is always used as the in-plane direction
- z - the second transverse direction, starting in the 1-2 quarter-cell, with the direction toward the 5-6 quarter-cell; the z-direction is always used as the out-of-plane or thickness direction

The strand description starts with the geometrical relationships of the unit cell and the subcells that comprise it. As shown in Figure 2.2, the total dimension on each side is taken as unity. The fiber is described as assuming the entire first and second subcells (the full x length of the subcell). Matrix material is assigned to the third through eighth subcell, also filling the entire x direction of the unit cell. In the y and z directions, the fiber-to-matrix ratio or volume fraction (v_f) control the dimensions of the subcells. For example, the unit cell length in the y direction is the sum of the fiber subcell y dimension and the 34 quarter-cell y dimension.

As proposed in Kwon and Berner [12], the subcells are joined together by requiring normal stress continuity between adjacent subcells as stated below:

$$\sigma_x^1 = \sigma_x^2, \sigma_x^3 = \sigma_x^4, \sigma_x^5 = \sigma_x^6, \sigma_x^7 = \sigma_x^8 \tag{2.1}$$

$$\sigma_y^{12} = \sigma_y^{34}, \sigma_y^{56} = \sigma_y^{78} \tag{2.2}$$

$$\sigma_z^{12} = \sigma_z^{56}, \sigma_z^{34} = \sigma_z^{78} \tag{2.3}$$

Shear-stress continuity between subcells adjacent in the shear stress direction is expressed:

$$\tau_{xy}^{12} = \tau_{xy}^{34}, \tau_{xy}^{56} = \tau_{xy}^{78} \tag{2.4}$$
$$\tau_{xz}^{12} = \tau_{xz}^{56}, \tau_{xz}^{23} = \tau_{xz}^{78} \tag{2.5}$$
$$\tau_{yz}^{15} = \tau_{yz}^{36}, \tau_{yz}^{27} = \tau_{yz}^{48} \tag{2.6}$$

Compatibility of normal and shear strains between each half-cell is expressed:

$$\varepsilon_x^{12} = \varepsilon_x^{34} = \varepsilon_x^{56} = \varepsilon_x^{78} \tag{2.7}$$
$$b_1\varepsilon_y^{12} + b_2\varepsilon_y^{34} = b_1\varepsilon_y^{56} + b_2\varepsilon_y^{78} \tag{2.8}$$
$$c_1\varepsilon_z^{12} + c_2\varepsilon_z^{56} = c_1\varepsilon_z^{34} + c_2\varepsilon_z^{78} \tag{2.9}$$

$$\gamma_{xy}^{1234} = \gamma_{xy}^{5678} \tag{2.10}$$
$$\gamma_{xz}^{1256} = \gamma_{xz}^{3478} \tag{2.11}$$
$$\gamma_{yz}^{1357} = \gamma_{yz}^{2468} \tag{2.12}$$

where

$$\gamma_{xy}^{1234} = \gamma_{xy}^{12}(a_1 + a_2)b_1 + \gamma_{xy}^{34}(a_1 + a_2)b_2 \tag{2.13}$$
$$\gamma_{xy}^{5678} = \gamma_{xy}^{56}(a_1 + a_2)b_1 + \gamma_{xy}^{78}(a_1 + a_2)b_2 \tag{2.14}$$
$$\gamma_{xz}^{1256} = \gamma_{xz}^{12}(a_1 + a_2)c_1 + \gamma_{xz}^{56}(a_1 + a_2)c_2 \tag{2.15}$$
$$\gamma_{xz}^{3478} = \gamma_{xz}^{34}(a_1 + a_2)c_1 + \gamma_{xz}^{78}(a_1 + a_2)c_2 \tag{2.16}$$
$$\gamma_{yz}^{1357} = \gamma_{yz}^{15}(c_1 + c_2)b_1 + \gamma_{yz}^{37}(c_1 + c_2)b_2 \tag{2.17}$$
$$\gamma_{yz}^{2468} = \gamma_{yz}^{26}(c_1 + c_2)b_1 + \gamma_{yz}^{48}(c_1 + c_2)b_2 \tag{2.18}$$

The last required connection is the consideration that the total strain is the volume-averaged sum of the subcell strains. The relationships above are described as

$$\bar{\varepsilon}_{ij} = \sum_{n=1}^{8} V^n \varepsilon_{ij}^n \tag{2.19}$$

where $\bar{\varepsilon}_{ij}$ is the ij-th strain component of the composite, V^n is the volume of the n-th subcell, and ε_{ij} is the ij-th strain component of the n-th subcell. The same expression can be also written for the stress components like

$$\bar{\sigma}_{ij} = \sum_{n=1}^{8} V^n \sigma_{ij}^n \tag{2.20}$$

This system of equations allows for the volume-averaged combination of the properties of the constituents yielding a global or macro-scale set of properties of the composite. Once the macro-scale properties are established, a macro-scale compliance matrix can be simply employed to calculate the macro-scale strains to applied stresses. The finite element method can be also utilized to analyze a complex shape of composite structure subjected to the applied loading in order to compute the macro-scale stresses and strains. The unit-cell model determines the stresses and strain at every subcell from these macro-scale strains. Thermal effects can also be included in this model, as by Kwon and Kim [13]. Thermal effects on the failure envelope are discussed in Chapter 8, Parametric Studies.

2.1.1 Strengths of the Theory

The theory discussed in Kwon and Park [14] is extremely useful and simple in its execution and implementation. Also, as shown in Kwon and Park [14], its performance for the prediction of macro properties of a composite, knowing only the properties of the constituents, is very satisfactory. The upscale and downscale routines are simple routines that can be implemented in any numerical software package in 500 or so lines (much fewer with efficient coding). The relationships between the subcells are simple and intuitive.

An additional strength of the theory is that the degraded properties of a lamina can be calculated *before* the analysis. The global-to-subcell (downscale) transformation relationships and composite-level constitutive relationships for each type of failure (and all combinations of failures) can be formed from the constituent properties in the first iteration and stored as reference values, allowing the subroutine to avoid matrix inversions and decompositions unrelated to solving the finite element problem, potentially significantly speeding up the subroutine performance.

2.1.2 Drawbacks of the Theory

The theory, while simple in its formulation and implementation, does have some drawbacks. The routines rely on some data that may not be readily available, specifically, transverse moduli and Poisson's ratio of fibers and shear modulus of fibers. These values may not be readily available from manufacturers or experimentalists. However, reasonable guesses for unknown properties can be made without significant impact to the output of the method. Also, as will be shown, the method itself can be used to estimate unknown properties from global values and known properties.

The formulation does not include shear coupling, that is: normal stresses on the composite only result in normal strains. Furthermore, the theory allows for strain discontinuities in the y and z directions between quarter-cells as well as shear-strain discontinuity between half-cells. These discontinuities are illustrated in Figure 2.3.

The shear strain discontinuity illustrated on the left of Figure 2.3 demonstrates the result of shear in the $x-y$ plane. The total shearing strain for both half-cells equals the macro-level shearing strain; however, adjacent quarter-cells (1-2 and 5-6, 3-4 and 7-8) are allowed to have incompatible shear strains. This is of important consequence, since the calculation regarding maximum principal strain relies on the shear strain value. The adjustment for this discontinuity is discussed in Section 3.1.4 and as will be shown, provides a convenient ability to tune a failure envelope such that it provides a failure range from conservative to aggressive.

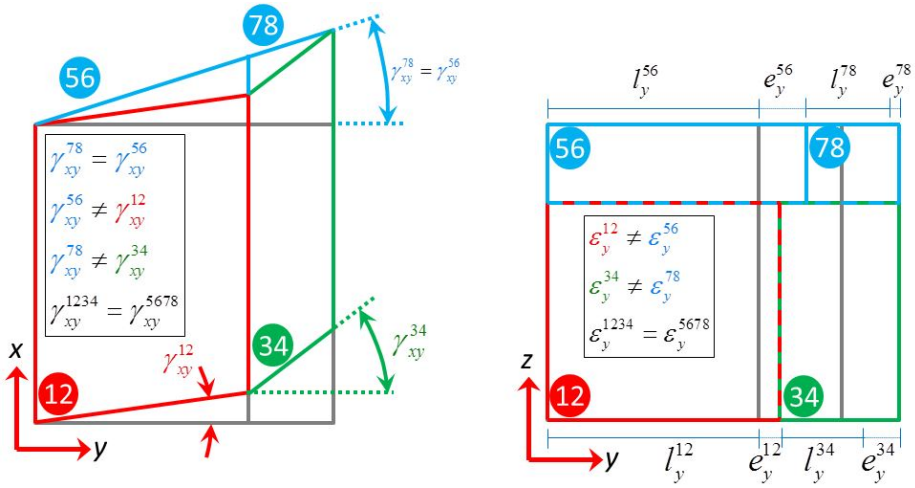

Figure 2.3. Allowed discontinuities

Of primary importance (and utility) is the shear strain discontinuity. It is best demonstrated when a shear stress is applied in the $x-y$ plane. The total shearing strain for both half-cells equals the macro-level shearing strain; however, adjacent half-cells are allowed to contain quarter-cells with discontinuous shear strain. This allowed discontinuity is likely only an artifact of the model, and will negatively impact any failure calculations based on these strains. The adjustment for this discontinuity is discussed in Section 3.1.4, and as will be shown, provides a convenient ability to tune a failure envelope such that its predictions are either conservative or aggressive.

2.2 The Constituent Properties

To determine the material properties of the composites, the material properties of the constituents must be known. The multiscale model, comprised of continuous fibers and matrix material, requires the input of the material properties of first the fiber, the composite and some details of the composite itself. Most of the material properties that are of concern can be found in literature provided from a material's manufacturer. In some cases, the relevant material properties are difficult to locate, are not provided, or are difficult or impractical to measure. In such cases, estimates for these properties adapted from similar materials can be used or the properties can be estimated using known properties of the constituents and composite. These estimates can be accomplished with the multiscale model's upscale and downscale routines discussed in Section 2.3.

2.2.1 The Fiber

The fiber, in most cases, is the main strength member for the composite. It usually consumes the majority of the volume of the composite and accounts for at least 90% of the modulus of the composite. The multiscale model requires the input of the following properties in order to complete both the upscaling (homogenizing) and downscaling calculations:

1. E_x^f – Longitudinal Young's Modulus
2. E_y^f – Transverse Young's Modulus
3. ν_{xy}^f, ν_{yz}^f – Longitudinal and Transverse Poisson's Ratio
4. G_{xy}^f – Shear Modulus
5. v^f – fiber volume fraction

6. α_x^f – Coefficient of thermal expansion for fiber in longitudinal direction
7. α_y^f – CTE of fiber in transverse direction

As discussed, some of these inputs are not easily obtained. Transverse Young's modulus (E_y^f), Poisson's ratios (ν_{xy}^f, ν_{yz}^f), shear modulus (G_{xy}^f) and coefficients of thermal expansion (α_x^f, α_y^f) are infrequently reported by manufacturers or are difficult to establish. However, reasonable estimates for these inputs can be used for preliminary modeling. The WWFE provided this data for its participants; however, for the designer and researcher, this same WWFE data can be a starting point for comparable materials. The composite and constituent data provided by the WWFE was used in this research.

2.2.2 The Matrix

The matrix material provides the composite that which the fiber material cannot: transverse and shear stiffness as well as support in compression loading. The multiscale model requires fewer properties of the matrix material since the matrix is considered homogeneous and isotropic. The properties required are:

1. E^m – Young's modulus of matrix (assumed isotropic)
2. ν^m – Poission's ratio (assumed isotropic)
3. α^m – CTE for matrix

The matrix material properties are usually more available than those of the fiber material. Most of the needed properties are available from resin manufacturers or can be obtained experimentally. Again, for the majority of test cases in this research, the WWFE data provided in Hinton et al. [10] was comprehensive and included all required values.

2.3 Estimating Properties

Many methods have been proposed to estimate macro composite properties from the properties of the constituents. Moncada et al. [15] and Robbins [8] use finite element models of representational volume elements to homogenize the constituents to predict macro properties. Kwon and Park [14] use the multiscale method to predict macro properties.

The prediction methods rely on the documented properties of composites, found from manufacturers like Hexcel [16] [17], academia [10], and reference texts like the Society of

Automotive Engineer's Composite Materials Handbook [18]. In addition to the data found in these sources, the estimation methods may also rely on data that is difficult to obtain. The usually unknown properties are:

1. E_y^f – The transverse elastic modulus of the fibrous portion of the composite
2. ν_{yz}^f – The transverse Poisson's ratio of the fibrous portion of the composite
3. G_{xy}^f – The shear modulus of the fibrous portion of the composite

These properties, and some of the better-known properties that are not available, can sometimes be assumed to be the same as their orthogonal counterparts by assuming that the material is isotropic. For carbon fiber, however, this is a poor representation as demonstrated in Miyagawa et al. [19], where the experimentally measured transverse elastic modulus was 6% of the longitudinal modulus. Therefore, for carbon fibers it may be best suited to take the transverse elastic modulus of carbon fibers as 10% of their longitudinal values.

To estimate other unknown properties, the multiscale method can be combined with an optimizer that uses known properties of both the constituents and the composite to tune initial guesses provided by the user. Preliminary work was done forming a nonlinear optimizer that uses the known composite properties as targets and all function inputs as parameters. The optimizer uses the objective function:

$$
\begin{aligned}
\underset{x_i}{\text{minimize}} \quad & \sum_{i=1}^{8} |1 - x_i| \\
\text{subject to} \quad & 0.25 \leq x_i \leq 2,\ i = 1, \ldots, 8 \\
& [\text{outputs}] = \texttt{upscale\_function}(\text{inputs}) \\
& E_x^s = E_x^{given} \\
& E_y^s = E_y^{given} \\
& \nu_{xy}^s = \nu_{xy}^{given} \\
& \text{*Other constraints}
\end{aligned}
$$

The optimizer changes the multiples (x_i) of one or many of the upscaling function inputs (the constituent materials' properties) and penalizes departures from unity on these multiples.

An additional use of this optimizer is tuning the values of selected constituent properties such that the upscaled material properties exactly reproduce those measured experimentally. Using an optimizer in this way also allows for a cross-property adjusting while preventing major departures from the stated constituent values. This simple routine can be implemented in programs like Excel, MATLAB or more advanced solvers. Further adjustments can be made to this routine to refine its method. Also, additional weights can be added to the objective such that changes to certain input parameters are "penalized" more than other changes.

2.4 Upscale Routine Sensitivity to Input Variables

Some additional work was done to determine the sensitivity of the forward function outputs to the material property inputs. The results are summarized in Table 2.1. Table 2.1 represents the change of the output variable (the major columns) due to a -10% change (the left minor column) and a +10% change (the right minor column) in the input variables (the rows). Both positive and negative changes are shown so that it can be determined whether the sensitivity is in general linear or not, and the general response direction of the output variable.

Table 2.1. Function output sensitivity

	E_1		E_2		E_3		G_1		G_2		G_3		ν_{12}		ν_{23}	
efl	-9.88	9.88	-0.05	0.04	-0.05	0.04	—	—	—	—	—	—	—	—	-0.18	0.15
eft	—	—	-5.42	4.99	-5.42	4.99	—	—	-2.86	2.47	—	—	0.10	-0.08	0.78	-0.76
nuf12	—	—	0.03	-0.03	0.03	-0.03	—	—	—	—	—	—	-5.33	5.33	0.11	-0.11
nuf23	—	—	0.26	-0.25	0.26	-0.25	—	—	0.55	-0.54	—	—	0.03	-0.03	-3.16	3.14
em	-0.12	0.12	-4.98	4.56	-4.98	4.56	-9.46	9.35	-7.55	7.16	-9.46	9.35	-0.09	0.09	-0.68	0.55
num	—	—	-3.73	4.89	-3.73	4.89	2.58	-2.45	2.00	-1.93	2.58	-2.45	-4.91	5.21	-11.75	13.91
vf	-9.69	9.69	-7.23	7.66	-7.23	7.66	-15.68	20.74	-7.49	8.81	-15.68	20.74	2.07	-2.05	5.56	-5.44
gf12	—	—	—	—	—	—	-0.66	0.55	—	—	-0.66	0.55	—	—	—	—

As seen in Table 2.1, the volume fraction, when changed by itself, has the largest effect on all output variables. While this variable has the most cross-output effect, it is usually one of the best known inputs into the model, reducing its variability. As expected, the fiber properties dominated the fiber-direction modulus, and the perpendicular modulus was relatively evenly split between the fiber transverse modulus and the matrix modulus. This table gives a general map as to what properties to adjust to dial in the mathematical model's property estimates to experimentally observed properties.

Additionally, in the general range of ±10%, most of the output responses were generally linear (or can be approximated as linear); however, for larger changes, some of the responses were nonlinear, emphasizing the need to have relatively good estimates of the unknown properties of the constituents before using the simple optimizer above.

2.5 Specific Routine Operation

In order to implement the multiscale model in both upscale and downscale directions, the relationship matrix, T, is formed as a 24x24 matrix. This relationship matrix uses Equations 2.1 through 2.3, 2.7 through 2.9 and Equation 2.19. These equations represent that the total strain of the strand is the sum of the strains contained in the strand, and that the strain is also volume-averaged strain.

The relationship matrix T is composed of three sub-matrices $[[T_1][T_2][T_3]]^T$. The first portion, T_1, forms the relationships between global stress and subcell stress. The first four rows of T_1 expresses Equations 2.1. Similarly, the remaining eight rows reflect normal stresses in the y and z (Equations 2.2 and 2.3). To demonstrate, the fifth row relates the strains between the 12 quarter-cell and the 34 quarter-cell in the y direction. The linear system is thus:

$$\begin{bmatrix} c^f_{yx} & -c^m_{yx} & \dots & c^f_{yy} & -c^m_{yy} & \dots & c^f_{yz} & -c^m_{yz} & \dots \end{bmatrix} \begin{bmatrix} \varepsilon^{12}_x & \varepsilon^{34}_x & \dots & \varepsilon^{12}_y & \varepsilon^{34}_y & \dots & \varepsilon^{12}_z & \varepsilon^{34}_z & \dots \end{bmatrix}^T = 0 \quad (2.21)$$

where the entries like c^f_{nm} are the (n, m) entry in the fiber component subcell stiffness matrix, and likewise for the matrix material subcell stiffness matrix.

Submatrix T_2 establishes the normal strain relationships—that the directional strain of the strand is equal between each half-cell, and that the strain in each half-cell is the weighted sum of the strains of each quarter-cell (Equations 2.7 through 2.9). Submatrix T_3 parses Equation 2.19, establishing that the global directional strain is the sum of the volume-weighted subcell strains.

Once T is formed, it is partially inverted to obtain the 24x3 R matrix which allows the volume-averaged and stress-equating distribution of global normal strains (ε^s) to subcell

normal strains (ε^c) by multiplying $R\varepsilon^s = \varepsilon^c$. Only the last three columns of R are for non-zero equations, so R is obtained by solving the linear system $TR = \{e_{22}\, e_{23}\, e_{24}\}$, where e_n are the 22nd through 24th unit vectors.

To establish the upscaling, a combined stiffness matrix (24x24) is formed and multiplied by the downscaling matrix R to obtain the 24x3 distributed stiffness matrix. The directional stiffnesses are then linearly combined and weighted by the relative volumes of the subcells. This yields a 3x3 normal stiffness matrix for the material. To obtain the upscaled values for directional moduli and Poisson ratio, this matrix can be inverted and the values extracted, where the diagonals are the inverse of the upscaled composite directional stiffnesses, and the off diagonals are these values with the composite Poisson ratios in the numerator.

To calculate the upscaled shear moduli, Equations 2.13 through 2.18 are used. The shear modulus of each half-cell is estimated by combining its quarter-cell's shear moduli, weighted by the quarter-cell cross-sectional area (length and width) in the plane of interest (Equations 2.22 and 2.23). These values are then combined across the half-cells by applying the half-cell dimension in depth as the weighting factor. For instance, the shear modulus of the unit cell in the $x - y$ plane is calculated:

$$G_{xy}^{1234} = \frac{1}{ab_1/G_{xy}^f + ab_2/G_{xy}^m} \tag{2.22}$$

$$G_{xy}^{5678} = \frac{1}{ab_1/G_{xy}^m + ab_2/G_{xy}^m} \tag{2.23}$$

$$G_{xy}^s = c_1 G_{xy}^{1234} + c_2 G_{xy}^{5678} \tag{2.24}$$

where a, b_n, c_n are the dimensions from Figure 2.2 and $a = a_1 + a_2$.

2.6 Conclusion

The micro-mechanical model for fiber composites proposed in Kwon and Berner [12] was described, as well as some of its benefits and shortcomings. Additionally, the inputs to the method—namely the properties of the constituents—were described. For properties that are either unknown or less-well defined like the transverse modulus of a fiber phase, estimating methods and optimization routines were proposed. The sensitivity of the outputs

of the upscaling routine was also explored in order to target the most effective alterations to input properties to better represent macro-level properties. Lastly, the mechanics of the calculation of the upscaling method were explained. With the upscaling and associated downscaling methods defined, the material properties and response under load, both macro and micro, can be predicted.

THIS PAGE INTENTIONALLY LEFT BLANK

CHAPTER 3:
Failure Model Based on Multiscale Model

Parts of this chapter were previously published in *Multiscale and Multidisciplinary Modeling, Experiments and Design* [11]. [2]

Composite materials have been applied to many load-carrying structures and gradually replaced metals in structures and devices. This ubiquity makes accurate predictions of failure strengths of composites essential. The multi-phase, inhomogeneous and anisotropic nature of composite materials lies at the heart of the complexity of accurate failure prediction.

The proposed failure criteria uses stresses and strains exhibited in the constituent materials such as fiber and matrix materials as described in the following sections. The criteria were developed to describe physics-based modes of failure at the micro-scale level. The failure modes are fiber breakage, fiber buckling, matrix cracking, and fiber/matrix interface debonding. The proposed criteria are evaluated against available experimental data as given in the World-Wide Failure Exercise data given to participants [10].

3.1 Failure Criteria

As discussed previously, many of the existing failure theories are based on the use of the test data of a lamina. This theory currently requires the use of constituent materials' strength data. If some of those data are not available, they can be derived from the lamina level test data. The failure envelope of a composite is defined as the locus of points of each failure mode. The following failure criteria are similar to the Hashin separate mode criteria [4] which is also discussed in Sun et al. [1], but is distinct from Hashin in its use of the micro-mechanics model as its basis and its use of strain rather than stresses.

3.1.1 Fiber Failure in Tension

This criterion is applicable for fiber under tensile loading. This failure mode is called fiber breakage. Once the fiber subcell's resultant strain reaches the failure strain of the fiber, the

[2] Please see permissions statement in Note 1 in Chapter 2.

fiber is considered failed based on the following criterion:

$$\frac{\sqrt{\left(\varepsilon_x^{12}\right)^2 + \left(\gamma_{xy}^{12}\right)^2 + \left(\gamma_{xz}^{12}\right)^2}}{\varepsilon_{u,t}^f} \geq 1 \tag{3.1}$$

This failure criterion takes shear angle into account so that the elongation of the fiber is not only the longitudinal lengthening of the fiber subcell, but also the imposed shear angle, as sketched in Figure 3.1. The shearing angle may not initially appear important, but it becomes significant for larger shearing stress on top of the longitudinal stress.

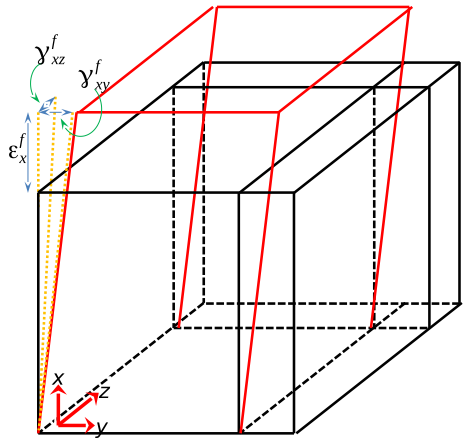

Figure 3.1. Fiber elongation

The data required to implement this criterion is the fiber elongation at failure, $\varepsilon_{u,t}^f$, which is commonly available information. While using this value in the failure model yields results within 4% of the stated composite value, the micro-mechanics model can also be used to adjust this quantity so as to exactly match the macro-level anchor point. To do this, the macro failure stress is applied to the unit strand and the fiber failure strain is calculated using the downscaling routine. This can be useful since the fiber elongation at failure may provide an over-prediction of the stated longitudinal strength of the composite.

This formulation of the fiber breakage criteria is unique since other criteria that separate the modes of composite failure are primarily stress-based. Due to the ability to extract both the normal and shear strain of the fiber phase of the composite through the multiscale method, the failure strain of the constituent can be used directly rather than rely on the macro-level failure values.

3.1.2 Fiber Failure in Compression

The second criterion is for fiber failure while under compression. It is called fiber buckling, and the criterion is defined as

$$\frac{\sqrt{\left(\varepsilon_x^{12}\right)^2 + \left(\gamma_{xy}^{12}\right)^2 + \left(\gamma_{xz}^{12}\right)^2}}{\varepsilon_{u,c}^f} \geq 1 \tag{3.2}$$

where $\varepsilon_{u,c}^f$ is the fiber (and composite) longitudinal strain at the stated ultimate compressive stress as calculated by $\varepsilon_{u,c}^f = \frac{\sigma_u^C}{E_x^C}$, in which the superscript C indicates composite (macro-scale) values. Since this value is derived from the macro failure stress through the micro-scale model, it requires no adjustment like the fiber breakage criterion.

3.1.3 Fiber/Matrix Interface Failure

One of the most important portions of this failure criteria is the debonding of the fiber/matrix interface between the fiber and matrix phases. The simplest form of this criterion describes the failure of the interface when the transverse normal stress between the fiber subcell and its adjacent matrix subcell reach a critical value. As stated, this criterion would simply be a maximum shear stress criteria applied at the subcell level:

$$\frac{|\tau_{xy}^{34}|}{\tau_u} \geq 1 \tag{3.3}$$

where τ_u is the in-plane failure shear of the composite. This, as will be shown later, is an incomplete picture, since longitudinal tensile stresses appear to delay shear failure and transverse tensile stresses appear to promote shear failure. This requires that there be some additional terms in the shear failure portion to account for the promotion or delay of the onset of shear failure in a composite sample. Empirical data will be used to determine which outputs of the multiscale method are best suited as terms in the failure criteria.

To understand the response of the subcells reported by the multiscale method as load progressed through the normal-shear space, a hemielliptical path through each of the normal-shear planes was chosen. These paths are meant to provide controlled, prior-to-failure input of loads to the multiscale downscale routine in order to plot the output. The paths chosen are illustrated alongside representative failure data in Figure 3.2 (a) and (b). The paths were

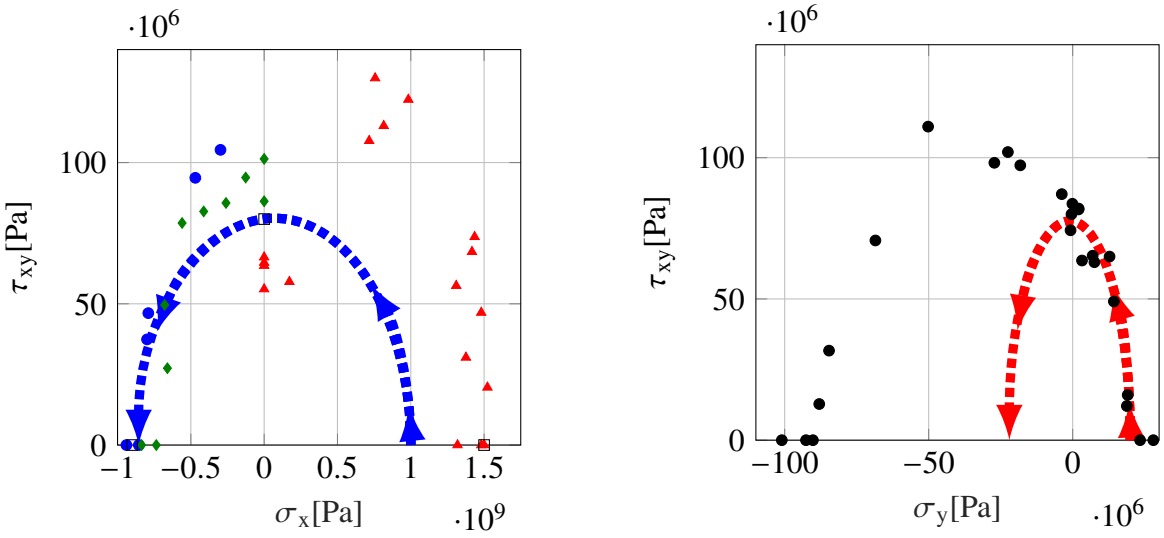

(a) Path through $\sigma_x - \tau_{xy}$ space

(b) Path through $\sigma_y - \tau_{xy}$ space

Figure 3.2. Paths through stress space

defined by the stated failure points of the composite ($\sigma_{x,T}$, $\sigma_{x,C}$, $\sigma_{y,T}$, $\sigma_{y,C}$, and $\tau_{xy,U}$) as the semimajor and semiminor radii. For this illustration, the properties of a T300-BSL914C were used, although Figure 3.2 (a) shows failure data from E-Glass LY556. The paths were defined by:

$$\left(\frac{\sigma_x}{1 \times 10^9}\right)^2 + \left(\frac{\tau_{xy}}{8 \times 10^7}\right)^2 = 1$$

for the $\sigma_x - \tau_{xy}$ subspace and

$$\left(\frac{\sigma_y}{4 \times 10^9}\right)^2 + \left(\frac{\tau_{xy}}{8 \times 10^7}\right)^2 = 1$$

for the $\sigma_y - \tau_{xy}$ subspace.

Figure 3.3 plots the stress values calculated in the micro-model as the micro-model is swept through these paths. The plot contains the shear stress between the 12 and 34 quarter-cells from the applied stress as well as both the x and y stresses in the 34 quarter-cell, τ_{xy}^{34}, σ_x^{34}, and σ_y^{34}.

In the $\sigma_x - \tau_{xy}$ subspace, Figure 3.3 (a), the calculated σ_x and σ_y subcell stresses in the 34 quarter-cell are two and four orders of magnitude, respectively, less than the applied

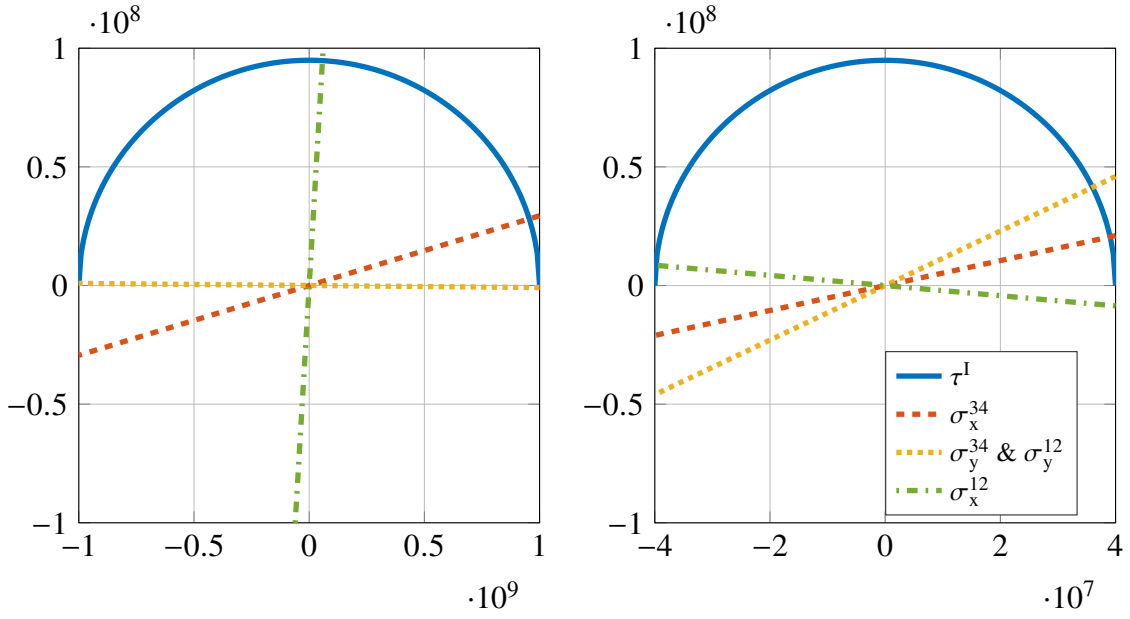

(a) σ_x vs. τ_{xy} (b) σ_y vs. τ_{xy}

Figure 3.3. Plot of subcell stress along hemiellipses in shear-normal space

longitudinal load. This is reasonable, since the fiber is the major load-carrying component. Alternatively, in the $\sigma_y - \tau_{xy}$ subspace, the calculated σ_x and σ_y subcell stresses are both the same order of magnitude and same sign as the applied transverse normal stress.

For the $\sigma_x - \tau_{xy}$ plane, Figure 3.2 (a), empirical data implies that ultimate failure is delayed with tensile σ_x and promoted with compressive σ_x, the calculated σ_x^{34} can be used to diminish τ_{xy}^{34}. The impact that σ_x^{34} has on the criteria can be controlled using a scaling factor α_1. The first alteration to Equation 3.3 becomes:

$$\frac{\tau_{xy}^{34} - \alpha_1 \sigma_x^{34}}{\tau_u} \geq 1 \tag{3.4}$$

For the $\sigma_y - \tau_{xy}$ plane, Figure 3.3 (b) and Figure 3.2 (b), observation implies that ultimate failure is *promoted* with tensile σ_y and *delayed* with compressive σ_y, the calculated σ_y^{34} can then be used to *increase* τ_{xy}^{34}. Likewise, its impact can likewise be scaled with α_2. The corresponding alteration to Equation 3.3 becomes:

$$\frac{\tau_{xy}^{34} + \alpha_2 \sigma_y^{34}}{\tau_u} \geq 1 \tag{3.5}$$

For a complete shear picture and to enable the use of a single criterion for all of shear space, we combine Equations 3.4 and 3.5, and allow for simplicity $\alpha_1 = \alpha_2$:

$$\frac{\tau_{xy}^{34} + \alpha_1(\sigma_y^{34} - \sigma_x^{34})}{\tau_u} \geq 1 \tag{3.6}$$

This form is satisfactory for the interface when it is under shear stress; however, it does not include interface debonding under pure transverse tension. It is logical to assume that debonding under transverse load will occur only under tensile transverse loading rather than compressive loading, which will likely reinforce any interaction between the fiber and matrix subcells until some other failure occurs, like matrix cracking due to the same compressive load. To include this impact, the transverse stress term is added:

$$n\frac{\sigma_y^{34}}{\sigma_\perp} \geq 1 \qquad n = \begin{cases} 1 & : \sigma_y^{34} > 0 \\ 0 & : \sigma_y^{34} \leq 0 \end{cases} \tag{3.7}$$

where $\sigma_\perp$ is the stated transverse failure strength of the composite.

It can be observed that bonded subcells under either longitudinal or transverse normal stresses experience some interface stresses due to the mismatch in stiffness of the two materials. The criterion includes the impact of the normal stresses on the interface shearing stress. For the complete criteria, we combine Equations 3.6 and 3.7 and allow them to interact as a quadratic polynomial. The criterion is stated as:

$$\left(\frac{\tau^I + \alpha_1(\sigma_y^{34} - \sigma_x^{34})}{\tau_u}\right)^2 + n\left(\frac{\sigma_y^{34}}{\sigma_\perp}\right)^2 \geq 1 \tag{3.8}$$

and similarly for the 12-56 interface:

$$\left(\frac{\tau^I + \alpha_1(\sigma_z^{56} - \sigma_x^{56})}{\tau_u}\right)^2 + n\left(\frac{\sigma_z^{56}}{\sigma_\perp}\right)^2 \geq 1 \tag{3.9}$$

where τ^I is the interface shear stress, calculated for the 34 subcell as:

$$\tau^I = \frac{\gamma_{xy}^{12} G_{xy}^f + \gamma_{xy}^{34} G_{xy}^m}{2} \tag{3.10}$$

or calculated for the 56 subcell as:

$$\tau^I = \frac{\gamma_{xz}^{12} G_{xz}^f + \gamma_{xz}^{56} G_{xz}^m}{2} \tag{3.11}$$

and α_1 is the scaling factor—currently $\sqrt{v^f}$—v^f is the fiber volume fraction, τ_u is the critical interface shear stress, and $\sigma_\perp$ is the critical interface normal stress. The impact of the shear-to-normal scaling factor, α_1, is explored in Chapter 6 along with the criteria's performance against experimental data.

The interface shear stress, τ^I is expressed as in Equation 3.10 and 3.11 as the average of the shear stresses in adjacent subcells. Using the portion of the downscaling routine described in Equation 2.24, these values should be the same; however, this averaging ensures that small variations between the two calculated shear strains are minimized. Values for τ_u can be calculated using the downscaling routine by applying the macro-level shear stress at failure to the unit strand and obtaining the interface stress between the fiber and matrix subcells. Values for $\sigma_\perp$ are adequately estimated using the uniaxial transverse failure strength.

The additional parameter, 'n', is equal to 1 when the composite is under transverse tension and zero when the composite is under transverse compression. The reason for this is to indicate that interface failure between the fiber subcell and the matrix subcell (specifically separation due to transverse normal stress) will only happen when the specimen is under transverse tension. Compressing this interface can only reinforce the connection between the subcells until the matrix reaches a crush value (i.e., failure by maximum principal strain as described below).

This formulation is very similar to Equation (16) in Sun et al. [1], which takes the matrix quadratic failure criterion (a matrix-specific application of the Hill-Tsai):

$$\left(\frac{\sigma_x^m}{X_m}\right)^2 + \left(\frac{\sigma_y^m}{Y_m}\right)^2 - \frac{\sigma_x^m}{X_m}\frac{\sigma_y^m}{X_m} + \left(\frac{\tau_{xy}^m}{S_m}\right)^2 \geq 1$$

where X, Y, and S are the matrix failure strengths. Sun then neglects the longitudinal term, and simplifies the above to:

$$\left(\frac{\sigma_y}{Y}\right)^2 + \left(\frac{\tau xy}{S}\right)^2 \geq 1$$

Sun et al. [1] then observe similar strengthening in composite failure values while under transverse compression and shear discussed previously. Their accounting for this behavior becomes:

$$\left(\frac{\sigma_y}{Y}\right)^2 + \left(\frac{\tau xy}{S - \mu\sigma_y}\right)^2 \geq 1 \qquad \mu = \begin{cases} \mu_0 & \sigma_y < 0 \\ 0 & \sigma_y \geq 0 \end{cases} \tag{3.12}$$

However the criteria proposed in Equations 3.8 and 3.9 include the presumed shear interaction between the matrix subcell and the fiber subcell due to normal loading in either or both the transverse and longitudinal directions. This criterion allows for the theory to account for the lack of shear-coupling as well as the observed delay in shearing failure while under longitudinal stress and the promotion of failure while under transverse tension.

The primary reason that the normal stress terms are in the above formulation is due to the observation in the WWFE data [5] that normal stresses either promote or delay specimen failure depending on orientation and sign. The primary thought about this interaction is that two bonded dissimilar materials undergoing the same strain will experience different stresses. For instance, the subcells undergoing longitudinal stress without bonding would all respond as independent springs and reach their own strain state that satisfies the stress state. In the case of the fiber subcell, its independent elongation would be less than the composite's elongation due to the applied stress. Conversely, the matrix subcells' independent elongation would be much greater than the composite's elongation. The two materials, however, impact one another. The fiber subcell is further elongated by the presence of the matrix subcells and the matrix subcells' elongations are moderated by the presence of the fiber. This mismatch is the likely reason for normal stresses causing interface shearing.

3.1.4 Matrix Failure

Matrix failure is also called matrix cracking. The failure criterion employed the maximum strain criterion, since it relies only on the calculation of the maximum principal strain experienced in each of the matrix subcells. The only complication of this criterion is the requirement to moderate the shear strain value between the fiber-matrix half-cell and the matrix-matrix half-cell. As discussed earlier, the shear strain compatibility only applies in each half-cell. The shear strain that must be used, therefore, is some combination of the calculated shear strain for the matrix portion of the fiber-matrix half-cell (worst case) or the

calculated shear strain for the matrix-matrix half-cell. The compromise is the mean of the two, making the criterion:

$$\frac{\varepsilon_1^m}{\varepsilon_{u,t}^m} \geq 1 \quad \text{OR} \quad \frac{\varepsilon_3^m}{\varepsilon_{u,c}^m} \geq 1 \tag{3.13}$$

where ε_1^m and ε_3^m are the principal strains of the state of strain determined from the following matrix:

$$\boldsymbol{\varepsilon}^{34} = \begin{bmatrix} \varepsilon_x^{34} & \gamma_{xy}^{34}+\gamma_{xy}^{78}/4 & 0 \\ \gamma_{xy}^{34}+\gamma_{xy}^{78}/4 & \varepsilon_y^{34} & 0 \\ 0 & 0 & \varepsilon_z^{34} \end{bmatrix} \tag{3.14}$$

The strain tensor for the matrix subcells is formed with the off-diagonals as shown in order to overcome the discontinuity allowed in Section 2.1.2. It averages the shear strains calculated for the 34 and 78 quarter-cells. The impact of this averaging is discussed in Chapter 6 along with the criteria's performance against existing data. The tensor for failure in the 56 subcell is similar in concept; however, it needs to overcome the same shortcomings in the xz plane.

$$\boldsymbol{\varepsilon}^{56} = \begin{bmatrix} \varepsilon_x^{56} & 0 & \gamma_{xz}^{56}+\gamma_{xz}^{78}/4 \\ 0 & \varepsilon_y^{56} & 0 \\ \gamma_{xz}^{56}+\gamma_{xz}^{78}/4 & 0 & \varepsilon_z^{56} \end{bmatrix} \tag{3.15}$$

Notice that only 34 and 56 matrix failure are the only ones considered since matrix failures in 34 or 56 quarter-cells are assumed to propagate to the 78 quarter-cell. Additionally, the 78 quarter-cell is small in comparison to the other matrix cells, so failures in the 78 quarter-cell and their associated reductions in strength are small in comparison to the reductions due to a pure 34 or 56 failure. In practical terms, this failure is exhibited primarily in the transverse compression regime.

Again, this formulation is unique in that it uses the maximum principal strains of the matrix subcells rather than the global (normal) strain of the composite to determine matrix failure, enabled again by the disaggregation techniques in the multiscale method.

3.2 Tuning Routine

In addition to estimating unknown variables, as discussed in Section 2.3, the failure model parameters may also need to be adjusted such that the composite meets a stated or tested

strength. In order to provide these data for better modeling, the multiscale method can be used to update the critical failure values. For instance, in longitudinal failure the virgin fiber's elongation at failure is used initially as the determination for longitudinal failure. Using this value may overpredict longitudinal failure stress by 5-10%. The longitudinal composite failure stress or strain as measured in experiments can be used through the multiscale method to update the failure strain of the fiber to that reported by the multiscale method with the failure stress or strain applied. To simplify this updating, a Fortran routine was written that takes as inputs the constituent parameters of the composite and the so-called failure anchor points and outputs the upscaled composite properties (homogenized moduli, etc.) as well as updated estimates for failure values such that the failure model represents the required composite anchor points.

3.3 Conclusion

In this section, calculations made possible by the multiscale method and observation of empirical data were joined to propose novel criteria for fiber composite failure. The criteria proposed is a separate mode stress- and strain- based criteria. The fiber failure criteria as well as the matrix failure portions are unique to this method, while the interface failure portion is based on the quadratic Hill-Tsai with additions made possible by the multiscale calculations.

The next sections describe a progressive failure and material degradation model that would take place after the proposed criteria indicated a failure. Finally, the multiscale formulation, the failure criteria, and progressive damage model are combined into a single subroutine to be included in finite element solutions. The performance of this model for both uniaxial lamina and multi-angle laminates as well as and explorations of its inputs are also included.

CHAPTER 4:
Damage Initiation and Progressive Damage

With a criterion that indicates under which conditions a particular ply will fail, a method must be developed to reduce the stiffness of the failed ply in the failure direction and allow this reduced stiffness to propagate through the remainder of the structure. In order to describe this method, damage modes will be discussed as well as the logic behind particular reductions to the unit strand. The defined failure criteria is used as an indication of when material degradation in a single unidirectional ply should begin. The methodology behind the proposed strength reduction technique and its general implementation in the context of the multiscale model is then described. Finally, the damage initiation and strength reduction are applied to the strength of a laminate and the laminate's ultimate failure.

The damage modes are divided between longitudinal and transverse damage modes. Damage types characterized by these modes will be defined and the reductions that are taken as a result of those damages will be introduced. The method of tracking damage and storing and communicating this information in a solution process will be discussed. A few methods explored in this research that help determine "ultimate failure" of a composite sample under test will be introduced.

Described here is essentially a mode-specific progressive-softening ply-discount method, where specific failures in specific plies are reduced in stiffness following failure. Nearly any discount method can be applied using this research's failure theory such as ply-discount, parallel spring, and first-ply failure.

4.1 Damage Initiation

The four failure types defined by the criteria in Chapter 3 are the fiber elongation, interface failure, fiber buckling, and matrix failure by maximum principal strain. To determine when a composite lamina transitions from an intact to a damaged state, Equations 3.1, 3.2, 3.8, 3.9 and 3.13 are used as initiation quotients. When any of these quotients reach unity, the subject lamina or portion of lamina is considered failed. Post failure behavior and ultimate failure follow damage initiation indicated by the criteria in Chapter 3.

4.2 Damage Progression

Progressive failure is defined as the path of feasible failures that follow an initial failure. Feasible failures are failures that can logically take place after an initial failure. For instance, beginning with an interface failure, a matrix failure due in whole or part to transverse loading is not feasible as the matrix material is conceptually separate from transverse support; however, fiber failure following an interface failure is a feasible failure. The damage initiation quotients give a starting point for where in the loading life of a structure the properties should begin to degrade. The way in which the properties should degrade and by what quantities will be based on the conceptual model of the unit cell.

4.3 Longitudinal Damage

The first damage mode is that characterized by failures that would result in significant reduction in the longitudinal strength of the composite or ply in either tension or compression. Longitudinal damage is characterized by either or both of fiber failure by elongation or matrix failure by maximum principal strain in either tension or compression.

4.3.1 Longitudinal Tensile Damage

Longitudinal tensile failures reduce the longitudinal modulus of the constituent material. When fiber failure is indicated, the modulus of the fiber subcell is reduced in the present model by 99%, though this is a tunable parameter. This is likely the most consequential longitudinal failure, since the fiber subcell's modulus contributes over 90% of the modulus of the composite strand.

Matrix material failure and interface failure caused by longitudinal tension are also permitted. Matrix cracking in the longitudinal direction is handled similarly to a fiber break, reducing the contribution of the matrix material to the longitudinal stiffness of the unit strand. Longitudinal tension, when combined with transverse tension or compression or in-plane shear also may cause interface debonding, however interface failure caused by longitudinal tension would cause a smaller reduction in longitudinal modulus due only to the reduced Poisson effect that this interface provided before failure. The damage caused by the interface debonding is discussed in Section 4.4.

As a feasible failure, matrix longitudinal failure by cracking following interface failure must be only due to longitudinal and out-of-plane (thickness direction) strains. This is due to the presumption that a failed interface cannot sustain in-plane transverse strain, and therefore cannot transmit that strain to the matrix material subcells. In this instance, Equation 3.14 would be altered as:

$$\varepsilon_d^{34} = \begin{bmatrix} \varepsilon_x^{34} & 0 & \gamma_{xz}^{34}+\gamma_{xz}^{78}/4 \\ 0 & 0 & 0 \\ \gamma_{xz}^{34}+\gamma_{xz}^{78}/4 & 0 & \varepsilon_z^{34} \end{bmatrix}$$

Similar reductions would be done for interface debonding in the 56 quarter-cell.

The reduction in strength of failed fiber and/or matrix subcells is accomplished by altering the transformation matrix T, described in Section 2.5. Since the first submatrix T_1 controls the x or longitudinal properties of the composite strand, those entries are the elements that are reduced. In conjunction with the reduction in longitudinal stiffness due to a longitudinal failure, shear stiffness is also reduced in the upscaling and downscaling routines by reducing the appropriate quantities in Equations 2.22 and 2.23 and their orthogonal counterparts.

4.3.2 Longitudinal Compressive Damage

Compressive damage, mainly characterized as fiber buckling or matrix crush causes a similar reduction in subcell stiffness, and is reduced in the same manner as tensile damage. An additional consideration is a reduction in longitudinal stiffness of the fiber subcell following interface failure. This reduction considers any loss of stiffness of the fiber subcell due to the removal of that subcell's reinforcement.This reduction is again taken during the upscale/downscale matrix formation by reducing the stiffness contributions of the fiber.

4.4 Transverse Damage

Figure 4.1 begins with interface failure since it alone of the four failure types is considered, in the context of a laminate, a possible intermediate or non-catastrophic failure mode. If fiber failure by either elongation—tensile fracture or buckling—or matrix failure by compression is indicated absent of interface failure, these usually are associated with complete failure. However, the present model allows for the appropriate reduction in stiffness of the failed ply and the detection of additional failures.

The stiffness of the strand is initially reduced by the interface failure, which causes the y-direction stiffness (E_y^s) and the shear stiffness (G_{xy}^s) to approach zero, while the longitudinal and z-transverse (E_y^s, E_z^s) stiffnesses remain unchanged. The shear stiffness of the fiber (1-2) subcell (G_{xy}^f) is also reduced, since half of the supporting matrix is no longer attached.

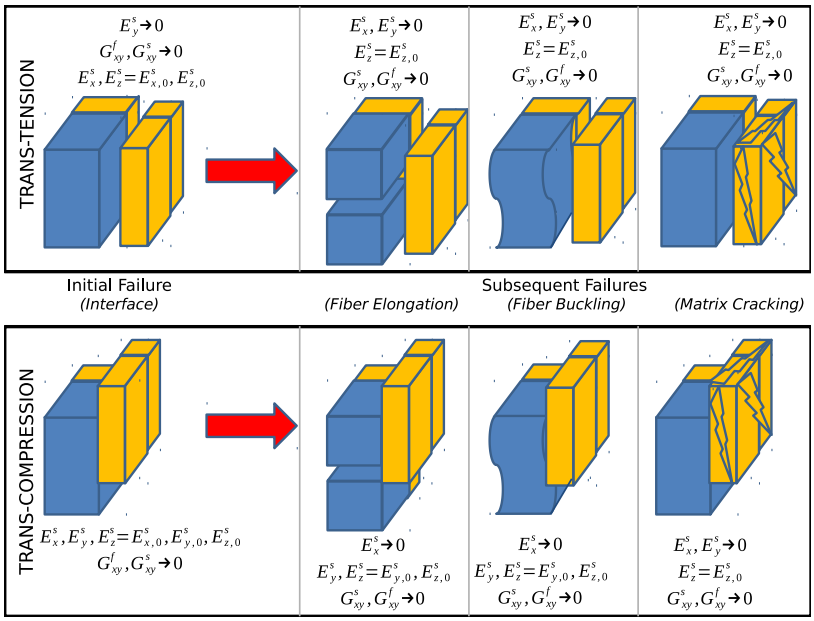

Figure 4.1. Progressive failure flow and stiffness reduction methodology beginning with interface failure

No additional transverse failures can occur since the stiffness in the transverse direction is very low. This, however, does not preclude longitudinal failures of the fiber or the separated matrix subcells. Following this initial failure, three types of failure are now possible: fiber elongation, fiber buckling and matrix cracking. These failures cause additional reductions in the remaining stiffnesses of the strand, indicating ultimate failure of the represented ply.

Matrix failure following interface failure becomes more complex. The matrix can now be considered a separated homogeneous and (assumed) isotropic material under a $[\sigma_x, 0, \sigma_z, 0, \tau_{xz}, 0]^T$ state of stress. The σ_y, τ_{xy} and τ_{yz} components are all assumed to be zero since there is conceivably separation between the 3478 half-cell and the 1256 half-cell, not allowing the 3478 half-cell to sustain stress in the y direction. In this case, the matrix stiffnesses can be used to determine additional matrix failures by maximum principal strain, as discussed earlier. Also, a portion of the shear stress (strain) from the laminate (surrounding lamina) can be placed on the z faces of the 3478 half-cell.

4.4.1 Transverse Tensile Damage

Transverse damage is described as either 34 quarter-cell interface failure or 34 quarter-cell matrix failure as defined in Chapter 3. This type of failure should result in a similar reduction in stiffness for both modes, since a matrix crack or a fiber-matrix debonding mode would likely be indistinguishable or occur at the same time. To reduce the stiffness of the unit cell due to this failure, the construction of the relationship matrix t and the distributed stiffness matrix is altered. The elastic modulus of the affected subcells (34 and 78) are reduced to 1% of their initial value in the direction of failure. To apply this to the unit cell, the submatrix $[T_2]$ entries related to the transverse stiffness of the 34 and 78 subcells are multiplied by the reduction factor (1%) and the upscaled stiffness matrix and the downscaling matrix R are reformed with the reduced transverse stiffnesses.

The 78 quarter-cell's properties are also reduced in this instance, since a 34 quarter-cell interface failure or matrix failure is assumed to affect the 78 quarter-cell equally. This simulates a crack that has propagated through the entire xz plane of the unit cell since it may not be reasonable to assume that a crack would initiate between the fiber 12 quarter-cell and matrix 34 quarter-cell and not propagate through the unit cell. A similar reduction is programmed for interface failure between the 56 quarter-cell and the 12 quarter-cell, and it similarly effects the 78 quarter-cell stiffness in the z direction.

In addition to transverse stiffness reduction, a transverse failure is also assumed to reduce the shear stiffness of the unit cell as the bond between the 1256 half-cell and 3478 half-cell is modeled as no longer contributing to the transverse stiffness of the unit cell. For instance, a 3478 transverse failure would provide little shearing resistance to shearing in the $x - y$ and $y - z$ planes. As such, the shear moduli for those cells must be reduced. To accomplish this, while forming the unit-cell shear moduli, the shear stiffnesses of the affected subcells is reduced in the failure directions by the reduction factor (again, 1% of its initial value), and recombine the subcell moduli to generate the upscaled unit cell modulus.

In the case of transverse failure, the fiber subcell in this model has lost its support in the failure plane, since the fiber-matrix bond is modeled to be either non-existent or significantly diminished. Fibers, in the absence of a matrix material, are assumed to not be able to sustain shear loading (despite one of the entries in the subroutine being the shear modulus of the fiber). For these reasons, the shear modulus in the model is also reduced. In addition to

reducing the shear stiffness of the fiber subcells following a transverse interface failure, the transverse stiffness of the fiber subcell is also reduced. This prevents artificial or nonexistent strength of the unit cell provided by a failed bond and its corresponding Poisson ratio.

The current model reduces the shear modulus by 99%, however this estimate can be improved with experiments like a three-rail shear test or combined experiments that would load a sample such that interface failure would be indicated and then the sample would then be tested in a three-rail shear test.

Two different failure criteria can track similarly presenting failures. Interface debonding and matrix tensile failure may be the same failure or at least, they may be indistinguishable. For instance, transverse interface failure can be indicated by the transverse criteria quotient, and reductions taken due to that failure. In this case, transverse matrix failure in the 3478 half-cell would be ignored since it is no longer the major mode of failure. In future iterations of this method, the matrix failure criteria would change following an interface failure such that it checks only the principal strains in the feasible loading directions. An interface failure would preclude further loading in the transverse directions, therefore any further failures in a matrix subcell would need to be due to loading in the remaining loading directions.

4.4.2 Transverse Compression

The bottom of Figure 4.1 shows a similar progression, however the strand is under transverse compression and either longitudinal tension or compression. The major difference between these two scenarios is that despite interface failure, transverse stiffness (E_y^s) is not reduced since the matrix is intact and remains in contact with the other two subcells. The major reduction in stiffness would be the in-plane shear stiffness, since the shear stiffness, provided by the bond between the 3478 half-cell and 1256 half-cell no longer exists. There would likely be frictional contact sustaining some shear stress, but it is ignored. Furthermore, similar to the interface failure under transverse tension, the shear strength of the fiber subcell is reduced following the removal of the support from the failed interface. Subsequent failures in this case can be fiber failure (elongation or buckling), matrix failure by maximum principal strain, though the stress state in this case is $[\sigma_x, \sigma_y, \sigma_z, 0, \tau_{xz}, 0]^T$.

Under compression, an interface failure would likely only cause a reduction in the shear stiffness of the lamina as well as a reduction in the fiber buckling strain, since one of the

supporting matrix subcells has debonded. Similar to the above scenario, the additional failures following interface failure allow for further reductions in the strand's stiffness.

4.5 Tracking Damage and Strength Reduction

Unlike uniaxial composite, in a laminate, initial failure is likely not ultimate failure. The load borne by the structure will most likely cascade to the remaining intact (or partially intact) load bearing members. In a homogenized laminate, the stiffness contribution of the failed lamina would be appropriately reduced as required by the indicated failure, and the stiffness matrix for the laminate would be re-homogenized. In a finite element software, the stiffness contribution of a failed section point would be similarly reduced and then re-homogenized in accordance with the modeling technique.

In order to reduce the post-failure stiffness of the unit-strand, the upscale and downscale routines require information regarding which cell and the failure direction of that cell. For three matrix quarter-cells and three directions, this requires nine pieces of information for each analysis point. These nine entries can be included in a 3-by-3 matrix. The columns of the matrix describe the failure directions: x, y and z; while the rows of the matrix describe the subcells that have failed. An entry of zero in any position indicates an undamaged state. An entry of one in a position indicates a fully failed state. This matrix is referred to as `failang`.

Entries in `failang` are attributed to failed states and combinations of failed states. For instance, a 1 in the (1,1) position of `failang` describes a failure in the 34-subcell in the x direction, and a 1 in the (2,2) position describes a failure in the 56-subcell in the y direction. The matrix `failang` is a convenient way to control the reduction of the properties of the constituents in the transformation matrix in order to obtain a degraded material constitutive matrix.

To simplify the storage of `failang`, the failure modes it describes can be broken into the three individual directions for failure. Transverse failures in the y direction—3478 interface

failures and 3478 matrix failures—can be represented in `failang` as:

$$\texttt{failang}_y = \begin{bmatrix} 0 & 1 & 0 \\ 0 & 0 & 0 \\ 0 & 1 & 0 \end{bmatrix}$$

and similarly for failures in the x and z directions. Using this method, all normal failures and their combinations can be described by the sum of these three matrices. Above, reductions in shear stiffness were associated with normal failures; using these associations, all reductions to stiffness—both shear and normal—following a failure can be described by a normal failure only. This also reduces the information required to be stored regarding failure status of a material point to three variables. The three variables scale predetermined matrices, which sums to `failang`:

$$\texttt{failang} = \zeta_1 \begin{bmatrix} 0 & 1 & 0 \\ 0 & 0 & 0 \\ 0 & 1 & 0 \end{bmatrix} + \zeta_2 \begin{bmatrix} 0 & 0 & 0 \\ 0 & 0 & 1 \\ 0 & 0 & 1 \end{bmatrix} + \zeta_3 \begin{bmatrix} 1 & 0 & 0 \\ 1 & 0 & 0 \\ 1 & 0 & 0 \end{bmatrix} \tag{4.1}$$

where ζ_n represents the amount of reduction in strength due to each failure type, varying between zero and one. For example, a 3478 half-cell interface failure with a 1% reduction in y strength combined with a 50% reduction due to a 5678 half-cell interface failure would yield:

$$\texttt{failang} = 0.01 \begin{bmatrix} 0 & 1 & 0 \\ 0 & 0 & 0 \\ 0 & 1 & 0 \end{bmatrix} + 0.5 \begin{bmatrix} 0 & 0 & 0 \\ 0 & 0 & 1 \\ 0 & 0 & 1 \end{bmatrix} + 0.0 \begin{bmatrix} 1 & 0 & 0 \\ 1 & 0 & 0 \\ 1 & 0 & 0 \end{bmatrix} = \begin{bmatrix} 0 & 0.01 & 0 \\ 0 & 0 & 0.5 \\ 0 & 0.01 & 0.5 \end{bmatrix}$$

This scheme would then only require the storage of the ζ_n and a ζ_f, indicating a reduction in strength due to a fiber failure. While either zero or one are currently used in `failang`, these fractional values can be input to indicate fractional reductions of the properties at an interface or within a subcell. These fractional reductions can be used in a damage description where the composite under examination progressively softens over the analysis steps.

4.6 Finite Element Software Damage Evolution

In some finite element software, provision for the evolution of damage or progressive softening of a material is allowed such that the energy dissipated in the failure of a material agrees with experiment. This damage evolution is also employed to improve stability of an implicit calculation involving progressive damage such that softening can be accomplished over a few increments rather than all at once.

The finite element software Abaqus describes its method for accomplishing this in the Abaqus user manual Section 24.3.1 [20]. In general, the stiffness of a material is modeled as linear-elastic until a damage initiation criterion is satisfied. Following damage initiation, the material is progressively softened based on the energy dissipated during the damage process. The progress of damage is controlled by a damage variable that varies from zero to one, reducing portions of the stiffness matrix based on the type of failure indicated by the initiation criterion. This approach can be implemented using `failang` by considering the appropriate ζ_n as the damage variable which increases following an indicated failure from zero to one (intact to fully failed) through the fractional values required by the energy release rate.

4.7 Ultimate Failure

For uniaxial samples, ultimate failure can be simple to predict, since a single failure likely indicates ultimate failure. The complete strength of the sample is typically lost due to that failure. In a lamina however, the load previously carried by a ply that has failed in a particular way is redistributed to the adjacent plies that are capable of carrying the transferred load. The stress-state in a laminate becomes complex due to the various material orientations and their associated orthotropy. What would normally be a simple biaxial state in an isotropic (or uniaxial orthotropic) material becomes a complex $\sigma_x - \sigma_y - \tau_{xy}$ state of stress. This is further complicated with the unloading of a failed ply and the redistribution of its load to the adjacent plies.

Ultimate failure in uniaxial composites, described in Section 3.1, was indicated when a single failure of a lamina represented ultimate failure. Simple criterion like “excessive strain” or “an inability to increase the applied load” are objectively true, however a more finite means of measuring failure is needed to determine failure since first ply failure would

likely yield needlessly conservative estimates for failure. When determining ultimate failure while applying the present model to the WWFE tasks, an approach was used that quantifies the planar components of strain. This approach uses a change of "strain radius" where the strain radius allows the capture of the change of any single (or all three) strain quantities due to the failure of a ply. In the following form, it treats a change in any strain equally:

$$r_\varepsilon = \sqrt{(\varepsilon_x^c)^2 + (\varepsilon_y^c)^2 + (\gamma_{xy}^c)^2} \tag{4.2}$$

This form can be modified to change the weight of the contributing factors.

The strain radius can be used in three ways. As a measure of resultant strain, a maximum strain at a point of interest can be chosen and analysis can be stopped, indicating composite failure. Alternatively, the first derivative of the strain radius with respect to the load can provide a "cost" of the next load increment in terms of strain—analogous to "marginal cost," and termed marginal strain. Lastly, the second derivative of the strain radius with respect to load allows the determination of both the area of maximum curvature of the strain radius curve as well as the inflection point of the marginal strain curve by peak-finding. An illustration of these three curves is shown in Figure 4.2.

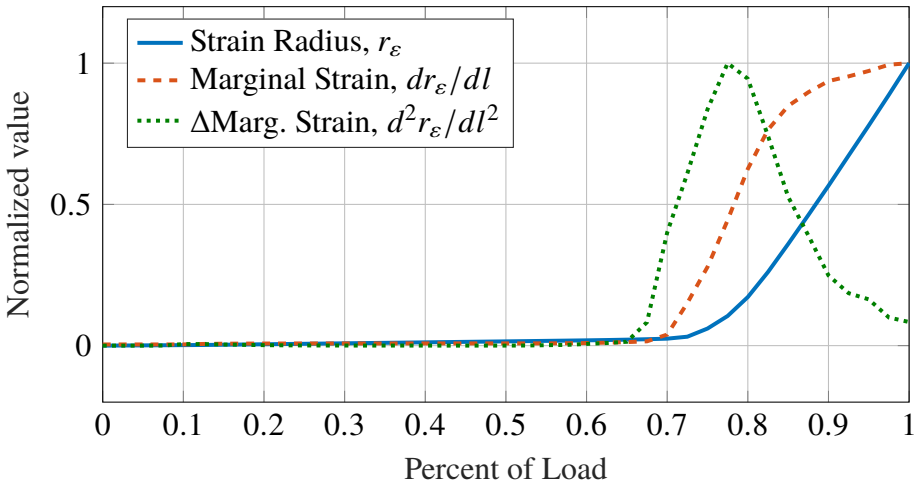

Figure 4.2. Ultimate failure detection by maximum curvature of strain radius curve

As loading of a composite progresses prior to major failures, the strain increases at a slow rate, commensurate with the small reductions in the stiffness of the loaded and (partially) failed ply. As damage continues, the strain radius (or resultant strain) increases more rapidly

until it begins to grow without bound. Figure 4.2 shows this response of the strain radius as well as the corresponding responses of marginal strain and change of marginal strain.

4.8 Determining Final Laminate Failure in Abaqus

The most convincing indication of failure in a simulation would be either the growth without bound of the displacement of all (or a portion) of the composite sample under test—analogous to a sample rupture, or the decrease to near zero of the load applied to the composite—analogous to extreme softening of the sample. In order to load the sample, either a pressure load on the surface of the sample laminate, or a displacement of the outer surfaces of the composite can be prescribed. In the case of the displacement, a loading condition must be prescribed on the outer surfaces and monitor the displacement of a telltale portion of the composite. In the case of load-carrying capacity, a nodal displacement is imposed on the sample and the reaction forces are monitored.

A Python script was used to generate failure envelope for the laminated composite from the finite element solver. Similar to the MATLAB envelope, a radar search was devised that changed the loading of the composite under test to follow chosen loading ratios. Each loading ratio was divided into 40 equal steps in order to accurately locate the features of failure as a percentage of the loading ratio. Likewise, each quadrant was divided into 50 sectors each corresponding to a loading ratio.

Once the solution is complete for a particular loading ratio, the Python routine extracts the history variables for the position of the center node, calculates their norms and differentiates twice. This data for each of the "slices" of each quadrant is written to a text file where it could be imported and parsed by a simple routine.

The method pursued to determine if failure has occurred in the Abaqus simulation was the plotting of the strain of the middle elements in both x, y and shear. These strains were then used to compute a single magnitude to measure the middle elements. The second derivative of the strain radius (Equation 4.2) with respect to the applied load was taken to locate the area of greatest curvature of the strain radius curve. These locations can correspond to initial and final failures of the composite under test.

Using this scheme in the first quadrant for the laminate, it can be seen that in some cases there are small perturbations in the second derivative, indicating that the rate of displacement is changing, followed by larger values for the second derivative, showing large curvature in the displacement curve. Small perturbations in the second derivative are assumed to mean that there are intermediate (but not completely fatal) failures in the composite. At these loading points, the composite's rate of displacement increases owing to the reduction in stiffness of a failed ply. The larger perturbations are indicative of rapid change in the growth of the displacement, which are assumed to mean that they are the location of ultimate failure.

4.9 Conclusion

With the multiscale model described in Chapter 2, the failure model it enables which is described in Chapter 3, and the progressive damage model described here, all the portions that are required for inclusion in either simple estimating methods like a MATLAB routine or more complex implementations in finite element software are present. These concepts are to be combined in a single Fortran routine such that they can be used in finite element software to provide composite properties, failure indications, and degraded material properties in the case of failure. The next chapter describes this routine and its operation, followed by its use and performance against experimental data.

CHAPTER 5:
Composing Theory into FE Codes

Initial development and testing of the proposed failure theory was conducted in the MATLAB software. Transitioning the failure theory and multiscale method from MATLAB to finite element software would increase their applicability and utility from simple models to more complex composite structures. This section describes the mechanics required to interface the multiscale failure theory with finite element solvers.

5.1 User Materials Interface

Many finite element solvers allow a more flexible interface for a user to input their own constitutive model for materials they desire to model. Finite element solvers from Abaqus, ANSYS, CalculiX, NASTRAN, among others, can use a subroutine written in Fortran to calculate or provide the constitutive relationships based on input data. This utility can be exploited using the power of a Fortran program to implement the calculations needed for the upscaling (to define the macro- or meso- properties for the composite) and downscaling (for determining the intra- and inter-cellular stresses and strains). A Fortran program also allows access to other libraries that simplify programming and accelerate the solution process.

5.1.1 Finite Element Code User Materials

The "user defined material" is an additional way for a user of a finite element package to provide material information to the software about the structure or material under examination. Under normal use, a finite element package can take as input the material properties of a structure as engineering constants, or tabular data. Most software has very flexible ways to input this data and allow for many different methods to change and manipulate this data as the solution progresses, however if a material model does not conform to these entry requirements, a user defined material script or "UMAT" must be constructed.

The user materials interface is different from most uses of finite element software implementation since it takes state information from the solver: time, temperature, strain, location, etceteras, and uses this information in any way the user requires to provide the constitutive

relationships of that material point and an updated state of stress and strain based on any in-step changes to the material properties. This flexibility is a perfect platform for the implementation of the multiscale model.

5.1.2 Fortran User Material

At its simplest, the Fortran program takes in position, time, temperature, stress information from the solver and either using these data or not, returns the constitutive relationship and an updated state of stress. The Fortran structure allows an enormous level of flexibility by allowing the inclusion of any number of methods to determine altered material properties and responses. In particular, linear algebra libraries such as Basic Linear Algebra Subroutines (BLAS) and Linear Algebra Package (LAPACK) can be simply implemented. [3]

5.1.3 The FE Code supplied data

Finite element codes that allow user material subroutines will frequently have similar inputs into those routines. The finite element suite used in this research (Abaqus) supplies 37 variables to any UMAT subroutine. These variables are arrays containing vector-valued data, stresses and strains from the previous increment, user-input material properties, time, temperature, etcetera. The most applicable variables are the user-input material properties, the incremental strain, and the solution state variables.

The UMAT uses these inputs as described above to perform the upscale, downscale, damage detection and strength reduction calculations at each material point.

5.1.4 Section Points and Layers

The finite element solver describes the material used in a model in relation to the elements used. If the material is described as a composite layup, the finite element solver breaks

[3] In order to include the BLAS and LAPACK functions in the FORTRAN code, the compiler flags that indicate the appropriate libraries must also be included. For use with Abaqus in Windows using the Intel Fortran compiler, the compiler flag "`/Qmkl`" must be included in the call to `ifort`. ("MKL" stands for Math Kernel Library, which is Intel's library that contains BLAS, LAPACK, and other vector math functions.) This is done in the user's `abaqus_v6.env` (or version appropriate) environment file in the list of flags beginning with "`compile_fortran`". If the Fortran compiler is something else, like `gfortran` under Linux, then the user would indicate the use of LAPACK or BLAS with the flags "`-llapack`" and/or "`-blas`" in the appropriate environment file.

the thickness or stacking direction into layers, with the material properties (modulus, orientation, etc.) assigned to each layer. Each layer can then be assigned an odd number of section points (user assignable) that describe points in each of the layers' thickness. The section points must be odd since they identify the top, middle and bottom of the layer. In the plane of the element, the section points are in alignment with the integration points of the element. The user material subroutine is called at each section point of each element in each increment of the solver's solution process. Figure 5.1 shows the relationships between section points and integration points.

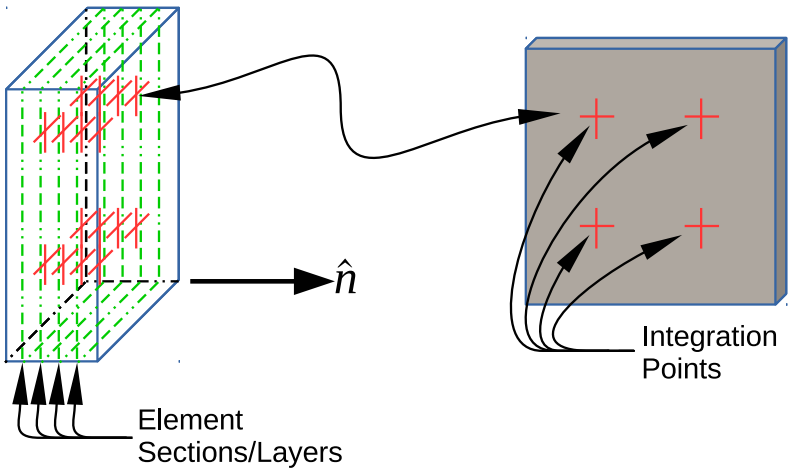

Figure 5.1. Section points in Abaqus

5.2 The UMAT

The micromechanics model for normal stresses is simply a system of linear equations, so efficient linear algebra routines such as those contained in BLAS and LAPACK can be used to solve the linear systems required to enable the downscaling in the UMAT. The Fortran code was written to accomplish four things:

1. To upscale the constituent material properties into macro-level constitutive relationships of the composite at the material point of interest and report those relationships to the finite element solver
2. To use the upscaled relationships and the strains reported by the FE solver at the material point to calculate stresses at the material point and report those stresses to the finite element solver

3. To downscale the strains reported by the FE solver to subcell strains and stresses and store those as function outputs (Solution-dependent state variables "`STATEV`")
4. To calculate the failure quotients based on the criteria in Chapter 3, calculate reductions based on failure state, and store these quotients, failure state and reduction parameters in the `STATEV` array

The UMAT currently outputs 58 User Defined variables into the `STATEV` array which contain the subcell strains (entries 1-24), subcell stresses (entries 25-48), and the failure model's failure state and failure initiation values (entries 49-55). The last three values are fractional values that control the reduction in strength of the subcells based on experienced failures. These are multiples that multiply portions `failang` as described in Section 4.5. The current UMAT formulation stores all these variables for all material points at every increment. This storage can become unwieldy and will likely need to be reduced such that the stored variables are only those that are required; however, to retain future flexibility the UMAT was written to include all available outputs. The logical flow of the UMAT is illustrated in Figure 5.2.

5.2.1 Downscale

The downscale subroutine operation was initially described in Section 2.5, and was adapted such that the operations required were accomplished using Fortran and appropriate linear algebra libraries.

The relationship matrix T is formed from the undamaged or damaged constituent material properties and is partially inverted forming the downscaling matrix R using the LAPACK linear algebra library solver DGESV (double precision, general matrix, linear solver). The linear solver obtains R by solving the linear system $TR = \{e_{22}\ e_{23}\ e_{24}\}$ by LU decomposition, where e_n are te 22nd through 24th unit vectors.

As a sub-function in the UMAT, the Downscale subroutine takes the R matrix returned by DGESV and uses it to decompose the normal strains input into the UMAT by the solver to normal strains in each subcell though matrix-vector multiplication: $R\varepsilon^{global} = \varepsilon^{subcell}$.

The shear strains are calculated using the shear strains input by the solver, the shear modulus of the unit-strand constituents, and the section-point failure status from the current

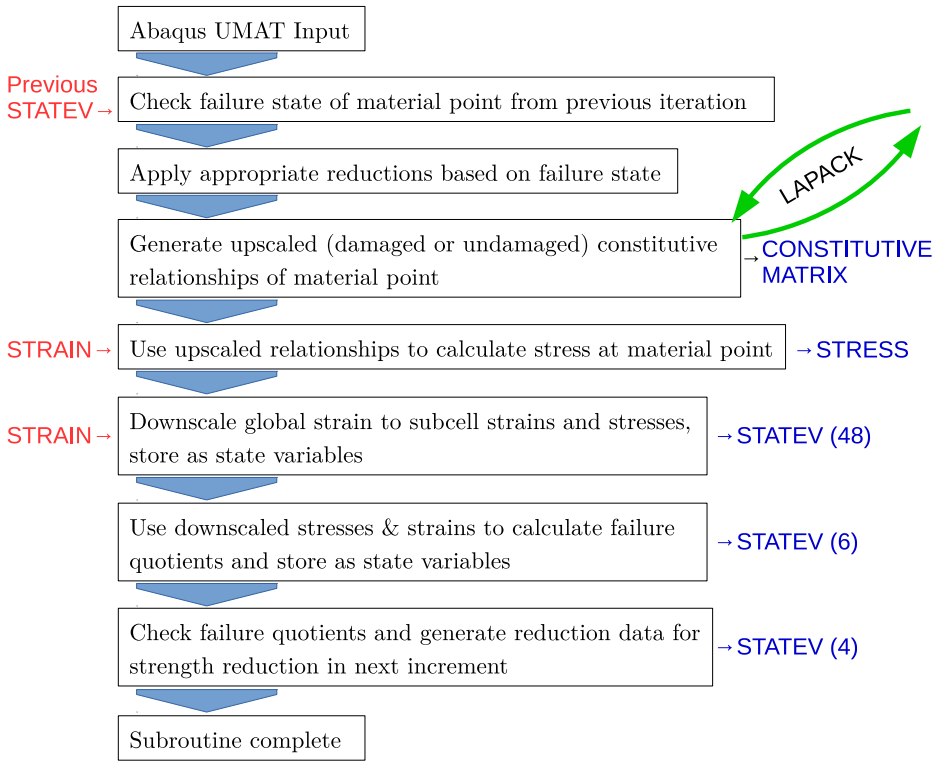

Figure 5.2. UMAT operational flow

(or previous) solution-step. The process uses the relationships in Chapter 2, equations 2.13 through 2.18 to decompose the global shear strains to subcell shear strains. For an undamaged composite, the calculation is straightforward, however for damaged composite, the routine degrades the shear modulus of the half-cell by the proportion indicated in the `failang` matrix.

5.2.2 Upscale

The upscale routine is accomplished following the formation of R during the downscale portion. The upscale calculation is the same calculation described in Section 2.5. The constitutive relationship defined by this upscale operation is then stored as a return variable to the finite element solver.

5.2.3 Damage Detection and Strength Reduction

The damage initiation subroutine uses Equations 3.1, 3.2, 3.8, 3.9, and 3.13 described before and the subcell stresses and strains calculated during the downscale portion to determine the damage initiation quotients. The fiber and interface quotients are calculations based on the stresses and strains; however, the matrix failure criterion relies on an additional subroutine that takes the subcell's strain tensor and calculates the principal strains for comparison to the matrix failure strain. This eigenvalue-solving subroutine is an implementation of the program found in Ungural and Fenster [21], Appendix B.

5.2.4 User-Defined Solution-Dependent State Variables

Crucial to the operation of the UMAT is the storage and reference to the state of the section point. The UMAT records all subcell strains and stresses at each increment for each section point. For large models, this storage, especially if written as a history variable, can become too large. The UMAT routine, which implements the micro model as well as the failure model with damage progression, currently stores all quarter-cell stresses and strains. In addition to storing the stresses and strains of the quarter-cell, the UMAT also computes and stores the general failure state and the individual values for each failure quotient. Lastly, it stores the three values for ζ, which control the value for `failang`, directly impacting the computed stiffness of the failed integration point/section point.

Also included in the state variables are the failure quotients from the six failure criteria (fiber, 34-interface, 56-interface, 34-matrix, 56-matrix, 78-matrix) and the previous solution increment failure state. These data (and the subcell stresses and strains used to compute them) are the essential data stored in the state variable array.

5.3 Conclusion

The link between the multiscale failure model and finite element software is now completed through the use of the UMAT. The UMAT framework also affords the flexibility for improvements to the failure model using multiscale calculations. In addition to identifying failure, the UMAT also includes the progressive failure logic and post-failure stiffness reduction technique. The next chapters use this UMAT formulation in FE software to reproduce failure envelopes described by WWFE data as well as data obtained by experiment.

CHAPTER 6:
Performance of Multiscale Model–WWFE Data

In order to test the performance of the user-defined material subroutine (UMAT) that implements the multiscale failure model, data provided in the WWFE by Hinton et al. [10] was used as a basis for comparison. Selected "tasks" from the WWFE were reproduced using the UMAT and the WWFE provided constituent material properties as the material definition. Both uniaxial and laminated composites were examined using the multiscale failure model.

6.1 Lamina Failure

A MATLAB program, and later an Abaqus finite element (FE) model were utilized to perform a radar-search in the envelope area incrementing the load along loading ratios until the failure criteria were met. The method then stored the failure stresses, reset the condition of the composite, increased the load ratio and began a new search along that ratio.

Most of the example cases were selected from the test data available in WWFE [10] to assess the proposed failure criteria under different loading conditions. The cases examined using the multiscale UMAT were:

1. Uniaxial E-Glass LY lamina under combined $\sigma_y - \tau_{xy}$
2. Uniaxial Hercules 55A lamina under combined $\sigma_y - \tau_{xy}$ (not in WWFE)
3. Uniaxial AS4 lamina under combined $\sigma_x - \tau_{xy}$
4. Uniaxial E-Glass MY lamina under combined $\sigma_x - \sigma_y$
5. E-Glass [90,$\pm 30_s$,90] laminate under combined $\sigma_x - \sigma_y$
6. E-Glass [90,$\pm 30_s$,90] laminate under combined $\sigma_x - \tau_{xy}$

The finite element models of the uniaxial test specimen were constructed of a thin rectangular coupon meshed with C3D20 brick elements. The material properties for the UMAT were assigned to the elements. The sample was loaded in 10 steps along various load ratios. This was automated with a Python script to enable multiple runs and efficient data collection. The failure criteria outputs of a central element were extracted, and for each load ratio stress

locations were linearly interpolated for where the criteria were satisfied. The finite element generated data corresponded well with the MATLAB generated script data.

6.1.1 Lamina Failure under Combined σ_y and τ_{xy}

This first example case used a uniaxial lamina constructed with E-Glass fibers and the LY556 resin material. The lamina was subjected to simultaneous loading of transverse normal and shear. In this loading configuration, the active criteria are the fiber/matrix interface debonding and matrix cracking. Because there is no longitudinal normal loading, fiber failure is not plausible. The material properties used in this example are listed in Table 6.1.

Figure 6.1 compares the present prediction to the experimental data. The criterion was successful in its representation of the experimental data. The first quadrant contains the failure due to tensile transverse normal stress ($\sigma_y/\sigma_\perp$ term). The second quadrant shows the peak where the fiber/matrix interface failure and the matrix failure curves intersect. This curve is very similar to the curve in Figure (20) of Section 3.4 of Skudra's text [26]. His formulations for what this research calls "interface failure" are very similar in that they are interactive criterion between transverse and shear stresses, and account for differences between transverse tension and compression. However, Skudra's form of matrix failure criteria is based on the specific work done by the maximum principal stress.

The matrix failure line can be manipulated by changing how the shear strain value is calculated. The matrix material tensor for the 34 quater-cell, described in Chapter 3 and repeated here:

$$\boldsymbol{\varepsilon}^{34} = \begin{bmatrix} \varepsilon_x^{34} & \gamma_{xy}^{34}+\gamma_{xy}^{78}/4 & 0 \\ \gamma_{xy}^{34}+\gamma_{xy}^{78}/4 & \varepsilon_y^{34} & 0 \\ 0 & 0 & \varepsilon_z^{34} \end{bmatrix}$$

This tensor highlights that the shear value calculated in the tensor is the average of adjacent subcells. The current theory can give a moderately conservative value by averaging the shear strain between the 34 quarter-cell and the 78 quarter-cell, a worst-case (conservative) estimate can be made by using the shear strain in the 34 quarter-cell only and an optimistic estimate can be made by using the shear strain in the 78 quarter-cell only. The three lines described by this are compared in Figure 6.2. This averaging is most useful to overcome

Table 6.1. Constituent and composite material properties

		E-Glass 21xK43 Gevetex	LY556/ HT907/ DY063	Comp.	E-Glass Silenka 1200tex	MY750/ HY917/ DY063	Comp.	T300	BSL914C	Comp.	55A/ AS4	EPON826	Comp.	T700	UF3325	Comp.
E_1	GPa	80	3.35	53.48	74	3.35	45.6	230	4	138	225		126	230	2.8	170
E_2	GPa	80		17.7	74		16.2	15		11	15			15		
G_{12}	GPa	33.33	1.24	5.83	30.8	1.24	5.83	15	1.481	5.5	15	1.567		0.2		
ν_{12}	–	0.2	0.35	0.278	0.2	0.35	0.278	0.2	0.35	0.28	0.2	0.34				
G_{23}	GPa	33.33			30.8			7			7			7		
$\sigma_{1,T}$	MPa	2150	80	1140	2150	80	1280	2500	75	1500	3350	50		4900		2100
$\sigma_{1,C}$	MPa	1450	120	570	1450	120	800	2000	150	900	2500	80				1450
$\sigma_{2,T}$	MPa			35			40			27	1.488		26			31
$\sigma_{2,C}$	MPa			114			145			200			94.3			
τ_{12}	MPa			72			73		70	80		50	55			
$\varepsilon_{1,T}$	%	2.687	5	2.132	2.905	5	2.807	1.086	4	1.087	1.488	1.7		2.1	4.5	1.7
$\varepsilon_{1,C}$	%	1.813	*	1.065	1.959		1.754	0.869		0.652	1.111	2.52				
$\varepsilon_{2,T}$	%			0.197			0.246			0.245			0.265			
$\varepsilon_{2,C}$	%			0.644			1.2			1.818			1.21			
γ_{12}	%			3.8			4			4			1.92			
v_f	%			0.62			0.6			0.6			0.6			0.7
$\varepsilon^f_{u,T}$	%			2.687			2.905			1.086			1.488			1.297
$^*\varepsilon^f_{u,C}$	%			1.813			1.748			0.645			1.058			0.896
$\sigma_\perp$	MPa			43.2			40			27			94.3			34.9
τ_u	MPa			72			88			92			79			117.6
$\varepsilon^m_{u,T}$	%			2.687			2.905			1.086			1.7			2.82
$\varepsilon^m_{u,C}$	%			1.813			1.959			0.869			2.52			4.5
		*** [10]			*** [10]			*** [10]			*** [10], [22], [23]			*** [24], [25]		

** Note that the calculation for $\varepsilon^f_{t,C}$ is done using the compression anchor point.

** The transverse $\sigma_\perp$ uses the transverse anchor point.

** The shear value τ_u uses the shear strength; however, is usually greater than τ^C_u by a factor of 1.1 to 1.5.

the shortcoming of the theory that allows for shear-strain discontinuities between half-cells described in 2.1.2.

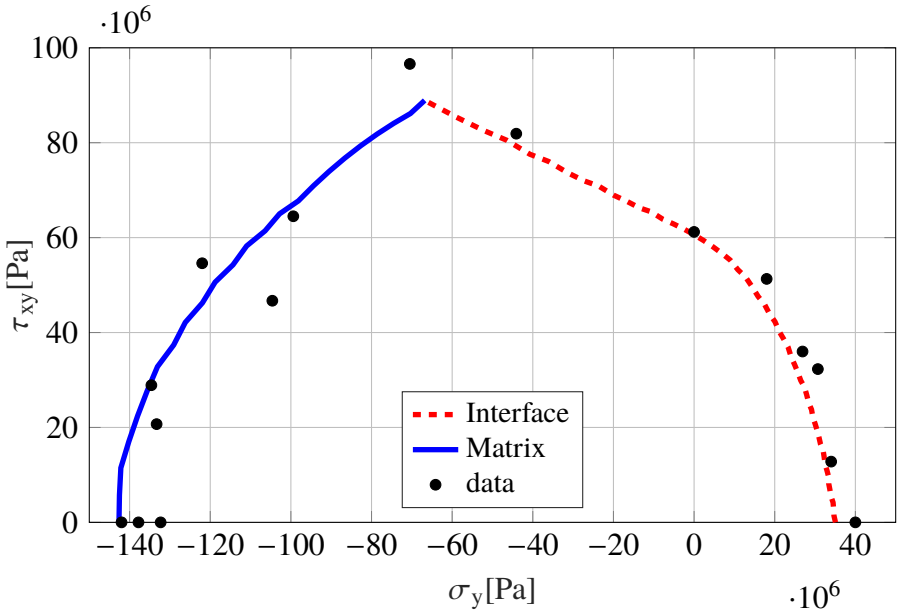

Figure 6.1. Failure comparison for E-Glass/LY556 under σ_y and τ_{xy} (MATLAB simulation)

A parametric study was also conducted to investigate the effect of the α_1 coefficient used in Equation 3.8, repeated here:

$$\left(\frac{\tau^I + \alpha_1(\sigma_y^{34} - \sigma_x^{34})}{\tau_u}\right)^2 + n\left(\frac{\sigma_y^{34}}{\sigma_\perp}\right)^2 \geq 1$$

Figure 6.3 shows the comparison for different α_1 values. When the value is zero, there is no effect of the compressive transverse normal stress on the failure, which poorly represents the test data. When α_1 is selected to be the square root of the fiber volume fraction, the fiber/matrix interface failure criterion agreed well with the experimental result. The final choice of α_1, however should be one that provides satisfactory representation of the failure envelopes in all three stress spaces ($\sigma_x - \sigma_y$, $\sigma_x - \tau_{xy}$, and $\sigma_y - \tau_{xy}$)

The general trend by the data shows the previously discussed promotion of shear failure under transverse tension and the delay of shear failure under transverse compression. The criterion adequately accounts for this trend.

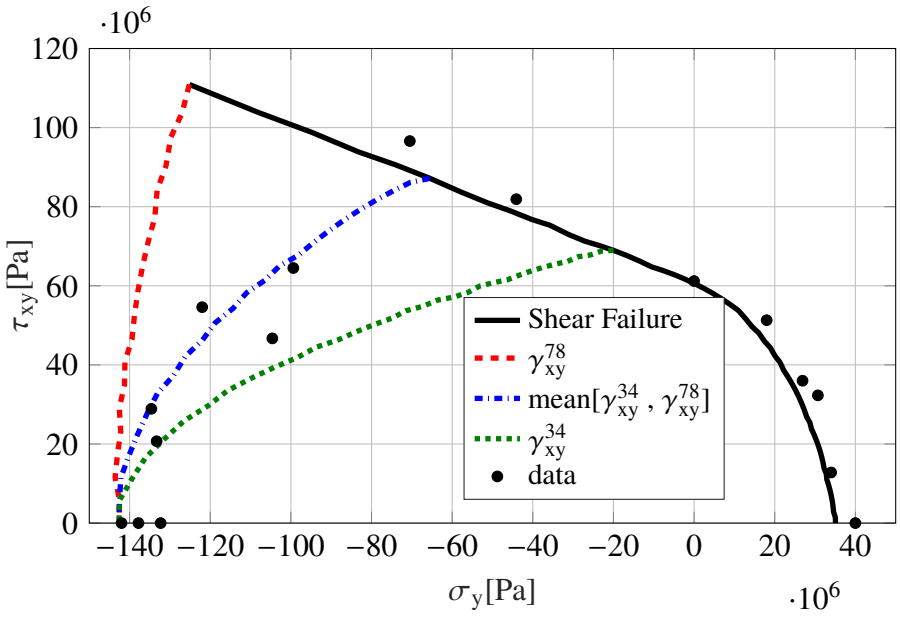

Figure 6.2. Effect of choice of shear strain for E-Glass/LY556 under σ_y and τ_{xy}

A second example for the $\sigma_y - \tau_{xy}$ space, which was not a part of the WWFE tasks, applied additional multi-axial loading to tubular specimens so as to determine failure data for AS4/55A [22] whose properties were similar to the AS4/3501-6 composite. The resin properties, however, needed to be adjusted to match the replacement resin. The properties of Hercules 55A were estimated using [23] and [27].

The compressive strength for Hercules 55A under pseudo-static loading indicated to be 80MPa. The failure strain was determined from its failure strength divided by its elastic modulus because the resin is almost linear up to failure. Based on the elastic modulus 3.15GPa, the failure strain was determined to be 2.5%. These values are reasonable for most resin/hardener combinations, some cure schedules and for room temperature testing. Table 6.1 shows the material properties used in the analysis.

Figure 6.4 shows the comparison of the experimental data to the present prediction for AS4/55A. The value for α_1 was also determined from the fiber volume fraction. Both results agreed very well showing the effect of the transverse normal stress on the fiber/matrix interface failure as suggested in the failure criterion.

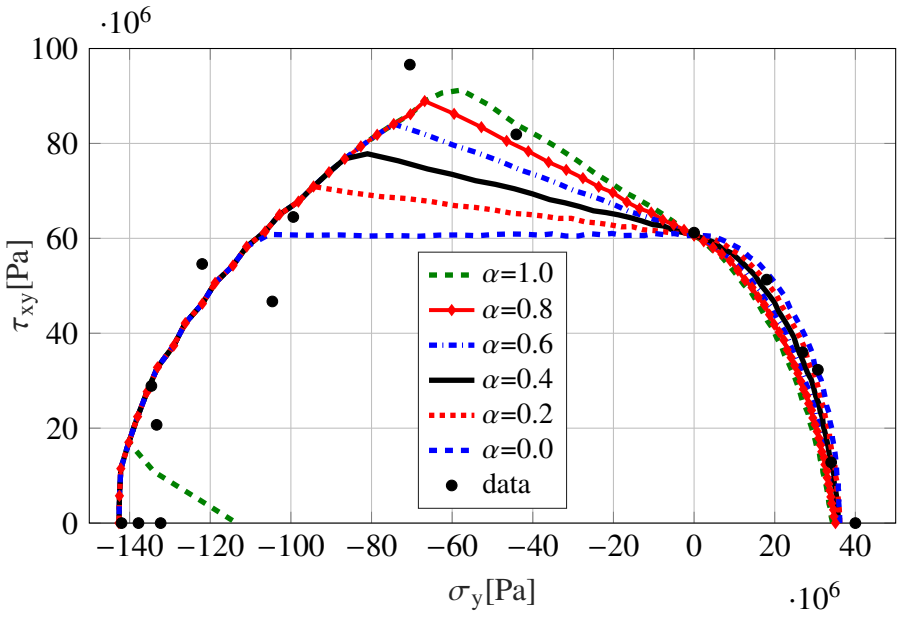

Figure 6.3. Effect of choice of α_1 for E-Glass/LY556 under σ_y and τ_{xy}

6.1.2 Lamina Failure under Combined σ_x and τ_{xy}

The second task in [10] applied longitudinal normal stress and in-plane shear stress to the T300/BSL914C composite. The material properties are provided in Table 6.1. The longitudinal normal stress failure varied from tension to compression. In this example, three failure modes were active. The first two are fiber breakage in tension and fiber buckling in compression. The third mode is fiber/matrix interface failure.

Figure 6.5 shows the failure envelope along with experimental data. As discussed previously, the shear stress influenced the fiber failure for both tensile and compressive longitudinal stress. When the longitudinal normal stress is not large enough for fiber failure, the fiber/matrix interface failure was the failure mode. The test data were quite scattered; despite this scattering however, the prediction fairly represented the data.

The effect of α_1 was also examined for the interface failure criterion as shown in Figure 6.6. As before, the same choice of $\sqrt{v_f}$ was used. Overall, the predicted results agreed well with the experimental data.

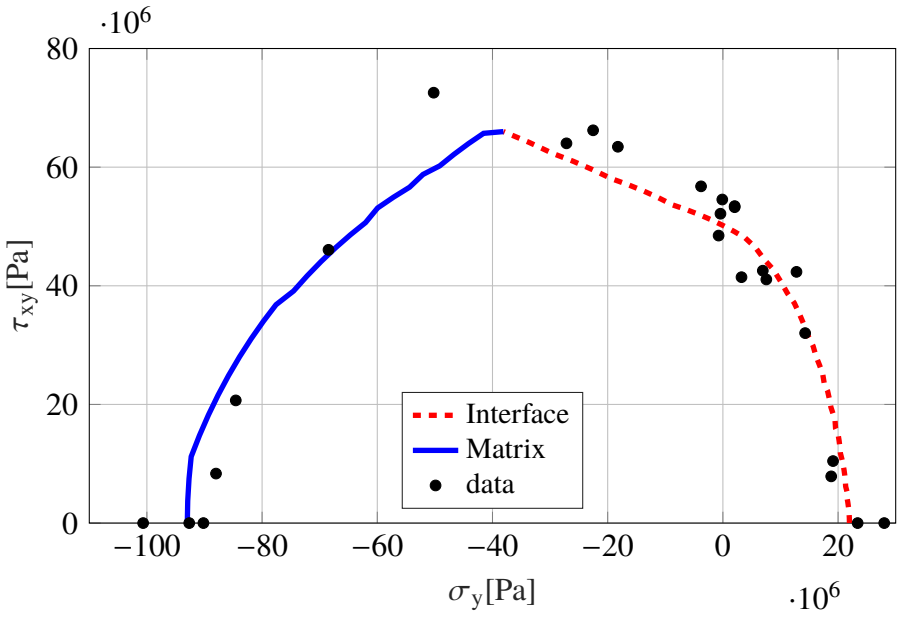

Figure 6.4. Failure comparison for AS4/55A under σ_y and τ_{xy} (MATLAB simulation)

6.1.3 Lamina Failure under Combined σ_x and σ_y

The third case tested for lamina was the E-Glass/MY750 composite which was subjected to normal stresses in both longitudinal and transverse stresses, i.e., biaxial loading. The material properties are given in Table 6.1. In this example, all possible failure modes could be considered such as fiber breakage, fiber buckling, fiber/matrix interface failure, and matrix cracking. When the longitudinal normal stress was either large in tension or compression, the failure mode was fiber breakage or buckling. Otherwise, depending on the direction of the transverse normal stress, matrix cracking or fiber/matrix interface debonding occurred. Figure 6.7 plots the results, which compare the present results to the experimental data. The proposed failure criteria predicted the failure reasonably well. In addition, the effect of α_1 was also explored, as shown in Figure 6.8. The same choice of $\sqrt{v_f}$ was used for α_1.

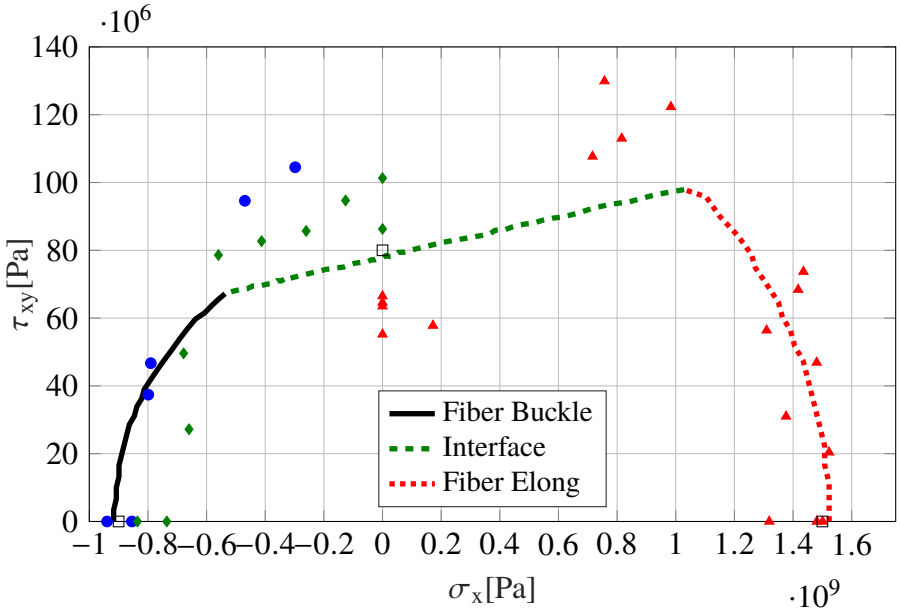

Figure 6.5. Failure comparison for T300/BSL914C under σ_x and τ_{xy} (MATLAB simulation)

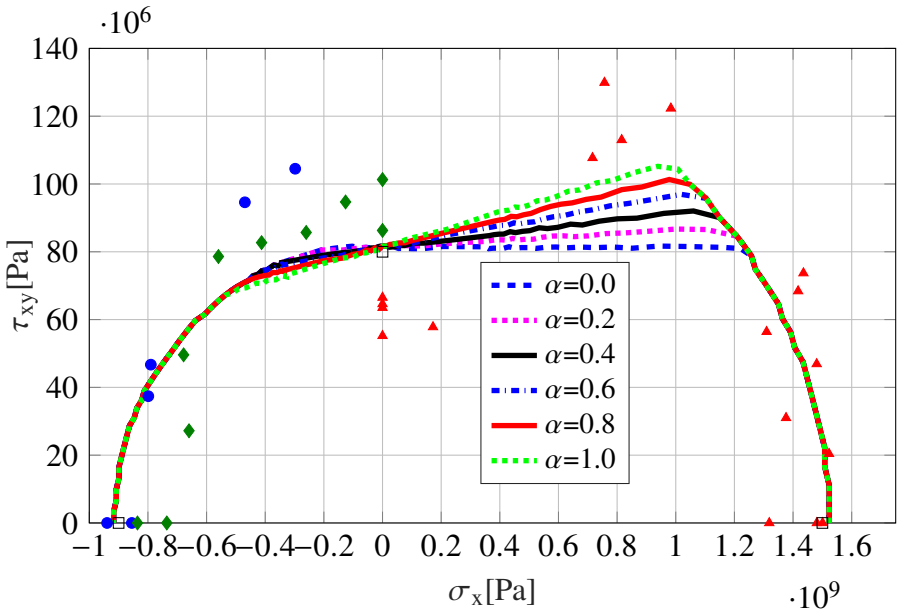

Figure 6.6. Effect of choice of α_1 for T300/BSL914C under σ_x and τ_{xy}

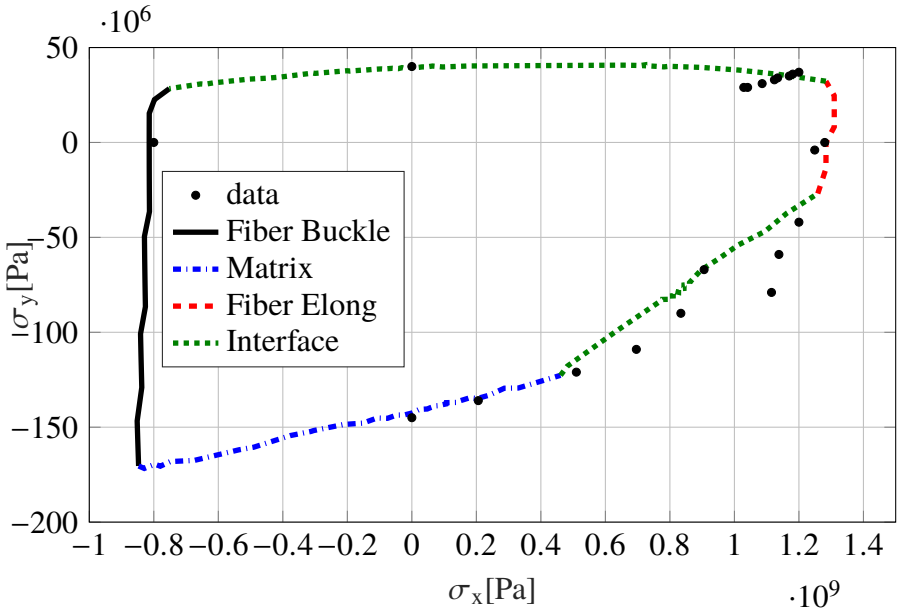

Figure 6.7. Failure comparison for E-Glass/MY750 under σ_x and σ_y

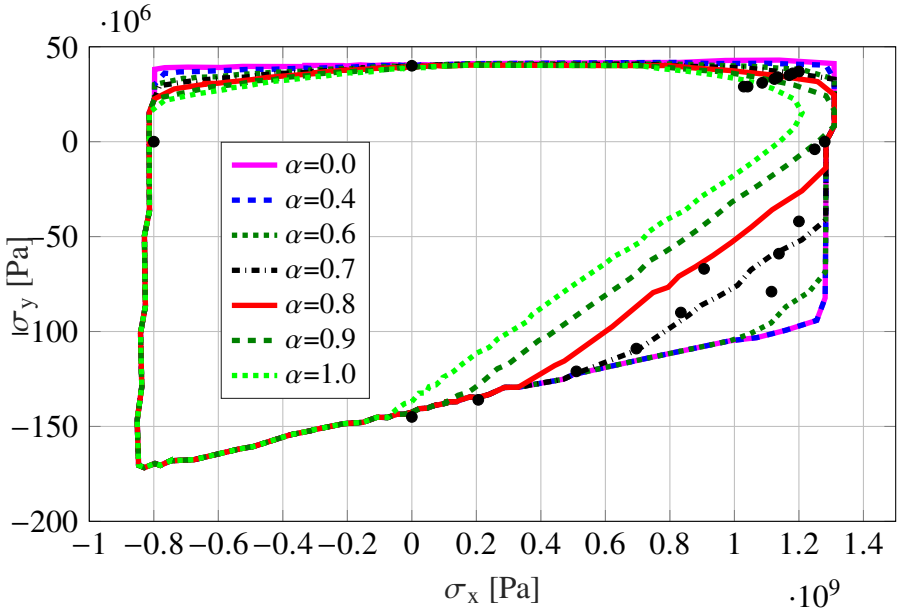

Figure 6.8. Effect of choice of α_1 for E-Glass/MY750 under σ_x and σ_y

6.2 Laminate Failure

The above investigations are used as a preliminary step to describing the failure of a composite laminate where reinforcement orientations vary. In addition to the uniaxial failure envelopes, the WWFE also required its participants to examine multi-angle laminates under varying load conditions. The Chapter 3 criteria were applied to these data as well.

6.2.1 Construction

In the Abaqus software, the test sample was constructed from a 20mm square 2mm wide sample. To represent the composite layup, a few options are available. First, the sample can be a shell section with section properties of a composite layup. In this instance, the UMAT contains logic to return a planar stiffness matrix rather than the upscaled three-dimensional matrix.

The second choice is the use of stacked shell elements (in Abaqus, a "continuum shell") which can be used when normal forces are important on a shell section. In this case, one would also include a composite layup in the Composite Layup dialog. The third option is the use of a single brick element for the entire thickness. Like the shell section, this 3D element also can be given the section properties by using the Composite Layup dialog.

Lastly, the sample can be specifically partitioned by composite layer and the properties of the composite can be identified in the Composite Layups dialog. As an alternative to the Composite Layup dialog, the user can apply the UMAT by indicating the section properties as defined in the UMAT with the orientations of the material identified separately in the Orientations dialog.

6.2.2 Laminate failure of $[90, +30, -30]_s$ under combined σ_x and σ_y

The first laminate explored from the data in the WWFE was a dataset originally from Hütter et al. [28], filament wound E-Glass cylinder under longitudinal and transverse stress. While the laminate is denoted $[90, +30, -30]_s$ the thicknesses of the layers as described in [10] indicate that a more accurate representation would be $[90, +30_2, -30_2]_s$. The correct relative thicknesses were used in the finite element simulations.

Boundary Conditions

For the normal loading case, the 20 mm by 20 mm sample described above was constrained on the negative x and y boundaries using symmetry conditions (`u1=ur1=ur3=0` for x, `u2=ur2=ur3=0` for y). The mid-plane of the sample was also constrained to zero motion in the z direction (`u3=0`).

Additionally, the motions of the nodes on each of the positive x and y faces were coupled such that all nodes on either face would all have the same displacement. This would reduce artifacts of excessive displacement of nodes due to potentially fictitious failures on the edges of the sample under test. A schematic of the imposed condition is shown in Figure 6.9.

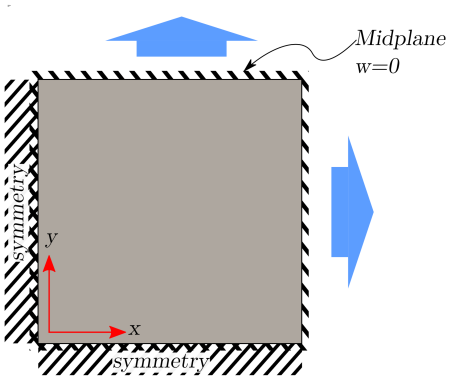

Figure 6.9. Boundary conditions applied to the normal FE composite model

Loading Methodology

To load the sample, two different methods were used. First, pressure loads were applied to the positive x and y faces of the sample. The second loading type uses imposed displacement of the nodes on the positive x and y faces. The imposed displacement method is more difficult to ensure a defined loading ratio, and therefore the primary mode of loading in the finite element model was defined pressure. The pressure method better mimics the load-controlled test described in [28]. The loading scheme can also be seen in Figure 6.9.

Failure Indications & Failure Envelope

Potential indications of composite failure are available as computed outputs in this formulation. As an additional output, the failure quotients are stored as Solution Dependent State variables calculated in the UMAT subroutine. In the case of pressure/force loading, the

strain radius, marginal strain and the change of marginal strain (d^2r_ε/dl^2) of telltale elements was used to measure final sample failure. These measures highlight the point along the loading ratio where the rate of displacement changes most, an area indicating potentially significant decreases in sample strength. Alternatively, particular types of failures can be monitored by requiring the output of the failure quotient or quotients of areas of concern.

For the $[90, \pm 30]_s$ laminated composite under normal loading, Figure 6.10 shows contour plots of (a) the strain radius, r_ε, (b) marginal strain, dr_ε/dl, and (c) change in marginal strain d^2r_ε/d^2. These plots illustrate the evolution of these variables as loading and composite failure progresses. The "ultimate value" is assumed to be where these curves converge, indicating the onset of large strains for relatively small increases in load. The plots in Figure 6.10 stop at these converged values, the next increment provides no appreciable increase in the envelope. For Figure 6.10 (a), r_ε converges at approximately 0.04, for (b) dr_ε/dl converges at approximately 0.1 and (c) d^2r_ε/dl^2 converges at 1.2. These final curves are plotted together in Figure 6.11 providing an estimated failure envelope using the strain radius as a basis.

The envelopes plotted in Figure 6.11 provide a relatively good representation of the experimental data. The marginal strain and change of marginal strain (first and second derivatives of r_ε) are qualitatively better estimates than r_ε, whose converged values give an overestimate of the failure envelope. Choosing a more conservative value for r_ε than the converged value can plot an envelope more consistent with marginal strain and change of marginal strain.

Some loading ratios are relatively poorly represented, and over-predict the failure in comparison to the data. The transverse tension half-space is very well represented by the failure model results, despite some scattering in the data in the middle tension-tension loading ratios. The finite element simulations provide an improvement over the previous MATLAB simulation envelope. This improvement is due to an improvement in the failure detection logic and improved material degradation calculations in the UMAT subroutine. The finite element models impose complications associated with edge loading and boundary conditions not present in the simple homogenized MATLAB scripts; however, the improved logic and the ability to model more complex structures and interactions are a significant benefit to the use of the UMAT in finite element code.

The failure load prediction of the laminate in transverse compression is 90% larger than the data indicates. Additionally the biaxial compression regime is similarly over-predicted. This may be due to the sample buckling rather than material failure. While Hütter [28] manufactured shorter samples to avoid longitudinal buckling before material failure, transverse buckling of tubular specimen can occur at much lower pressures than material failure, particularly in the presence of manufacturing irregularities. These irregularities may have caused primary mode buckling (transverse failure of the laminate) before material failure. Figure 26 of [28] also assumes that the fourth quadrant data may be sample buckling rather than material failure. As a check of this assumption, the compression cylinder described in Hütter et al. [28] was modeled with the multiscale UMAT. A linear buckling analysis of this model with internal pressure only was conducted, and indicated that the buckling load was 112 MPa (compression), approximately the values given in the WWFE (Figure 6.12). While it is not conclusive that the failure points in the negative σ_y half-plane are a result of sample buckling, it is likely that buckling, indicated at the same load as the provided failure load, plays a significant role in the data set.

Figures 6.13 through 6.15 illustrate the individual failures of the plies in relation to the data from Hütter [28] and Hinton [10]. The outer data points in the transverse tension half-plane appear to coincide with the experimental data in [28] as a cascading failure. The data points in the transverse compression half-plane show the overprediction discussed earlier.

Of note is the relatively early indication of interface failure for all plies in transverse tension. It is unknown whether this failure actually occurs, however using the change of strain radius as an indication of failure, this failure–actual or not–and its associated reductions do not contribute significantly to a large increase in strain following the indication of failure. Additional experiments can be conducted to determine whether failure is actually occurring.

Similar experimental observations of Lissenden et al. [29] who conducted repeated loading tests on $[\pm 45]_s$ cylinders. Their test program repeatedly loaded SiC/Ti composite tubes with increasing axial and moderate shear loads. They noted small amounts of residual shear strain midway through the test sequence after only reaching 30% of the ultimate axial load, which they attributed to "interfacial slippage." Repeated loading tests like those described by Lissenden et al. would aid in determining whether the interface failure lines in Figures 6.13 ff. are true indications of failure.

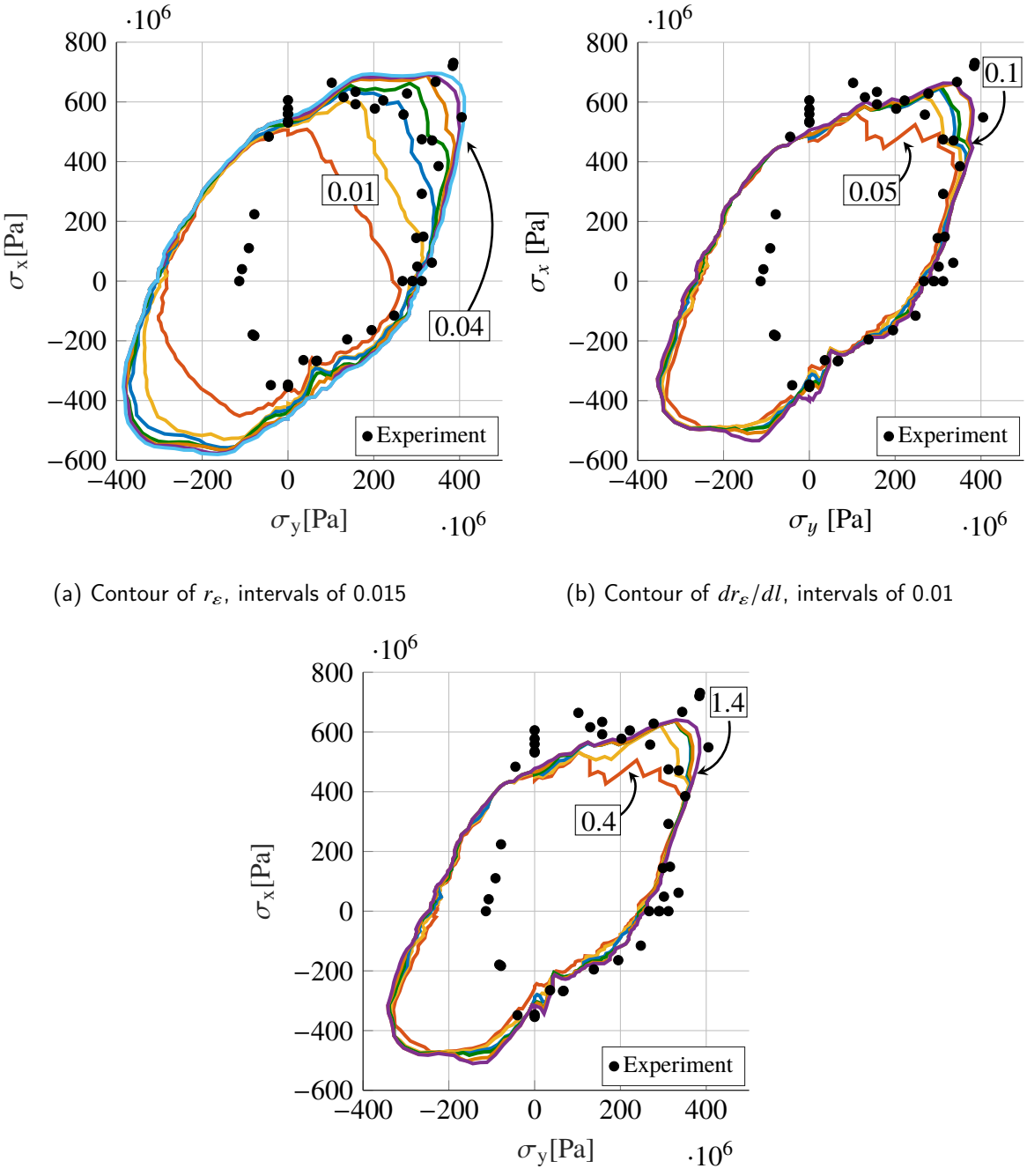

(a) Contour of r_ε, intervals of 0.015

(b) Contour of dr_ε/dl, intervals of 0.01

(c) Contour of d^2r_ε/dl^2, intervals of 0.2

Figure 6.10. Contour plots for laminate normal loading

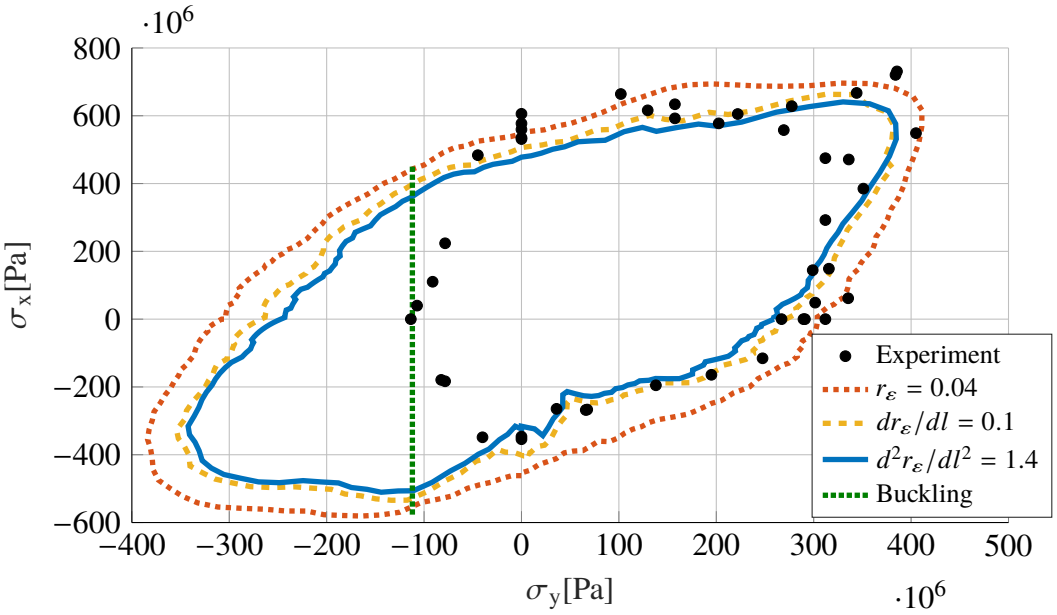

Figure 6.11. Failure of $[90, \pm 30]_s$ under combined $\sigma_x - \sigma_y$ loading, predicted by r_ε

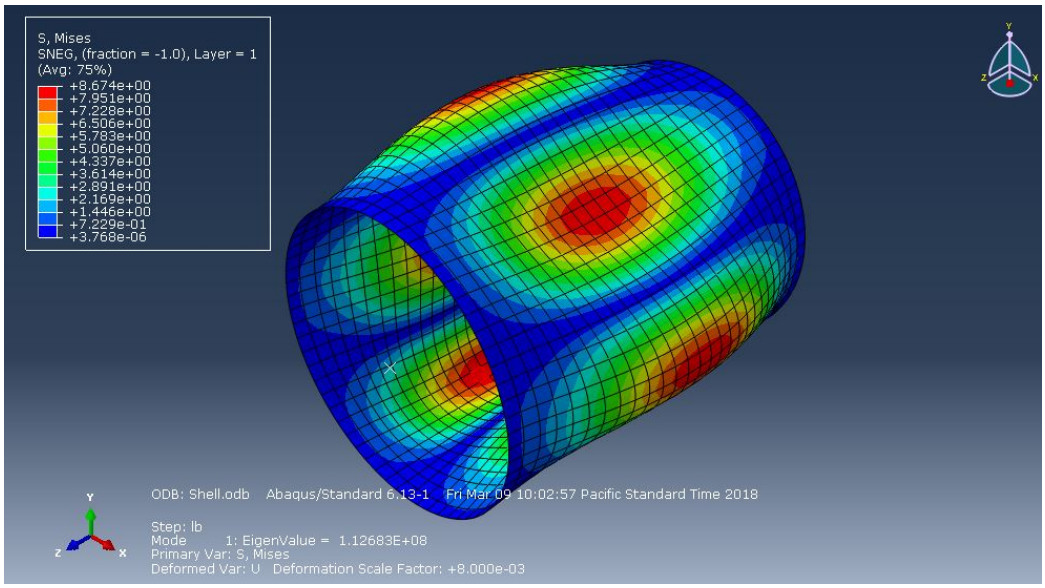

Figure 6.12. Results of linear buckling analysis of cylinder under internal pressure

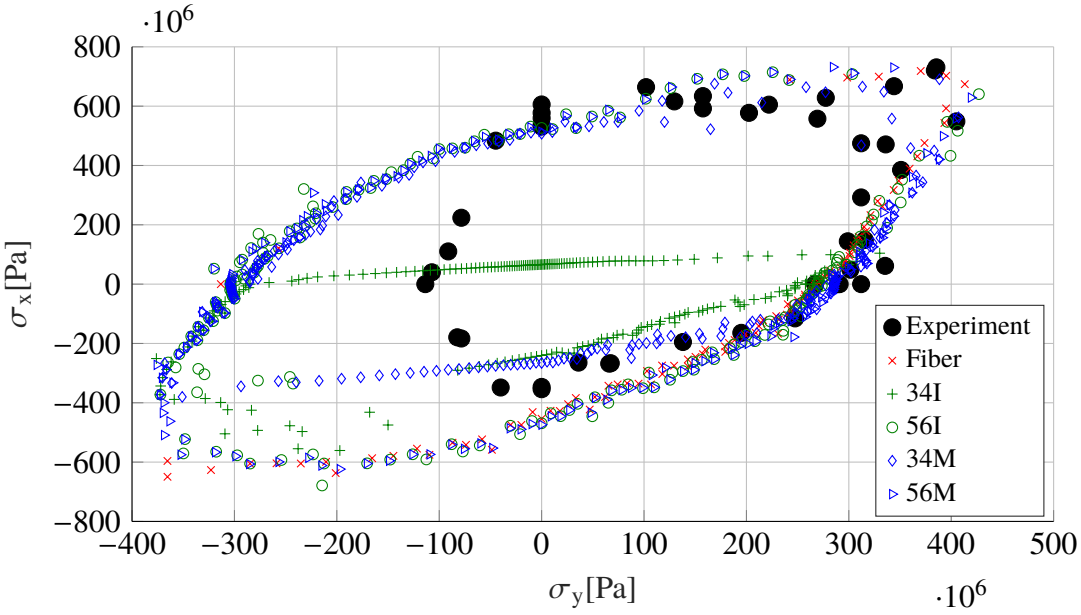

Figure 6.13. Individual failures for normal loading in 90-degree ply from Abaqus

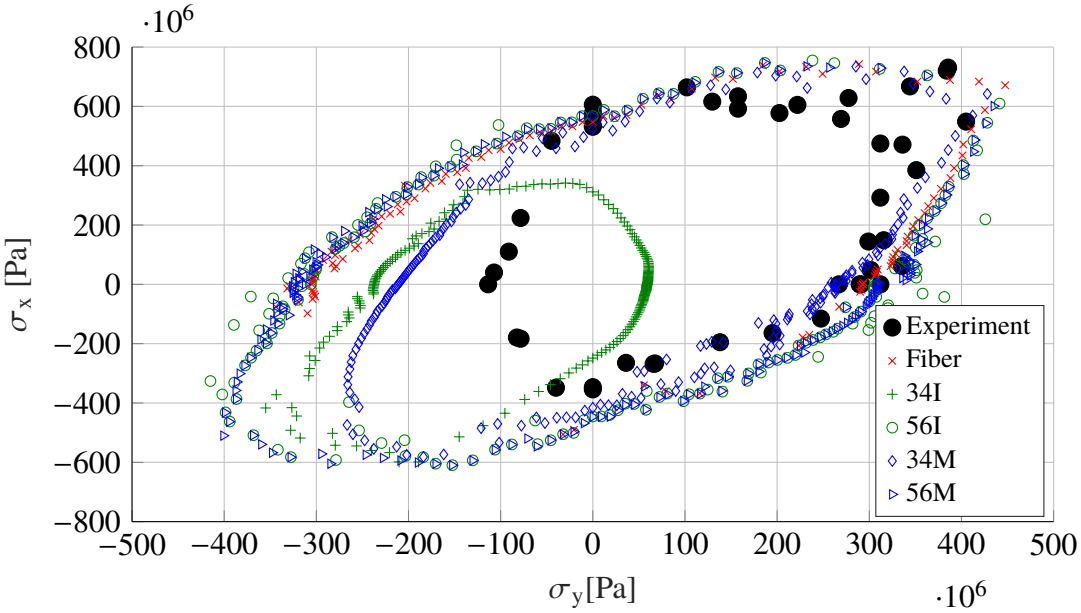

Figure 6.14. Individual failures for normal loading in +30-degree ply from Abaqus

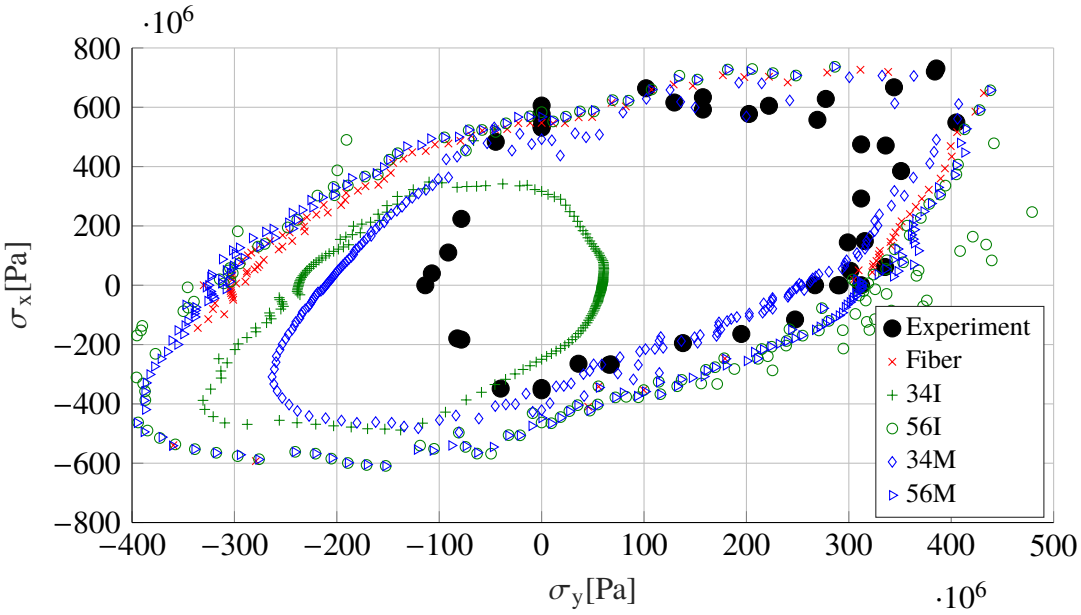

Figure 6.15. Individual failures for normal loading in -30-degree ply from Abaqus

6.2.3 Laminate failure of $[90, +30, -30]_s$ under combined σ_x and τ_{xy}

The second laminate case for E-Glass in [10], Task 5, was the same layup described above subjected to combined σ_x and τ_{xy}. Hütter et al. [28] used the same samples for both normal and shear testing.

Boundary Conditions

Boundary conditions used in the shear test model were such that the center nodes were pinned so their displacement in x and y were zero (`u1=u2=0`) and the mid-plane of the sample was constrained in the z direction (`u3=0`). An illustration of the boundary conditions imposed is shown in Figure 6.16.

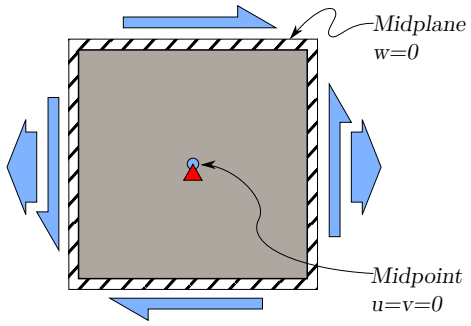

Figure 6.16. Boundary conditions applied to the normal and shear FE composite model

Sample Loading

The sample was loaded with equal pressure, applied normal to the positive and negative x faces of the sample as well as surface tractions applied tangentially to the positive and negative x and y faces. The loading is also illustrated in Figure 6.16.

Failure Indications & Failure Envelope

As with the normal loading case, the ultimate failure discriminator can be converged values of the strain radius, r_ε, or its derivatives. Figure 6.17 contains three contour plots of the progression of r_ε during sample loading. For Figure 6.17 (a), r_ε converges at approximately 0.014, for (b) dr_ε/dl converges at approximately 0.07 and (c) d^2r_ε/dl^2 converges at 1. These final curves are plotted together in Figure 6.11 providing an estimated failure envelope using the strain radius as a basis.

The failure model produced a moderately faithful representation of the test data shown in Figure 6.18. While the failure prediction is not necessarily a smooth curve, the failure model reproduces the features highlighted by the experimental data: longitudinal failure strength, transverse failure strength and the curved transition features in the remainder of the plane. The finite element representation shows a similar performance from the MATLAB model.

Figures 6.19 through 6.21 illustrate the individual failures of the plies in relation to the data from Hütter [28] and Hinton [10]. The individual ply failure plots again show where the multiscale failure model indicate particular failures in particular plies. Their collective representation of the experimental data is very good, however they appear to over predict failures in pure shear. The apparent over prediction is not necessarily reflected in the strain radius plots in Figure 6.17, which shows that the strain radius and its derivatives these areas does capture the earlier shear failure as shown in the experimental data.

Of note are features in Figures 6.19 and 6.21, discussed also in the normal envelope individual failure plots (Figures 6.13 through 6.15), namely the relatively early indication of interface failure in the 90-degree and 34 matrix failure (likely the same failure) in Figure 6.19 and interface failure only in Figure 6.21. These failures, whether they are actual or not, do not appreciably impact the converged values of strain radius or its derivatives sufficiently as to indicate that the composite has failed. These features are absent in the +30-degree ply likely due to the fact that the composite is under positive shearing and normal load so the principal stress is in closer alignment with the orientations of the +30-degree fibers.

6.3 Conclusion

The multiscale failure model provided reasonably successful representations of the failure envelopes for a wide variety of fibrous composites—varying in both material and construction. Shortcomings of the outputs, namely over prediction of failure stresses in some stress regions and an earlier-than-expected prediction of interface failures in others, require more analysis. Overall, the performance of the implementation to this dataset was encouraging. Comparisons to additional datasets is also desired. The following section describes experiments designed to further explore the performance of the multiscale failure model under different experimental circumstances.

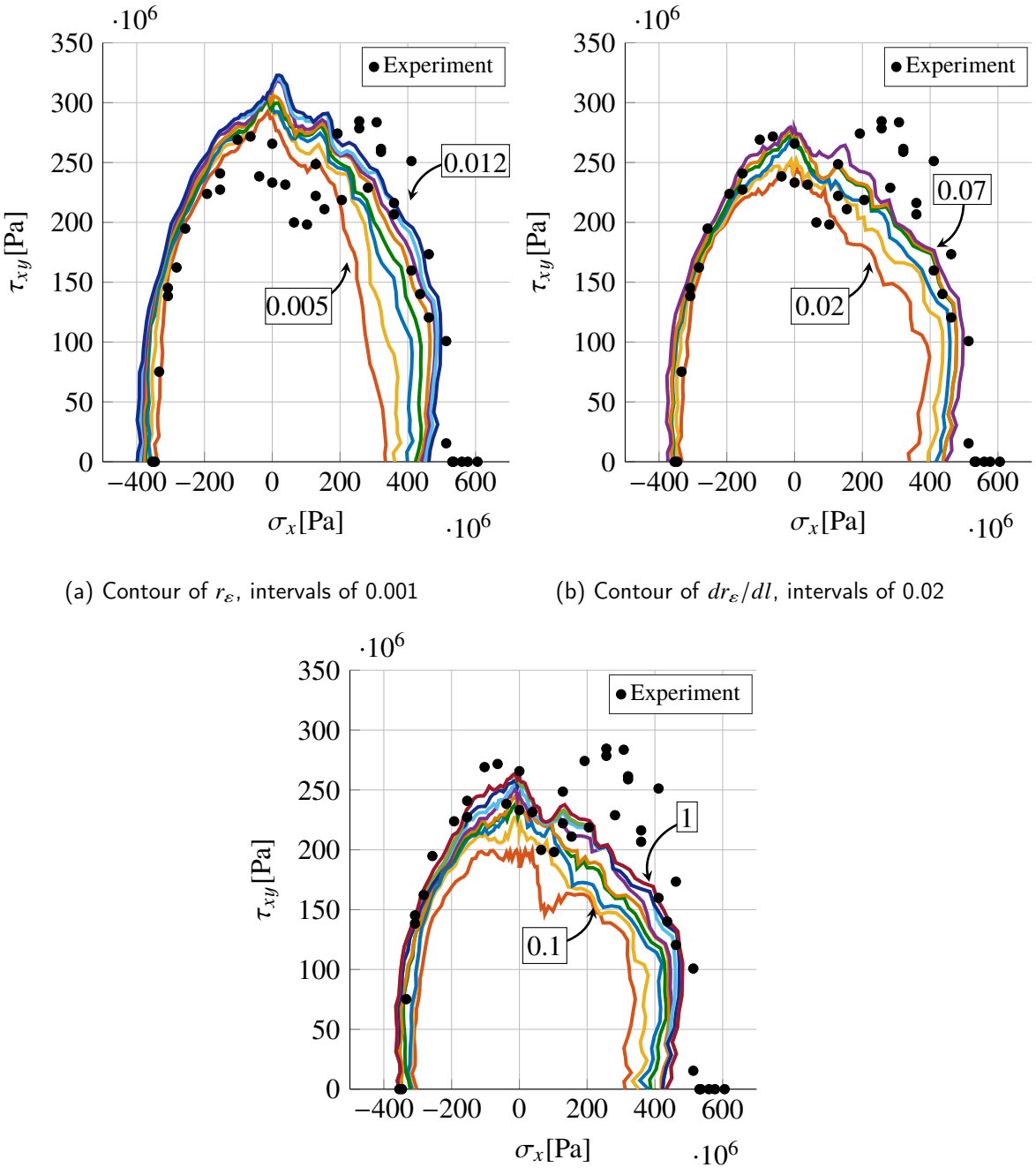

(a) Contour of r_ε, intervals of 0.001

(b) Contour of dr_ε/dl, intervals of 0.02

(c) Contour of d^2r_ε/dl^2, intervals of 0.1

Figure 6.17. Contour Plots shear

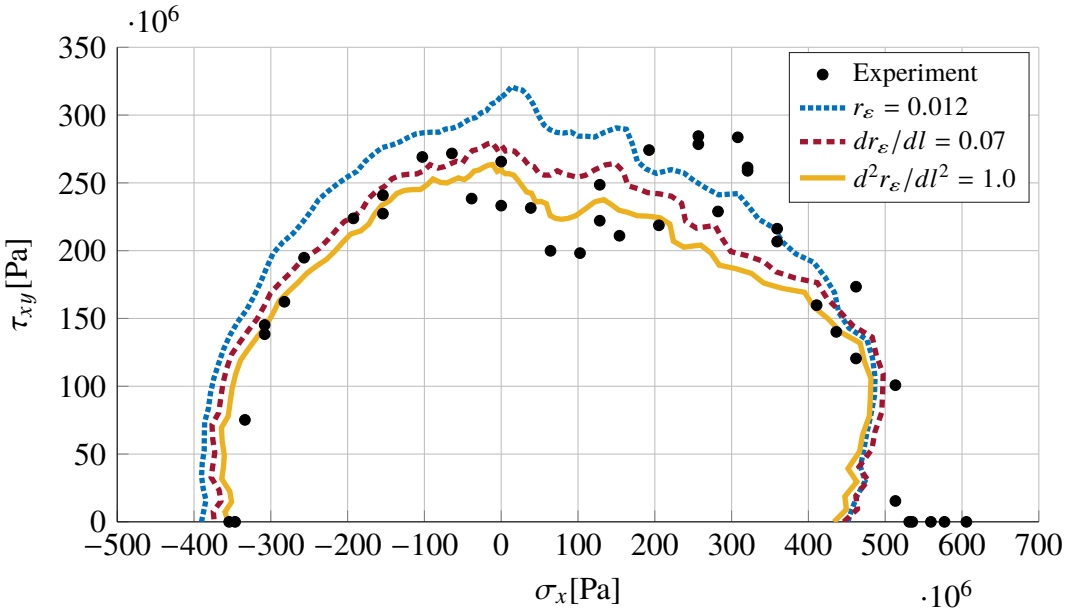

Figure 6.18. Failure of $[90, \pm 30]_s$ under combined $\sigma_x - \tau_{xy}$ loading predicted by r_ε

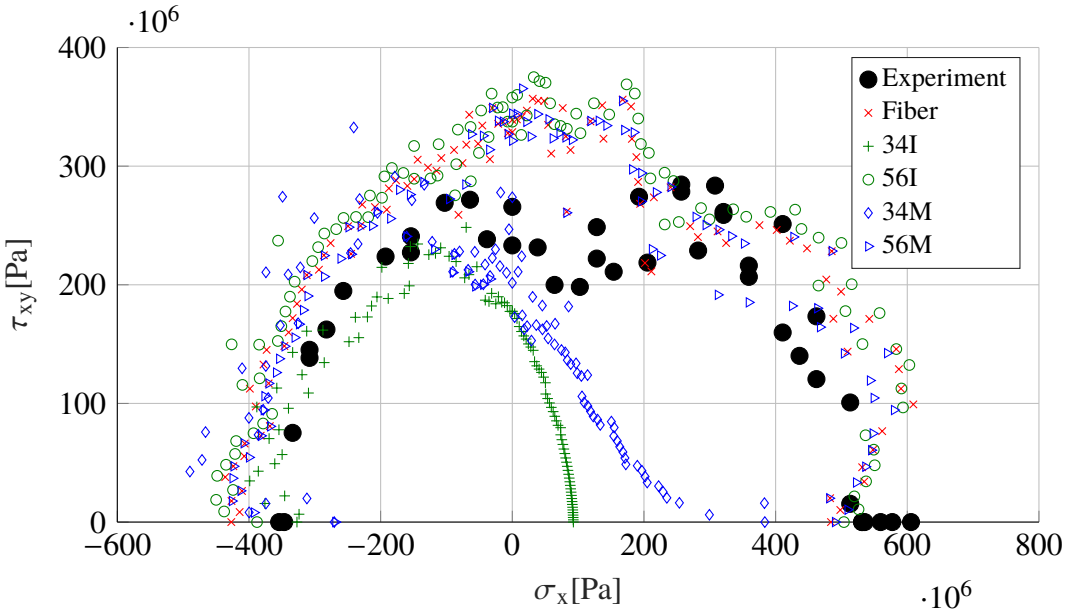

Figure 6.19. Individual failures for normal and shear loading in 90-degree ply from Abaqus

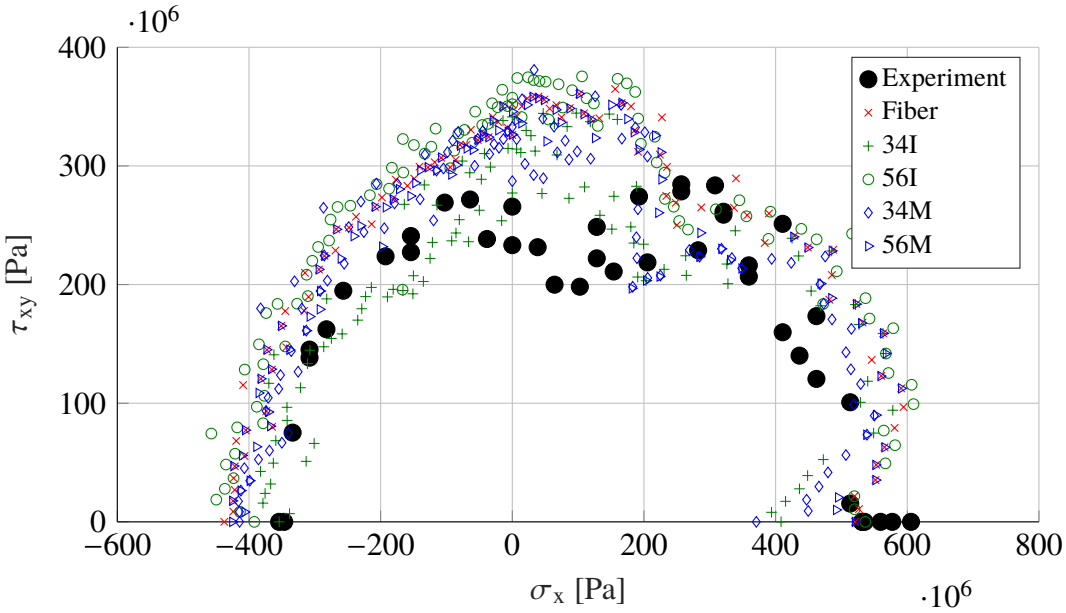

Figure 6.20. Individual failures for normal and shear loading in +30-degree ply from Abaqus

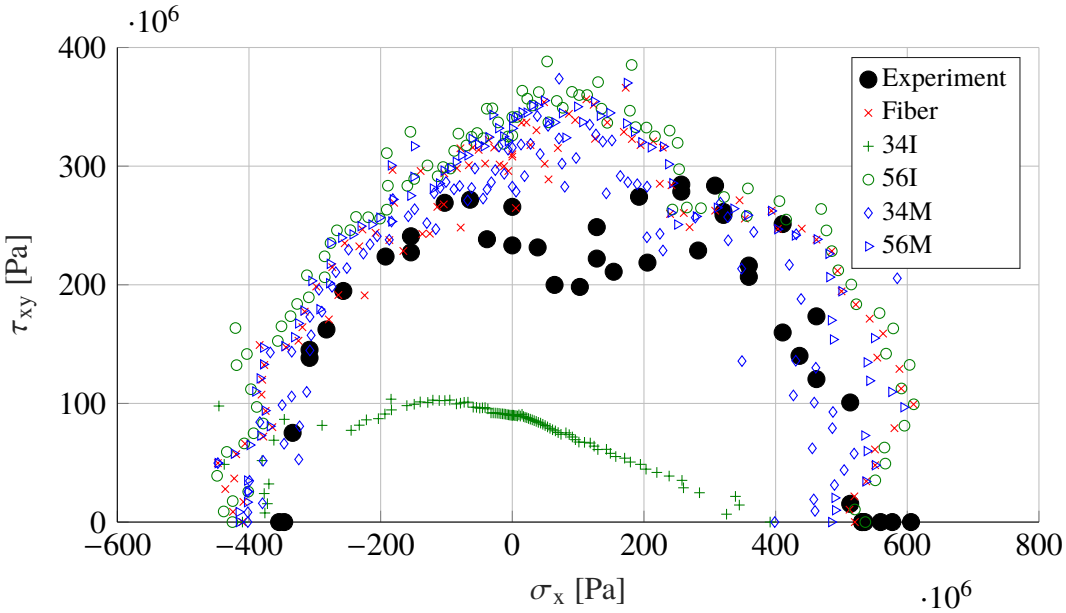

Figure 6.21. Individual failures for normal and shear loading in -30-degree ply from Abaqus

CHAPTER 7:
Composite Cylinder Testing

In order to further exercise the proposed failure criteria against actual test data in addition to the data provided in the World-Wide Failure Exercise, the proposed model was also utilized to predict stiffness properties and failure strength of filament-wound carbon fiber cylinders. Sets of cylinders of varying thickness and winding schedule were purchased from commercial winding vendors as well as wound by the author and tested using an experimental internal pressure device. The cylinders were also modeled in finite element software using the multiscale model and failure model in order to demonstrate both stiffness prediction as well as ultimate strength of the cylinders under internal pressure.

7.1 Cylinder Description

Filament-wound carbon fiber cylinders were manufactured by a commercial composite winding operation as well as by the author using a desktop filament winding machine. These cylinders were constructed from Torayca T700 fibers with a UF3325 thermoset pre-impregnated epoxy. The T700 fibers are arranged in a single "yarn" or "tow," which is a collection of hundreds or thousands of individual fibers. The cylinders were typically two layers of carbon fiber with an inside diameter and length of 76.2 mm (3 inches). The thickness was nominally 0.762 mm (0.030 inch), depending on the number of winding layers and the matrix material used. Some thicker specimen of 1.778 mm (0.070 inch) were also tested; they were constructed of four layers of two repeated patterns. The particulars of each cylinder tested is recorded in Table 7.1.

A variety of winding schedules were used in order to give a wide span of possible failure levels against which to test the effectiveness of the multiscale failure model in finite element software. Of the two layers in each cylinder, the first layer was primarily hoop windings, while the top layer was either 45 or 60 degrees. Additional cylinders of $[85]_2$ were constructed and tested, however their results are not included in other than a qualitative sense, since their construction and uniformity was suspect.

Table 7.1. Cylinder testing results

MFG	Lyr1 [deg]	Lyr2 [deg]	Lyr3 [deg]	Lyr4 [deg]	ID [m]	OD [m]	Len [m]	Thick [m]	Fail Load [N]	Fail Press [Pa]	Fail Stress [Pa]	Fail Strain [%]	Notes
AC	85	45	85	45	0.0762	0.079756	0.0762	0.001778	1.74E+05	5.21E+07	1.14E+09	0.0167	
AC	85	45	85	45	0.0762	0.079756	0.0762	0.001778	1.56E+05	4.69E+07	1.03E+09	0.0156	
AC	85	45	85	45	0.0762	0.079756	0.0762	0.001778	1.62E+05	4.84E+07	1.06E+09	0.0156	
								Mean	*1.64E+05*	*4.91E+07*		*0.01597*	
								StD	*8.88E+03*	*2.66E+06*		*0.00064*	
AC	85	45	–	–	0.0762	0.077978	0.0762	0.000889	9.18E+04	2.75E+07	1.19E+09	0.0156	
AC	85	45	–	–	0.0762	0.077978	0.0762	0.000889	9.85E+04	2.95E+07	1.28E+09	0.0167	
AC	85	45	–	–	0.0762	0.077978	0.07112	0.000889	7.92E+04	2.54E+07	1.10E+09	0.0163	short
AC	85	45	–	–	0.0762	0.077978	0.0762	0.000889	8.07E+04	2.42E+07	1.05E+09	0.0125	uncured
								Mean	*8.98E+04*	*2.75E+07*		*0.01619*	
								StD	*9.83E+03*	*2.05E+06*		*0.00055*	
AC	85	60	–	–	0.0762	0.077978	0.0762	0.000889	8.71E+04	2.61E+07	1.13E+09	0.0133	
AC	85	60	–	–	0.0762	0.077978	0.0762	0.000889	8.64E+04	2.59E+07	1.12E+09	0.0131	
AC	85	60	–	–	0.0762	0.077978	0.0762	0.000889	9.25E+04	2.77E+07	1.20E+09	0.0146	
AC	85	60	–	–	0.0762	0.077978	0.0762	0.000889	7.96E+04	2.39E+07	1.03E+09	0.0128	uncured
								Mean	*8.87E+04*	*2.66E+07*		*0.01367*	
								StD	*3.35E+03*	*1.00E+06*		*0.00083*	
JD	85	85	–	–	0.0762	0.077978	0.0762	0.000889	9.56E+04	2.87E+07	1.24E+09		
JD	85	85	–	–	0.0762	0.077978	0.0762	0.000889	1.14E+05	3.43E+07	1.49E+09	0.0139	
JD	85	85	–	–	0.0762	0.077978	0.0762	0.000889	1.04E+05	3.12E+07	1.35E+09	0.0145	
								Mean	*1.05E+05*	*3.14E+07*		*0.01420*	
								StD	*9.42E+03*	*2.82E+06*		*0.00042*	

7.2 Finite Element Model

Three finite element models of the cylinders were constructed using shell elements, stacked shell elements and continuum elements. The cylinder was modeled using quarter-symmetry and internal pressure. Symmetric boundary conditions and zero displacement on the equator ($\theta = 0$ and $z = 0$) were also employed. Figure 7.1 depicts the model used.

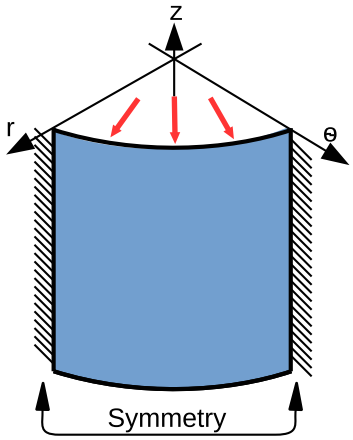

Figure 7.1. Cylinder quarter symmetry model

Filament winding offers an additional complication when modeling in finite elements. In actuality, the layup schedule is likely not uniform through the length of the specimen, but rather varies with both position and length. Figure 7.2 helps illustrate this peculiarity. Filament winding is normally a single filament wound from end-to-end on a mandrel. Once the filament has reached the far end of the mandrel, the winding head returns to the starting end while laying a filament of similar angle and opposing sign. The next round-trip lays filament next to those previously lain. This continues until the entire mandrel surface is completely covered with both orientations. Figure 7.2 shows that the cylinder, while typically stated as $[\pm\theta]_s$ or similar, is more complex where some areas have $+\theta$ nearest the mandrel and others have $-\theta$ nearest. While it is possible to wind cylinders with complete layers at stated angles, the process is time consuming, potentially error-ridden and of questionable utility.

Additionally, the location of the specimen in the winding pattern can be crucial to the correctness of the model. It may be desired that the equator or "transition knot" shown in Figure 7.2 lie in the middle of the sample, or be excluded from the sample completely. This

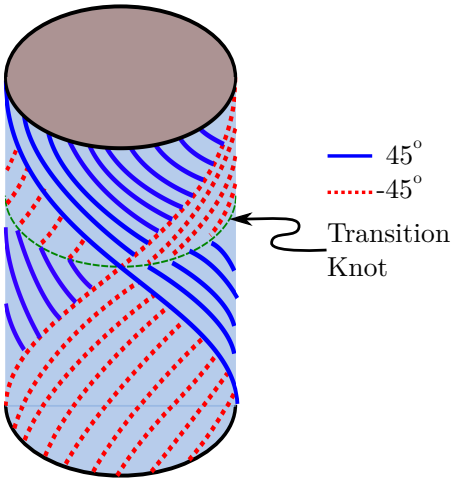

Figure 7.2. Illustration of bottommost ply for angled layers during hoop winding

may or may not be possible based on the winding angle and the diameter of the winding mandrel. For the hoop winding, however, it will always be helical in nature regardless of the width of the individual fiber or tow of fibers. The hoop windings for all the cylinders, therefore, are approximated by two steep-angle windings, one on top of the other, nominally $\pm 85^o$.

For simplicity and to avoid twisting effects in the finite element model, layers other than hoop winding angles were modeled as symmetric layers with the actual thickness of the layer being modeled. For instance, a ±45-degree layer of 0.381 mm (0.015 inch) thickness was modeled as $[+45, -45]_s$ with each layer as 9.5×10^{-2} mm (0.00375 inch) thick, while in reality it contains two non-symmetric layers of 0.191 mm (0.0075 inch) in thickness.

7.3 Specimen Instrumentation

In addition to the force gauge on the Instron/SATEC machine and the machine's measurement of compressive extension, a speckle pattern was painted on the side of each specimen for use with a digital image correlation (DIC) system. Some specimen were also instrumented with resistive strain gauges to compare with DIC measurements. The DIC system was used in place of the strain gauges on many tests since its results compared satisfactorily with the resistive strain gauges.

The DIC system calculates the strain state of the visible portion of the case exterior by tracking the motion of the speckle pattern mentioned earlier during the loading portion of the experiment. Post-processing can also be accomplished in order to transform the data calculated in rectangular coordinates to cylindrical coordinates such that hoop stresses can be directly extracted.

The DIC system was also chosen as the primary measure of strain for the cylinder tests since the placement of the resistive strain gauges on the exterior of the sample proved to be a significant factor in their measurement. Placement of the gauges on differing directional weaves or bridging across two patterns produced significantly different results. To remove the gauge placement dependency, the whole-field strain as measured by DIC was used.

7.4 Cylinder Testing

Practical destructive testing of the carbon fiber wrapped cylinders was accomplished with an Instron/SATEC-operated pipe-expander. The design for the apparatus is analyzed by Ponshock [30]. Ponshock constructed a finite element model of the device in Ansys to determine uniformity of stress delivered to the inside of the cylinders and to ensure that the device doesn't deform exceptionally while applying the pressure to the inside of the test article.

This expansion device was used in a SATEC compression testing machine to provide a relatively uniform internal pressure on the walls of the test cylinders. The test apparatus uses opposing conical rams driven towards one another, providing outward force on a segmented cylinder of eight equal wedges against which the conical rams bear. The cylinder under test is placed around the assembled wedges. A depiction of the device is shown in Figure 7.3.

This test apparatus provides internal pressure in the test specimen, applied by the cylindrical faces of the segmented wedges. The uniformity is aided by the insertion of two clamshell shims between the wedge faces and the internal face of the specimen

The tests were conducted using a custom Instron test method program where the samples are brought slowly to a machine force of 8 kN, held for 15 seconds, increased at the same rate to 15 kN and again held for 15 seconds, after which the machine compresses at an increased rate (2 mm/min) until sample failure. The need for these load-hold cycles are twofold. First,

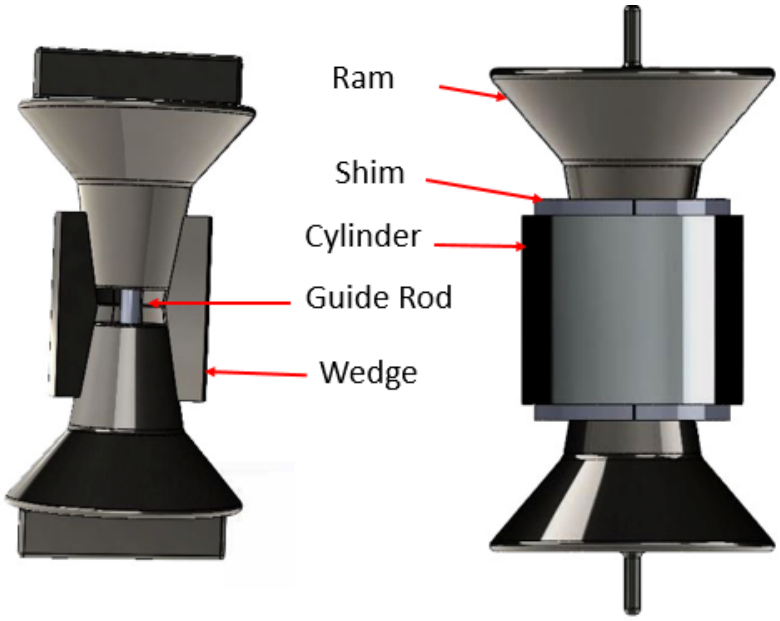

Figure 7.3. Cylinder expansion device for testing burst pressure. Source [30].

the first load cycle allows a slow squeeze-out of excessive lubricant (molybdenum high-pressure grease) as well as a first data-matching plateau for the digital image correlation software and the strain gage data acquisition software, both of which are currently unable to collect force data from the Instron system. The second loading pause provides a second data-match plateau. Both of these plateau are early enough in the loading of the specimen so that they are comfortably within the elastic range of the specimen. [4]

To convert Instron machine force to internal pressure, the free-body diagram of the cylinder apparatus is constructed (Figures 7.4) to show that the force borne by the inside of the cylinder from the machine is:

$$F_{wc} = F_m \frac{\cos\theta - \mu \sin\theta}{\sin\theta + \mu \cos\theta} \tag{7.1}$$

where F_m is the force applied by the machine, μ is the coefficient of sliding friction, and θ is the cone-and-wedge angle shown in Figure 7.4. Converting this to internal pressure by

[4]For a more detailed description of the data-matching plateau, see Section A.1.

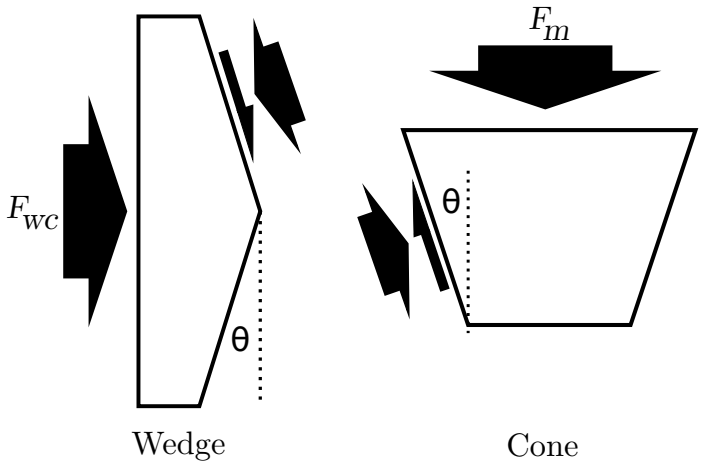

Figure 7.4. Free body diagram of wedge and ram device. Adapted from [30].

dividing by the inner surface area of the cylinder:

$$P_I = \frac{2F_m}{\pi dl}\frac{\cos\theta - \mu\sin\theta}{\sin\theta + \mu\cos\theta} \tag{7.2}$$

where d and l are diameter and length of the cylindrical specimen.

The coefficient of friction, μ, used in these formulæ was first obtained by experiments conducted in Ponshock [30] and reestablished in this research.

The figures that follow are plotted with internal pressure on their y axis. This choice is deliberate since a conversion from machine force to internal pressure is a derived quantity, and using it prevents the use of a second calculation to display hoop stress, which could add unnecessary error. Also, the finite element model of the cylinders used internal pressure as the load, thus it was preferable to use internal pressure as the common quantity.

7.5 Test Results

Cylinder testing was conducted using the mechanical expander on mild steel and carbon fiber filament-wound cylinders. Test data was very consistent, and in some cases provides areas for additional research. The results applicable to the failure model validation are described here, and areas for additional exploration are included in Chapter 9.

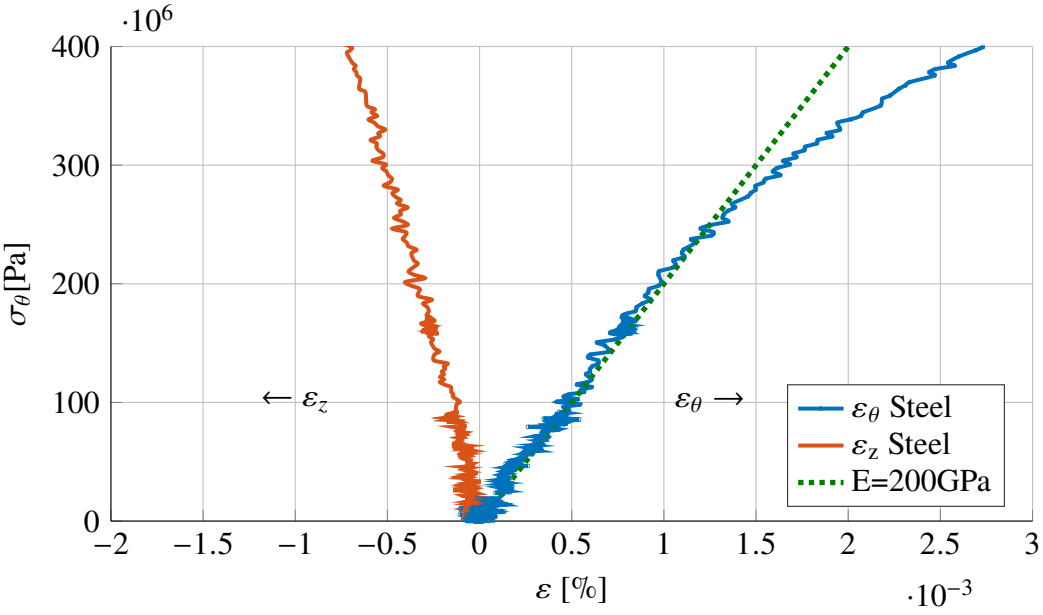

Figure 7.5. Steel cylinder experimental results

7.5.1 Steel Cylinders

The testing of steel cylinders was intended first as a re-verification of the coefficient of friction of the experimental setup estimated by Ponshock [30] as well as a direct comparison of the strengths of similarly sized and similarly tested steel and filament-wound carbon composite cylinders. The stress versus strain plot as captured from the DIC is plotted in Figure 7.5. This data allows the calculation of the coefficient of friction using the known modulus of mild steel, as well as a second validation of the Poisson ratio by comparison of $\varepsilon_z/\varepsilon_\theta$.

The reverification of the coefficient of friction was accomplished by averaging the strain values measured during the steel cylinder test using Equation 7.2 and the thin-walled cylinder approximation ($\sigma_\theta = {}^{Pr}/_{t}$) which combine to form the relationship

$$\mu = -\frac{\varepsilon_\theta \pi l t E \sin(\theta) - 2F_m \cos(\theta)}{\varepsilon_\theta \pi l t E \cos(\theta) + 2F_m \sin(\theta)} \tag{7.3}$$

where E is the Young's modulus of mild steel (200×10^9 Pa), F_m is the machine force, θ is the angle of the wedge/cone pair, and ε_θ is the experimentally measured hoop strain.

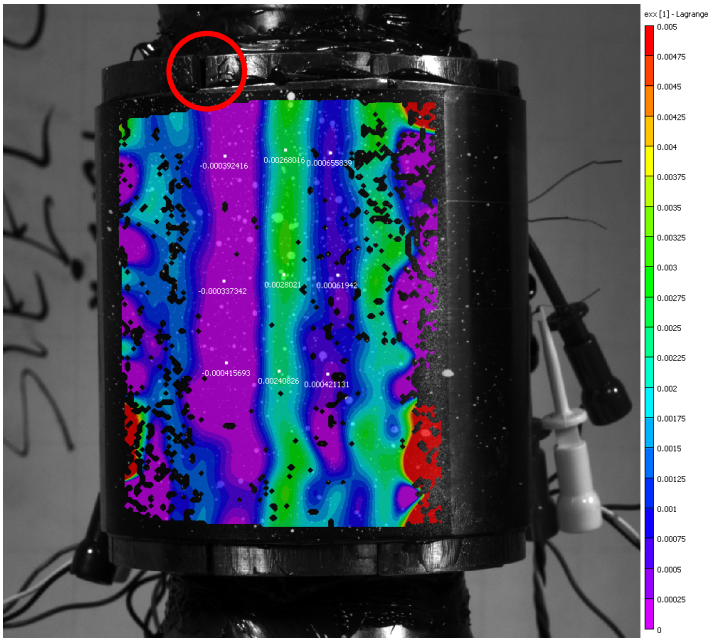

Figure 7.6. Steel cylinder strain fringe (ε_x) at yield

The steel cylinder test indicated that the coefficient of friction for these experiments was estimated at $\mu = 0.178$, used for the remainder of the calculations.

The steel cylinder was subjected to internal pressure through its elastic region into plastic response. Plastic response began at expected yield stress of 250 MPa. The steel cylinder did not fail completely, because the expander device reached maximum travel prior to the cylinder reaching ultimate failure. The DIC fringe plot of strain taken at yield is shown in Figure 7.6. This plot shows a variation in hoop strain of 3,500 μm/m between areas immediately adjacent. This is likely a consequence of the clamshell shims acting as stress concentrators rather than their intended use as distributors. Additional experiments should be conducted to determine whether these shims are beneficial or detrimental to the testing.

This data also allows an estimate for the longitudinal stress applied to the sample as friction on its inner surface. Lubrication was also applied to the sample between the clamshell shims and the inner diameter of the sample to reduce this friction. The peak calculated axial stress before the sample began to respond plastically was 37 MPa, which corresponds to a maximum longitudinal tensile stress of 14% of the applied hoop stress.

7.5.2 Simple Composite Winding

The first subset of cylinders were all wound with a hoop orientation as the innermost layer followed by an angular layer. Additional hoop or angular layers in some cases were then added or repeated. The cylinders described here were three 1.778 mm (0.07 in) thick cylinder with the winding schedule $[85, \pm 45]_2$, and three each of 0.889 mm (0.03 [in) thick $[85, \pm 45]_1$ and $[85, \pm 60]_1$.

The $[85, \pm 45]_2$ Cylinder

The cylinders tested provided repeatable results where the cylinder failure pressure averaged 59.4 MPa with a standard deviation of 0.321 MPa. The three cylinders all failed similarly with a parting of the internal fibers (hoop layer) and an opening of the cylinder following this failure. The pressure-strain plots from one of these experiments is shown in Figure 7.7. Also plotted are the results from the three finite element simulations. The average internal pressure at failure for these models was 55.0 MPa with a standard deviation of 1.7 MPa, which provides a 3% under-prediction on average (a 10% under-prediction in the worst case, and 1% under-prediction in the best case).

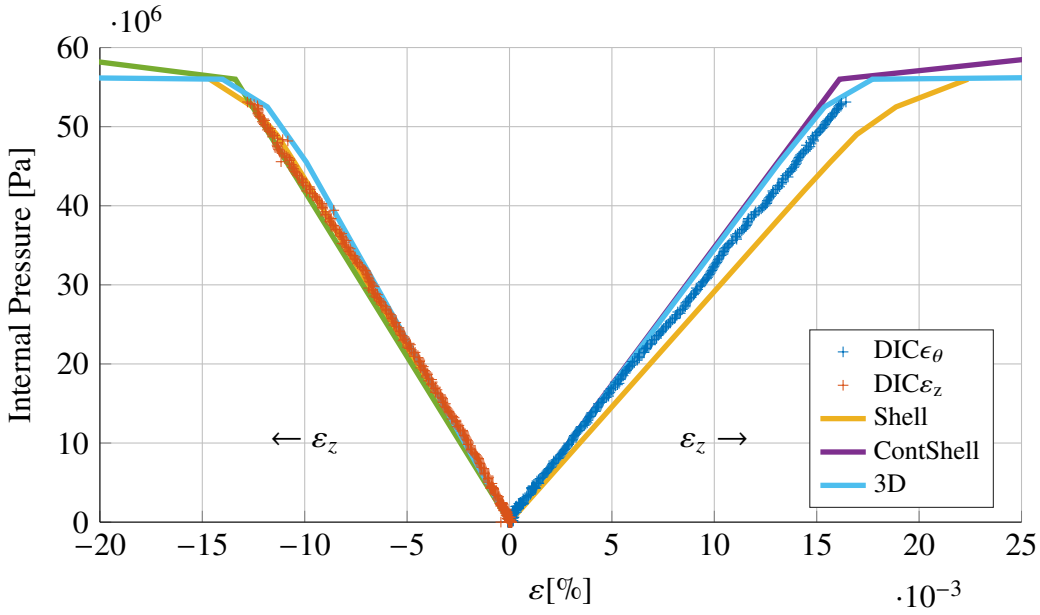

Figure 7.7. Experimental measurement and finite element model results for $[\pm 85, \pm 45]_2$ cylinder

The $[85, \pm 45]_1$ Cylinder

These cylinders were very consistent from cylinder to cylinder where the failure pressure averaged 30.2 MPa with a standard deviation of 1.8 MPa. The three cylinders all failed similarly with a parting of the internal fibers. The pressure-strain plots from one of these experiments is shown in Figure 7.8. Also plotted is the results from the three finite element simulations. The average internal pressure at failure for these models was 28.7 MPa with a standard deviation of 1.15 MPa. The finite element prediction for failure pressure is a 5% under-prediction on average (a 16% under-prediction in the worst case, and 2% under-prediction in the best case).

Figure 7.9 plots hoop and axial strain for the $[85, \pm 45]_1$ cylinder immediately before failure. This fringe shows a relatively uniform axial strain; however, the same artifact seen in the steel fringe is manifest in the wound cylinder, where the majority of the cylinder exhibits a uniform strain, but the fringe contains an area where adjacent areas exhibit a difference in strain of 18,000μ.

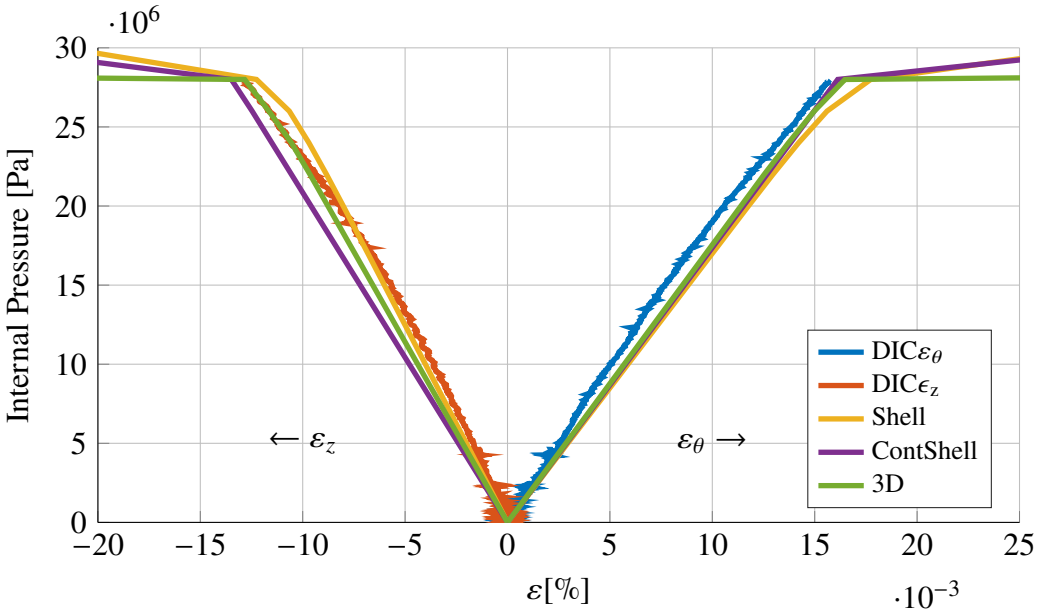

Figure 7.8. Experimental measurement and finite element model results for $[\pm 85, \pm 45]_1$ cylinder

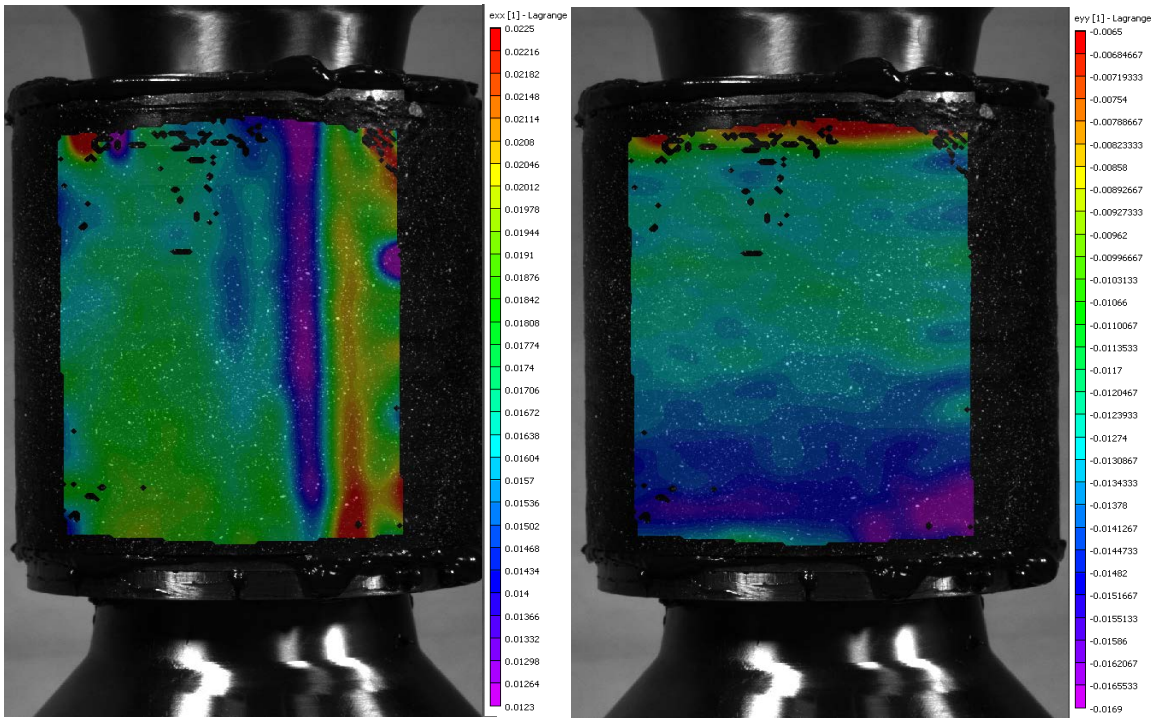

Figure 7.9. Hoop (left) and axial (right) strain fringe at failure for $[85, \pm 45]_1$ cylinder

The $[85, \pm 60]_1$ Cylinder

The cylinders tested provided repeatable results where the cylinder failure pressure averaged 32.1 MPa with a standard deviation of 1.22 MPa. The three cylinders all failed similarly with a parting of the internal fibers and an opening of the cylinder following this failure. The pressure-strain plots from one of these experiments is shown in Figure 7.10. Also plotted is the results from the three finite element simulations. The average internal pressure at failure for these models was 28.7 MPa with a standard deviation of 1.16 MPa. The finite element prediction is a 8% over-prediction on average (a 15% over-prediction in the worst case, and 1% over-prediction in the best case).

For this sample, the hoop pressure-strain curve is nearly linear to failure; however, the longitudinal pressure-strain curve is distinctly nonlinear. This feature is repeated in all $[85, \pm 60]_1$ experiments, but is not seen in the $[85, \pm 45]_2$ and only slightly present in $[85, \pm 45]_1$ plots.

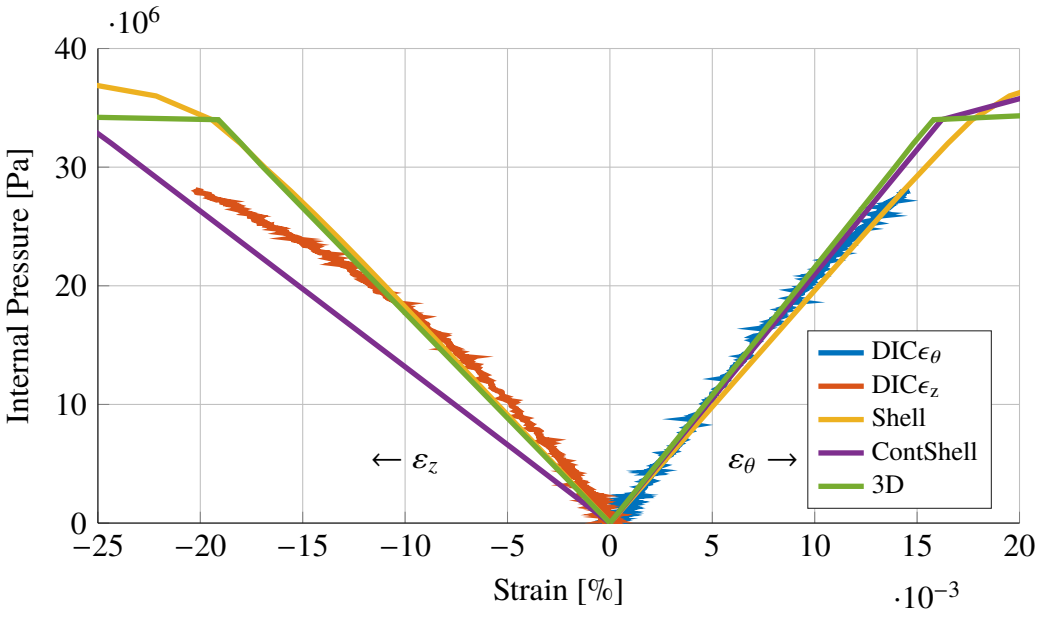

Figure 7.10. Experimental measurement and finite element model results for $[\pm 85, \pm 60]_1$ cylinder

7.6 Additional Testing Observations

As expected in a qualitative sense, cylinders with windings that are closer to hoop direction demonstrate larger hoop moduli. For instance, an $[85]_2$ cylinder tested was stiffer in the hoop direction than the $[85, \pm 60]_1$ cylinder, which was approximately as stiff as the $[85, \pm 45]_1$ cylinder. This was seen in both the cylinder testing as well as finite element simulations. A plot of this hoop modulus as a function of outermost winding angle as calculated by finite element simulation is shown in Figure 7.11 (a). These simulations predict that shallow (axial) outer windings contribute a negligible amount to the hoop stiffness. This behavior is predicted through outer windings of 60 degrees. For angles greater than 60 degrees, the outer windings begin to contribute more significantly. This increased stiffness contribution is observed in the cylinder testing and repeated in finite element models.

An unexpected observation from the cylinder testing was the effect that the outer winding angles had on the axial strain of the cylinder specimen. As expected, steep windings as those in the $[85]_2$ cylinders, showed very small axial strain for corresponding hoop strain. For outer layers of 60 degrees, a marked increase in axial strain versus hoop strain was noted over that of the cylinders with purely hoop winding. It was initially assumed that as

the outer windings became shallower, the ratio of axial strain to hoop strain would either increase (the Poisson ratio would become greater) or become level; however, the cylinders with 45-degree external winding showed a decrease over that of the 60-degree cylinder in both experiment and simulation. Additional finite element simulations of different angles were then conducted to explore this phenomenon. The plot of these results is shown in Figure 7.11 (b). There appears to be a "belly" in this data such that for external winding angles between 30 and 70 degrees, there is a marked increase in axial response as a function of hoop stress over that of purely hoop windings or hoop windings covered with shallow angles. This graph also postulates that there is a maximum axial response for a given hoop stress at approximately 60 degrees.

This response in the 60-degree cylinder may be due to the fiber phase acting as a strength member and aligning more with the loading direction, and attempting to rotate toward it. This rotation may be responsible for the additional axial shrinking. For cylinders with shallower windings (closer to zero), the response may be less pronounced since the fiber-matrix interface and the matrix itself is the predominant load carrying component. The matrix, since it is assumed to be isotropic, will not rotate toward the load and therefore less likely to show this response as negative axial strain. Conversely, cylinders with steeper angles (closer to hoop) have a shorter distance through which to rotate in order to be in alignment with the load. The nonlinear axial strain response shown in Figure 7.10 may be further confirmation that this rotation is at play. The matrix material in the 60-degree layer may be allowing this nonlinear response while the hoop strain in the same region remains approximately linear.

As further confirmation of this unexpected response, Figure 7.11 (c) plots the Poisson ratio ($\varepsilon_z/\varepsilon_\theta$) of the cylinders as predicted by finite element simulation. The unusual response of the $[85, \pm 60]$ cylinder is further highlighted as well as an increased response of the $[85, \pm 45]_2$ cylinder over that of the $[85, \pm 45]_1$.

7.7 Conclusion

In addition to demonstrating model validity and effectiveness, cylinder testing led to other experimental observations such as observations concerning the utility of the clamshell shims, the superior performance of DIC for strain measurement over foil strain gauges,

and precautions required during testing to obtain satisfactory results. These observations will lead to improvements in testing procedures, data collection capabilites, and modeling techniques. Furthermore, unexpected trends seen in the carbon cylinder data and the finite element simulations with regard to the performance of the cylinder as a function of its outermost winding will provide valuable insight into methods used to design composite layups for optimal structures.

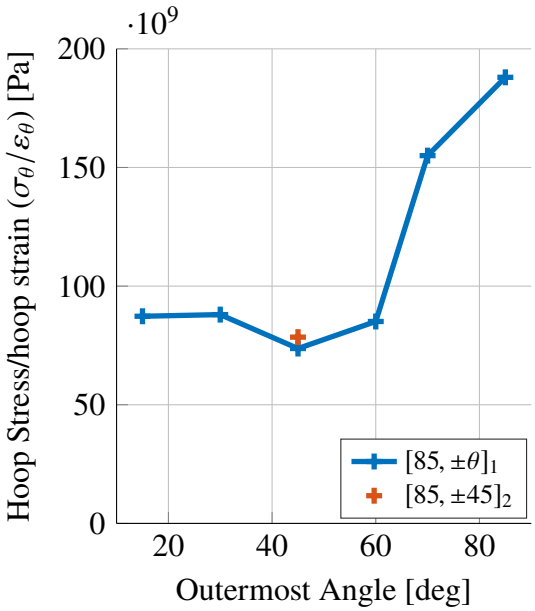

(a) Hoop stress/hoop strain (hoop modulus) versus outermost angle

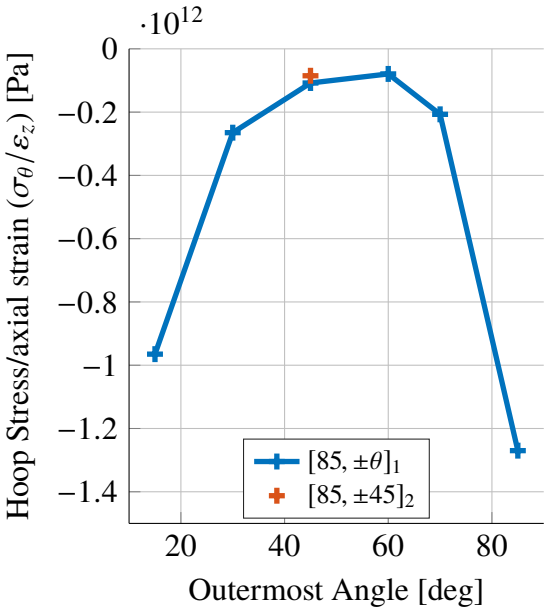

(b) Hoop stress/axial strain ($\approx {}^{E_y}/_{\nu_{yx}}$) versus outermost angle

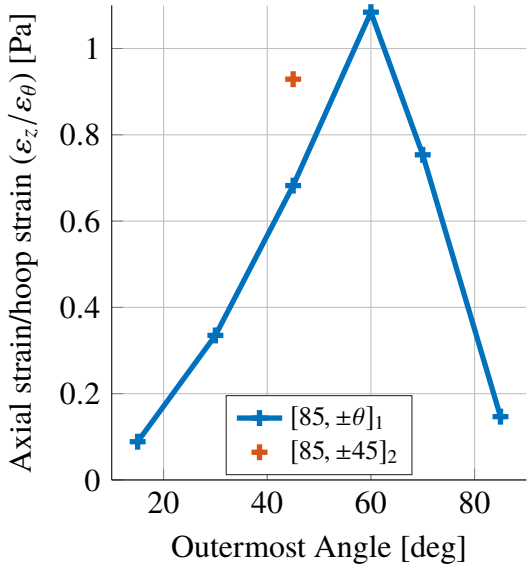

(c) Axial strain/hoop strain (Poisson ratio) versus outermost angle

Figure 7.11. Finite element model properties

CHAPTER 8:
Parametric Studies

Parametric studies are presented here to explore the stability and utility of the multiscale method and failure criteria. The input parameters of volume fraction, Young's modulus of the constituents and small rotations of composites are addressed. The parametric study helps to identify whether either the multiscale method or the failure criteria or both are stable for changing inputs and produce reasonable response.

8.1 Volume Fraction Effects on Failure Envelope

The first parametric exploration is the effect of changing the fiber volume fraction of the composite. As with the envelopes plotted in Chapter 6, a "radar search" was performed in the applicable stress space for each of the uniaxial composites. For each of the uniaxial loading scenarios, the fiber volume fraction was decreased from the given 60% to 50% and increased to 70% (a 17% change) and a new failure envelope was generated based on the new fiber volume fraction.

The first study, E-Glass LY under $\sigma_y - \tau_{xy}$ is plotted in Figure 8.1. It shows no appreciable change in the interface failure region of the envelope; however, the envelope shows significant change in the matrix failure portion (transverse compression). The 17% change in volume fraction shows a ±1% change in shear failure value, a ±5% change in transverse tensile failure value, and approximately ±7% change in transverse compression failure value. Using Equation 2.24, an increase in fiber volume fraction increases the shear and transverse modulus of the composite strand by the contribution of a larger fiber subcell. This reduces composite strain and therefore subcell strain, allowing an increase in applied stress prior to reaching matrix failure strain or interface shear failure stress.

The next study, T300 under $\sigma_x - \tau_{xy}$ is plotted in Figure 8.2. The major change in this envelope is an increase and decrease in the fiber failure portion of the envelope for increased and decreased fiber volume fraction (respectively). A ±17% change in volume fraction produces a ±17% change in both tensile and compressive longitudinal failure values and a ±2% change in the shear failure value. This change is due to the increased (or decreased)

Table 8.1. Parametric study summary

		v_f		E_f		E_m		Angle	
		0.5	0.7	-25%	+25%	-25%	+25%	-5^o	$+5^o$
$\sigma_y - \tau_{xy}$	$\sigma_{y,T}$	-5.4%	3.3%	–	–	–	–	–	–
	$\sigma_{y,C}$	-9.1%	6.6%	–	–	-21.5%	26.4%	–	–
	τ_{xy}	-1.7%	1.7%	–	–	–	–	-3.3%	8.3%
$\sigma_x - \tau_{xy}$	$\sigma_{x,T}$	-16.4%	15.8%	-25.0%	24.3%	–	24.3%	-28.1%	-28.1%
	$\sigma_{x,C}$	-16.3%	16.2%	-24.8%	24.7%	–	24.7%	-27.6%	-27.6%
	τ_{xy}	-2.5%	1.2%	–	–	–	–	–	–
$\sigma_x - \sigma_y$	$\sigma_{x,T}$	-18.1%	12.3%	-18.3%	34.6%	–	–	–	–
	$\sigma_{x,C}$	–	–	–	–	–	–	–	–
	$\sigma_{y,T}$	-18.1%	12.0%	-18.4%	34.2%	–	–	-26.5%	–
	$\sigma_{y,C}$	-9.2%	7.0%	–	–	-24.6%	25.4%	–	–

portion of the fiber, the major longitudinal strength member of the composite. An increased fiber volume fraction allows the application of additional stress prior to the fiber subcell reaching failure strain. For the interface portion of the failure envelope, as in the $\sigma_y - \tau_{xy}$ case, the fiber volume fraction shows a small effect. An increased interface failure value can be attributed to an increased composite shear modulus and decreased composite strain.

The last study, E-Glass MY under $\sigma_x - \sigma_y$ is plotted in Figure 8.2. The envelope plotted in this scenario shows a response as expected from the previous two scenarios. The interface failure in transverse tension is relatively unaffected by the fiber volume fraction. The fiber failure lines in longitudinal tension and compression show increased and decreased failure stresses with increased and decreased fiber volume fraction. Lastly, in transverse compression, the matrix failure criterion shows similar response to that of the $\sigma_y - \tau_{xy}$ scenario.

8.2 Constituent Stiffness Effects on Failure Envelope

Changes in the stiffnesses of the constituents was also varied to explore the impact on the failure envelopes of a uniaxial composite. The stiffnesses were varied by ±25% and plotted with the as-modeled failure envelope, plotted with the data provided from the WWFE.

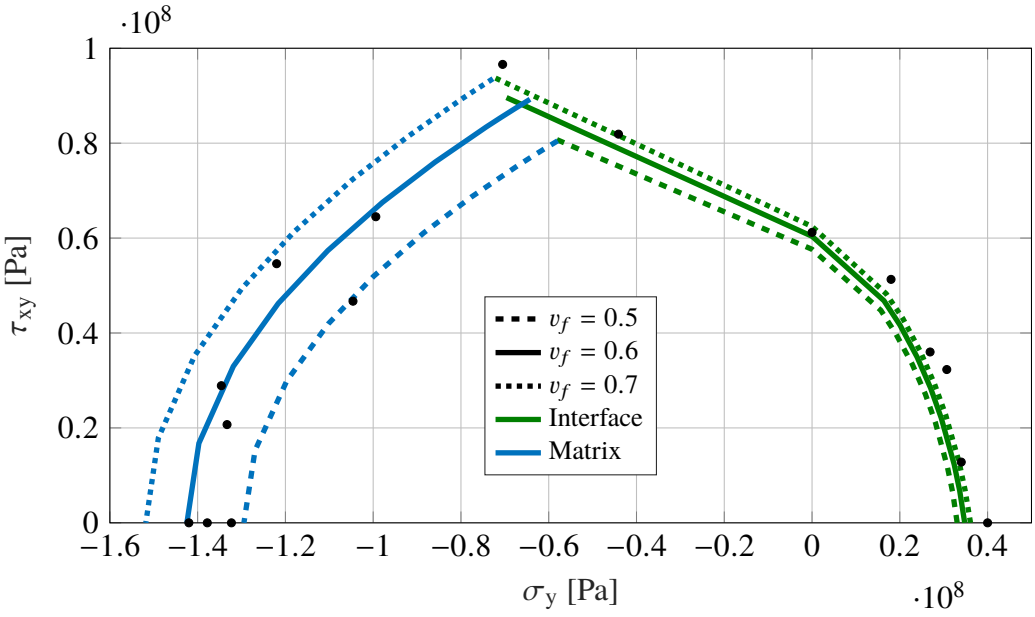

Figure 8.1. Parametric study for E-Glass LY ($\sigma_y - \tau_{xy}$) change volume fraction

8.2.1 Change of Fiber Stiffness

The fiber modulus of the E-Glass composite fiber was altered by reducing or increasing the longitudinal and transverse moduli by 25%. Since the E-Glass fibers act isotropically, the longitudinal and transverse moduli were the same. The shear modulus of the fiber was also altered using the modified longitudinal modulus:

$$G^f_{xy} = {}^{E^f}/_{2(1+\nu_{xy})}$$

The T300 fiber is not isotropic, so the fiber's modulus was altered by changing the longitudinal, transverse and shear modulus by ±25%.

The first study, E-Glass LY under $\sigma_y - \tau_{xy}$ is not shown since it is unchanged from the base case. Altering the fiber modulus (and the shear modulus) does not significantly impact the failure envelope of this material under this stress. This can also be seen later in Figure 8.5 since the failure envelope in the σ_y direction does not appreciably change with changing E^f.

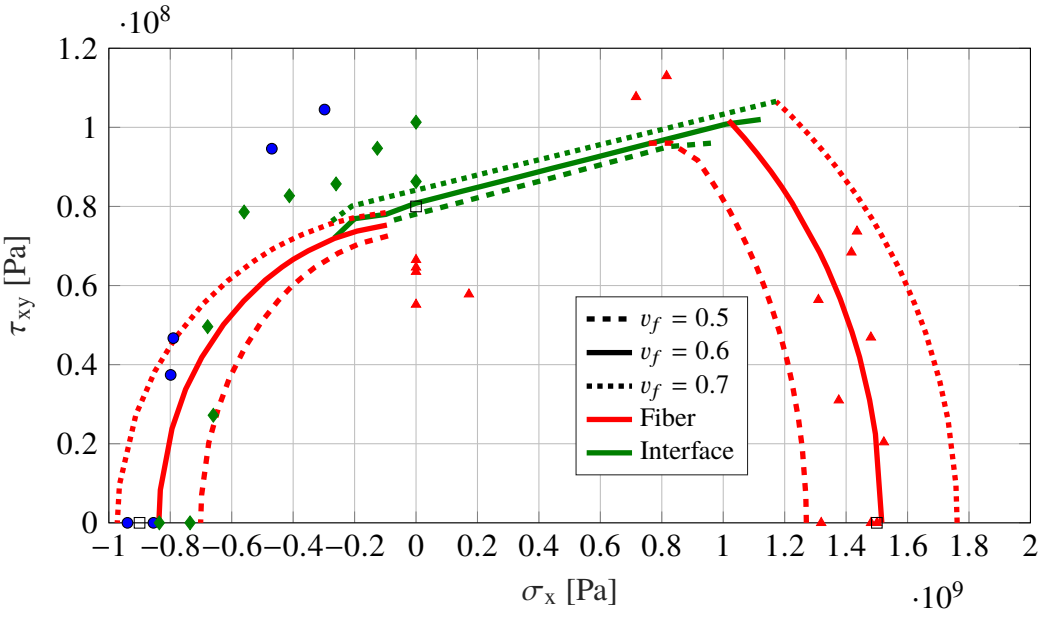

Figure 8.2. Parametric study for T300 ($\sigma_x - \tau_{xy}$) change volume fraction

The second study, T300 under $\sigma_x - \tau_{xy}$ is shown in Figure 8.4. The longitudinal tension and compression values follow the change in fiber stiffness, as expected. The change in longitudinal failure values is commensurate with the change in fiber stiffness (±25%). Again, increased stiffness of the fiber subcell contributes additional stiffness to the composite, allowing larger stresses to be applied prior to reaching failure strain. The interface failure curve appears not to change in this scenario, however the curves show a discontinuity with the -25% reduction in fiber modulus.

Figure 8.4 contains a feature that indicates that the failure model may require refinement. All the parametric cases were conducted using the failure values for the "real" composites since the failure values for the altered composites are unknown. The envelope lines delineating the fiber failures and matrix failures for other than the real composites are likely more accurate than those drawn for interface failure since the interface failure criteria relies on the composite level shear stress failure value for the desired composite, not known in this instance. In further improvements to the theory, the τ_u in Equation 3.8 should be altered with changes in matrix or fiber stiffness as well as changes in volume fraction. As the fiber subcell approaches the properties of the matrix, then τ_u should approach τ_u^m, and alternatively as the matrix approaches the properties of the fiber, then τ_u should approach

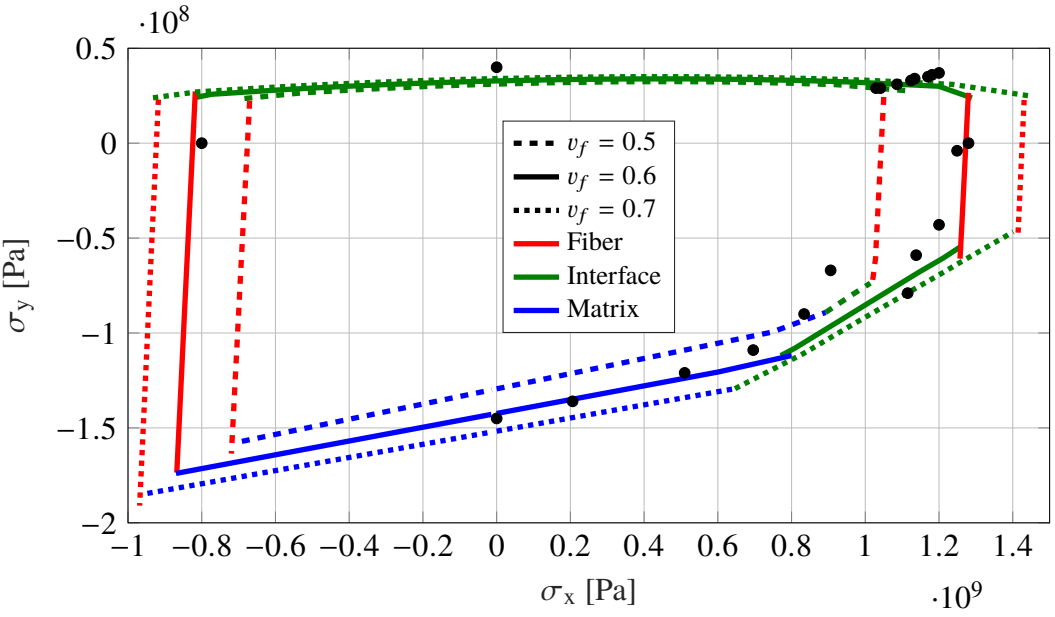

Figure 8.3. Parametric study for E-Glass MY ($\sigma_x - \sigma_y$) change volume fraction

τ_u^f. Alternatively, interface failure may be able to be posed as a strain-based criteria, where the failure quantity could be based on the shear strain difference between the subcells.

The last study, shown in Figure 8.5, illustrates the lack of change in transverse failure values described above for the $\sigma_y - \tau_{xy}$ study. It also reinforces that which is shown in Figure 8.4, namely an increase in longitudinal failure stress scales with the increase in fiber modulus.

8.2.2 Change of Matrix Stiffness

For the final constituent property exploration, the stiffness of the matrix material was altered by ±25%. The first study for $\sigma_y - \tau_{xy}$, shown in Figure 8.6, indicates that a change in matrix stiffness only alters the compression quadrant. The specific change is an increase in matrix failure, that scales with the change in matrix stiffness.

The next study for $\sigma_x - \tau_{xy}$, shown in Figure 8.7 shows a very small change in interface failure, as with most scenarios. The major change is the increase in failure stress for an increase in matrix stiffness, which scale together. Interestingly, for a decrease in matrix stiffness, however, there is no appreciable change in failure stress. This is likely due to the significant difference in stiffness between fiber and matrix in this case. This case is for a

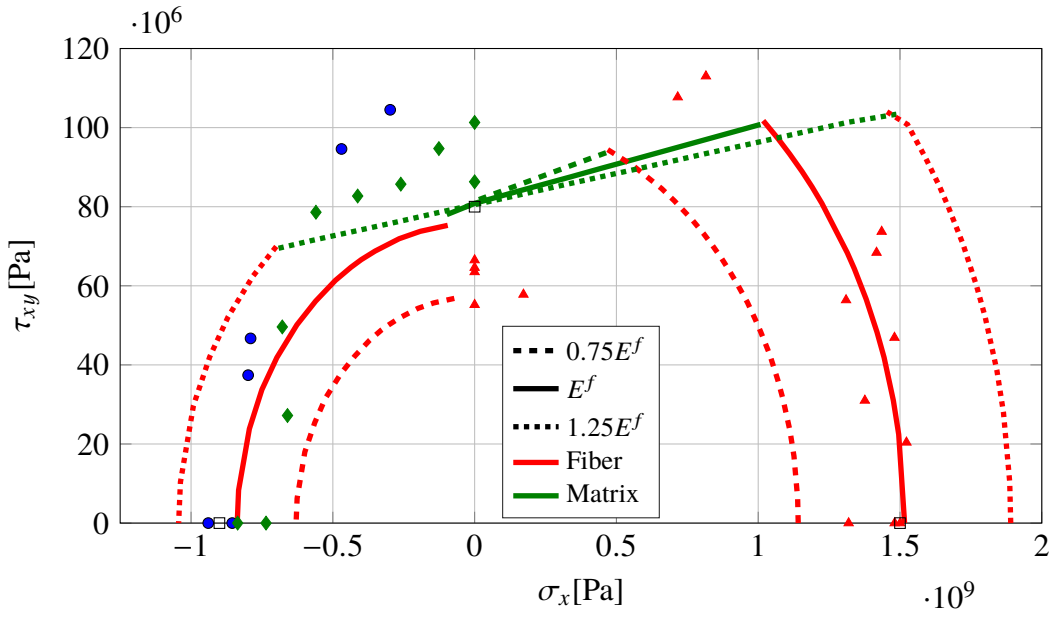

Figure 8.4. Parametric study for T300 ($\sigma_x - \tau_{xy}$) change fiber stiffness

carbon-fiber T300 composite, whose matrix material is 1% of the stiffness of the fiber. A decrease in matrix modulus is insignificant in comparison to the modulus of the fiber, and therefore a change in this material property contributes or removes an insignificant amount of composite stiffness, altering the failure envelope by a small amount.

The last study for $\sigma_x - \sigma_y$, shown in Figure 8.8 shows a change in matrix failure in transverse compression and a change in interface failure while under transverse compression and longitudinal tension. The matrix failure value increases and scales with increasing matrix stiffness. The interface failure line, however, shows decreased interface failure stress with increased matrix stiffness. This is due to the σ_x^{34} term in Equation 3.8. Its magnitude is less (although still positive) when the matrix stiffness used is greater than the true value (closer to the stiffness of the fiber). This decrease in subcell stress decrements a smaller amount from the numerator, allowing it to reach τ_u sooner.

8.3 Small Angle Effects on Failure Envelope

In addition to varying the material properties of the matrix, an exploration which varied the angles of the uniaxial composites through small angles was conducted. This was done to determine if the failure criteria exhibited any unexpected behavior when small

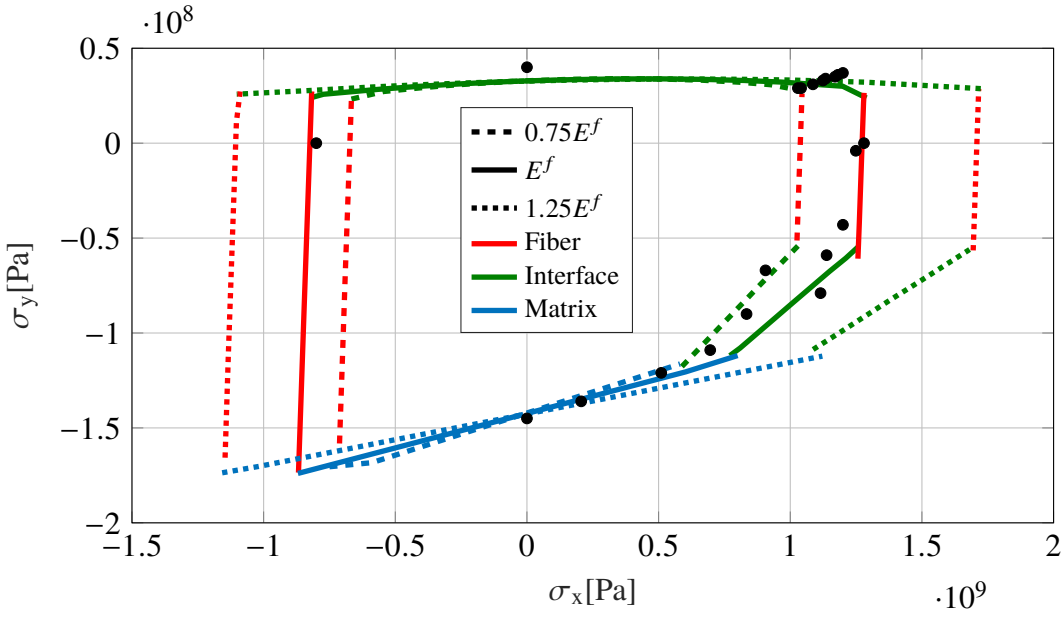

Figure 8.5. Parametric study for E-Glass MY ($\sigma_x - \sigma_y$) change fiber stiffness

perturbations were included in the model. Additionally, this exploration was done to see whether the experimental testing was sensitive to sample fiber angle, and if so, attempt to quantify the sensitivity.

The first study was for $\sigma_y - \tau_{xy}$ and is shown in Figure 8.9. This exploration showed expected results, that failure occurred at lower τ_{xy} for negative fiber angle and at greater τ_{xy} for positive angle. The slope of the interface failure line and its τ_{xy} intercept was the major difference between the angle perturbations; other portions of the envelope remained relatively unchanged.

The second study for small angle perturbations in $\sigma_x - \tau_{xy}$ is plotted in Figure 8.10. This exploration had interesting results in that small angles ($\pm 2.5^o - \pm 5^o$) indicated a large impact on the failure envelope. Some of the WWFE scatter could be explained by these small rotations ($\pm 2.5^o$), assuming that small manufacturing defects on the order of these angles were allowed. Larger rotations exceeding 5 degrees are less likely, since they are more easily observed during manufacture. If the FE simulation is correct, experimental data also is not represented by rotations as large as 5 degrees.

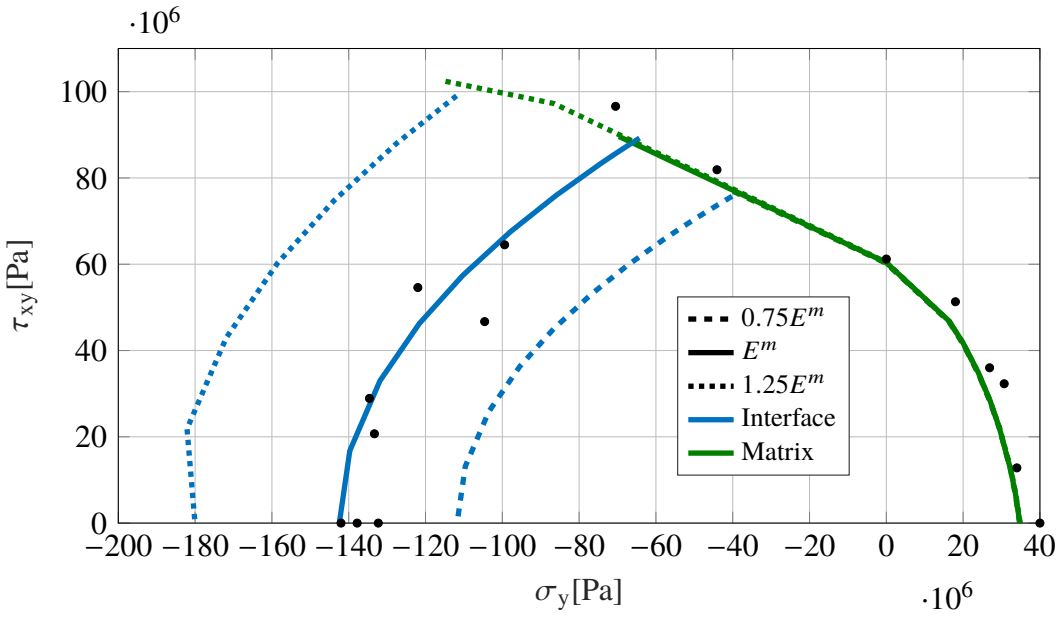

Figure 8.6. Parametric study for E-Glass LY (σ_y–τ_{xy}) change matrix stiffness

An explanation of the envelope's response to these rotations may be seen in Figure 8.11, where for positive rotations and positive shear, the fiber is in closer alignment with the resultant force. The reverse is true for negative rotations. Negative rotations present the fiber-matrix transverse interface toward the resultant force; therefore, a weaker interface causes an earlier failure.

This result will likely require experiments to verify, since extreme changes were caused by small angles. In addition to experiments, a laminate model could also be constructed that approximates a uniaxial composite with varied plies with small off-axis fiber angles. This total "uniaxial laminate" then could be rotated through these small angles to observe the impact on the envelope.

The last angle study was for $\sigma_x - \sigma_y$ rotated through -10,-5,+5 and $+10^o$ The plot in Figure 8.12 shows that the results in this case are symmetrical; the sign of the rotation does not change the envelope shape. For small angles, there appears to be no appreciable change in the longitudinal strength of the composite, but for larger angles of 10 degrees, there is considerable reduction in longitudinal strength since interface failure and matrix failure become the dominant modes.

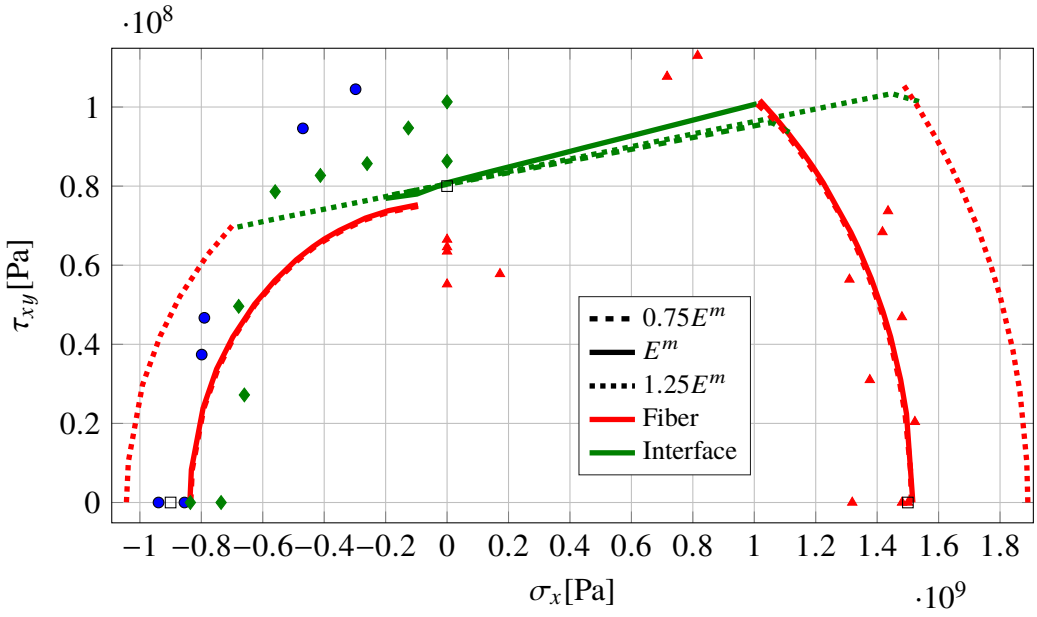

Figure 8.7. Parametric study for T300 ($\sigma_x - \tau_{xy}$) change matrix stiffness

8.4 Conclusions

These parametric studies provide valuable insight into the operation of the composite failure model. They provide a check to ensure that the model does not produce spurious results under reasonable perturbations, while at the same time provide estimates as to how a composite would perform if the constituents were altered. In the case of the altered E^f for $\sigma_x - \tau_{xy}$, a shortfall of using a composite-level failure stress in the failure model formulation is demonstrated. A better formulation and an object for further research is altering the interface failure criteria such that, like the fiber failure criteria and the matrix failure criteria, it utilizes constituent properties exclusively. The remainder of the parametric studies provide reasonable or explainable results, but results that should be confirmed with modeling and experimentation.

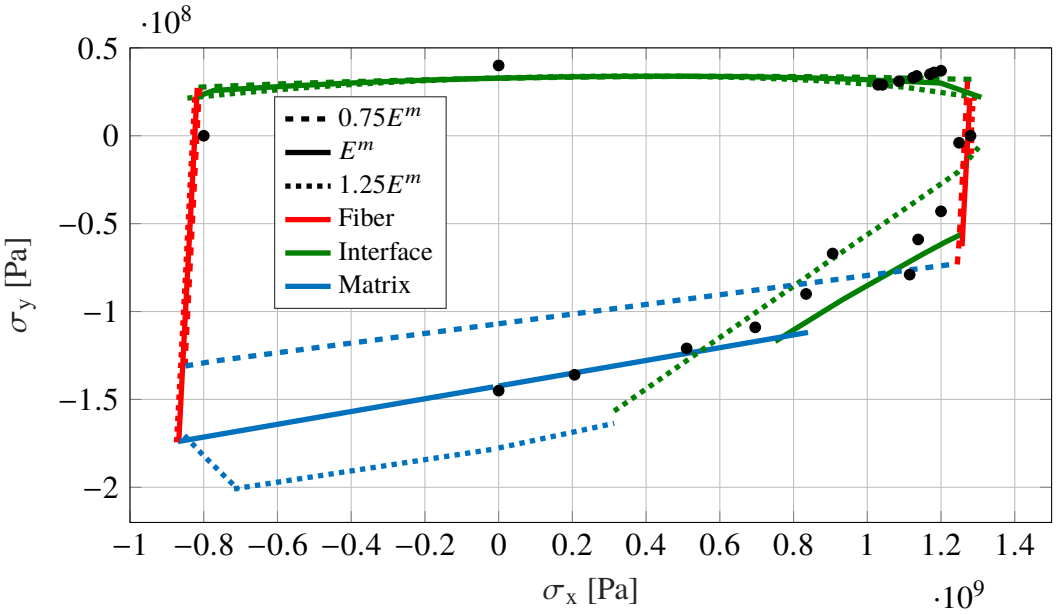

Figure 8.8. Parametric study for E-Glass MY ($\sigma_x - \sigma_y$) change matrix stiffness

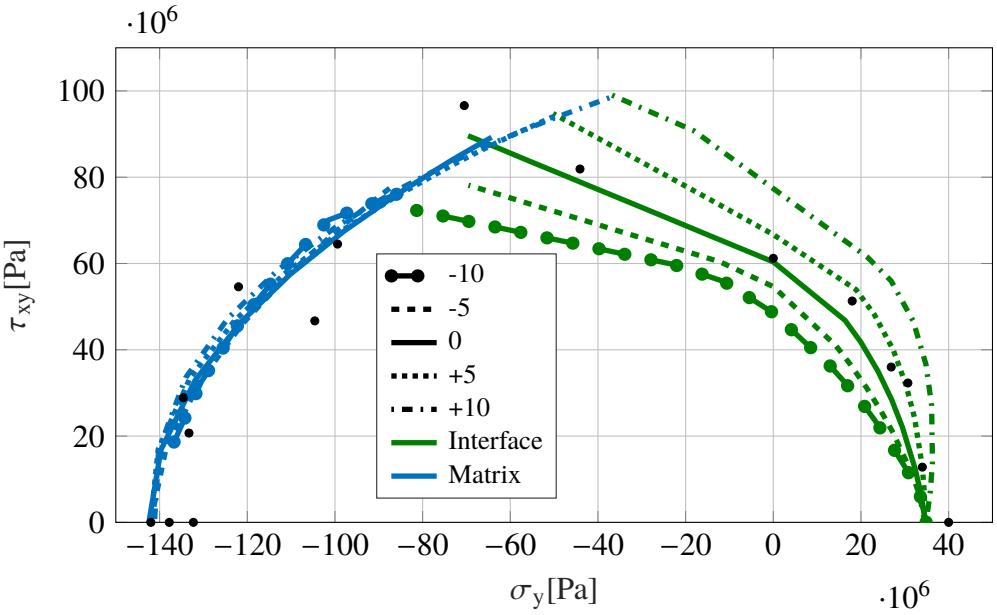

Figure 8.9. Parametric study for E-Glass LY ($\sigma_y - \tau_{xy}$) change composite orientation

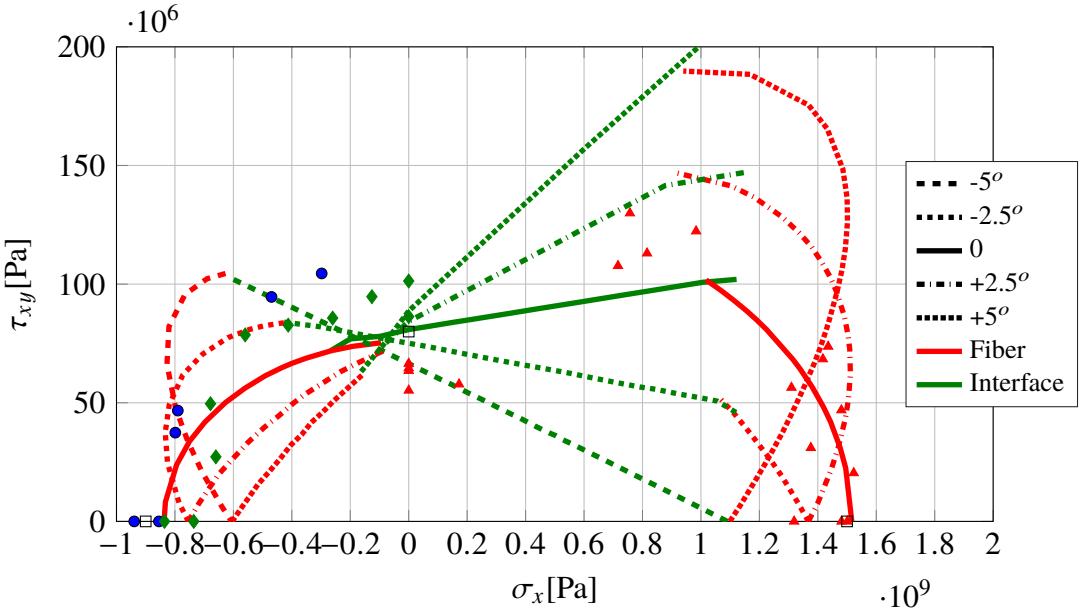

Figure 8.10. Parametric study for T300 ($\sigma_x - \tau_{xy}$) change composite orientation

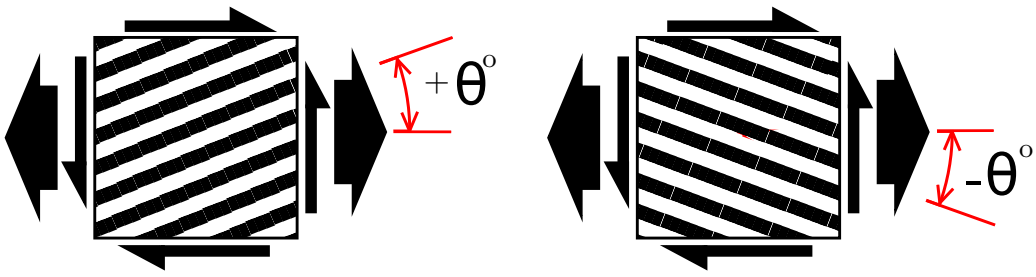

(a) Positive Rotations (b) Negative Rotations

Figure 8.11. Small angle effect

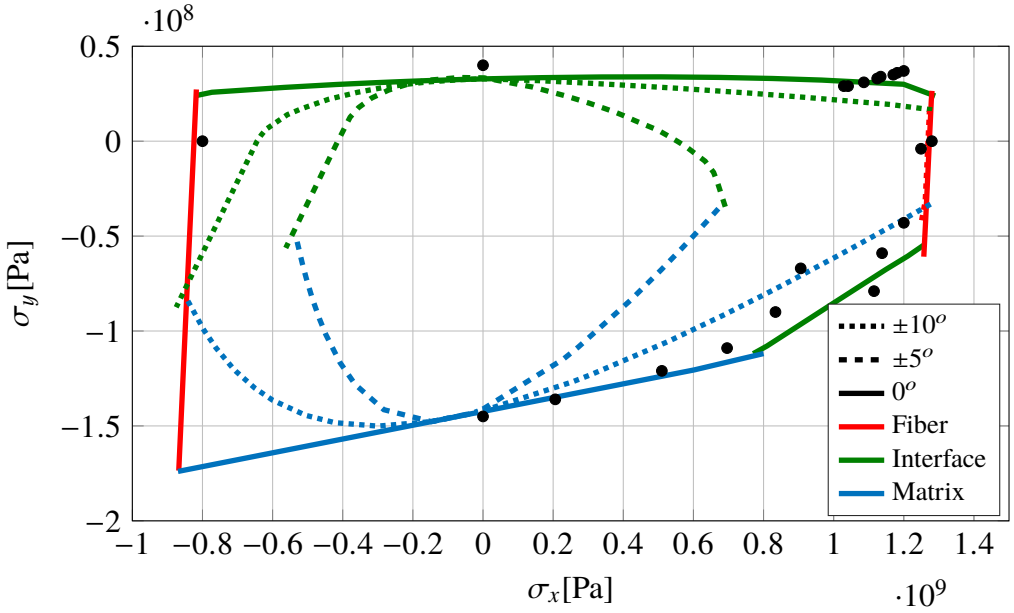

Figure 8.12. Parametric study for E-Glass MY ($\sigma_x - \sigma_y$) change composite orientation

CHAPTER 9:
Conclusion and Additional Work

9.1 Conclusion

The multiscale method for fibrous composites was first defined, and its computation was adapted to a finite element user material. Using experimental data as a guide, the outputs from the computation of the model were observed in stress-space. They were then combined to generate a separate mode failure criteria that shares same functional forms with previous criteria. These criteria are unique in that they use additional geometric considerations as well as calculations made possible by the multiscale method to account for more realistic failure modes. The proposed failure criteria, unlike most criteria discussed in Sun et al. [1] and Hinton et al. [10] successfully reproduces features in experimentally derived failure envelopes in the three sress planes and is easily used for many different composites of varying properties.

Initial failure in a complex structure may not lead immediately to complete failure of the structure, but rather to a gradual degradation. For this purpose, the failure criteria was combined with a logical framework that postulated potential degradations to individual portions of a composite. This degradation model then used the multiscale model to recalculate the stiffness properties of a composite. The failure model and degradation framework combine to form a flexible composite analysis tool.

The analysis tool proposed can calculate macro-level composite properties, check for local failures, and degrade the properties if failure is indicated. The failure model and framework discussed, distinct from other methods, is comprehensive. It forms a single coordinated method that estimates composite properties from constituent properties, estimates composite strengths based on constituent strengths and experimental data, identifies failure initiation, and degrades material properties based on failure.

The failure and degradation model was then implemented in Fortran so it may be used in finite element software as a user-defined material. As such, the multiscale method reports the undamaged material properties for the construction of the elemental stiffness matrix.

While not computationally optimal, the method carries a small computational overhead and is simply implemented.

The multiscale failure and degradation model was then tested using data from the World-Wide Failure Exercise which afforded an enormous set of data using varied materials and varied loading conditions. Against this data the model provided a reasonable representation of the failure of the subject composite, both uniaxial and laminated. For additional validation, filament wound cylinders were constructed and destructively tested. These tests were then modeled with finite elements so that stress-strain data and final failure values predicted by the multiscale failure and degradation model could be compared with additional experimental results.

In the course of these experiments, novel experimental methods and data processing schemes methods were devised. These methods included improvements to test specimen construction, the joining of data collected on unconnected measurement systems, as well as the construction of devices that enable the collection of data during many-channel experiments. Lastly, observations during these experiments regarding the placement of strain gauges on composite samples and best-practices for successful tests as well as areas for further research were presented.

The failure model also enables a user to conduct what-if analyses to determine a composite's response to changed parameters. The model was used for a simple parametric study in which the input constituent properties were altered, showing the variability of and the sensitivity of the model to the variation of the properties of the composite. Analyses such as this can enable a designer to better select composite reinforcement and matrix combinations as well as layup angles in a structure to optimize a design's performance.

9.2 Additional Work

The work described here could benefit from additional explorations and improvements, coding efficiencies, validation of assumptions by experiment, and exercising the model with additional modeling scenarios.

Applicability

This model and the UMAT derived from it appear to perform successfully while analyzing uniaxial and multi-angle continuous fibrous composites, however, the range of applicability of this model needs to be better understood such that it can be used in appropriate situations when it will the appropriate failure model to use

Computational Improvements

The current form of the UMAT, while functional, is likely not computationally efficient. The current form of the upscale/downscale formulation uses a linear algebra solving routines to extract the downscaling matrix. Efficiencies may be obtained by including an included subroutine that solves for the downscaling matrix rather than using the linear algebra library function, perhaps requiring less computational overhead. In addition to exploring whether alternative functions would yield improvements, the relationship matrix is a sparse matrix. Sparse matrix solvers may also provide improved performance.

More improvements to the UMAT would be a minimization of branching inside the subroutine. The current form has a significant amount of branching due to the `if...then` statements that are used for detecting and accounting for failures in the composite's integration point. The minimization or elimination of this branching would be required to modify the UMAT for use as a subroutine in Abaqus' explicit solver which requires that the UMAT be vectorized—a VUMAT.

The sum of the UMAT's computations may also be done *a priori*. Intact and damaged downscaling matrices and constitutive relationships can be calculated as part of model pre-processing, and stored for later access by the subroutine rather than computing these values at each integration point and each loading increment. Initial explorations using this technique were unsuccessful; however, it could prove a benefit for large models.

Validation of the assumptions by experiment

The plots of laminated composites included potential intermediate failures of plys at levels of low loading as compared to the ultimate failure. It is unknown whether this indication is actual or not. Some failure models are based on the accumulation of microcracks in a composite, perhaps this indication is the beginning of the formation of microcracks. In order

to explore this assumed behavior, a laminated composite beam could be constructed and loaded prior to ultimate failure, but beyond the assumed intermediate failure load. After this loading, nondestructive testing (ultrasonic, radiographic, acoustic, shearographic) could be conducted to determine if intermediate failures are present, and attempt to quantify them.

Real Structure Damage Detection

Finite element models of composite structures can be used in conjunction with real-world testing to localize structural damage as proposed by Gordis [32]. This damage detection method could potentially be used as a non-destructive method for determining composite intermediate failures such as those discussed in Chapter 6. Laminated composite beams or tubes could be constructed and stressed to a level higher than where intermediate failures are predicted, but short of ultimate failure. Once these potentially compromised specimen are prepared, the method described in Gordis as well as Bouwense [33] could be used to determine whether the failures are present or not.

Additional Parametric Studies

Additional studies could be conducted that examine sensitivity to failure 'anchor points' as input data. It is important to know how and how significantly an envelope changes for varying input values of $\varepsilon^f_{u,t}$, $\varepsilon^f_{u,c}$, ε^m_t, ε^m_c, τ_u, $\sigma_\perp$.

Modeling of Alternate composites

The failure model can be extended for use in composites other than uniform uniaxial composite and laminated composite with single orientations. The model, since it is implemented on the "material" level can be used very flexibly. For instance, chopped strand mat could be modeled using randomized orientations of the UMAT material model.

The model can also be validated for its applicability to woven composites. Kwon and Altekin [31] discuss woven composites in the context of multiscale modeling, the multiscale failure model would likely be able to be tailored for use in a composite textile application.

Modeling of Complex Structures

Additional exploration of the multiscale method and the failure model should be conducted using additional benchmarking problems such as structures with more complex features.

Classic benchmark problems including panels with holes and panels with stiffeners can be modeled using the multiscale failure model to further explore its applicability. These benchmark problems form an essential step to using the method and model for more comprehensive composite structural analysis.

In addition to structures with planned features such as holes and stiffeners, structures with inclusions and delaminations can be modeled in finite element software. Tests can be made with the multiscale failure model and finite element simulations of structures with inclusions using cohesive contact, crack propagation and element deletion.

Temperature Effects

Thermal stresses in composites are included in Kwon and Kim [13], and can be implemented in the UMAT devised for this research. Additional parametric studies can be conducted to determine the impact that temperature changes have on the prediction of a failure envelope. Additional experiments can be conducted to compare the prediction of the multiscale failure model to an actual composite subjected to higher and lower temperatures.

THIS PAGE INTENTIONALLY LEFT BLANK

APPENDIX:
Additional Contributions

A.1 Linking Unconnected Data Collection

Many data collection sources were used during the quasi-static tests described in Chapter 7. In order to link the varied data collection systems, all of which are collecting data at disparate rates and unsynchronized times, the "two plateau" method was devised. It relies on a custom program of a material testing frame that instructs the frame (Instron, MTS, SATEC, etc.) to impose on a sample two chosen loads in the lower portion of the elastic range of a sample. The two load plateaus were held for a specific time, usually 10 or 15 seconds each. Each of the data collection devices: the Instron load cell, surface applied strain gages, and digital image correlation (DIC) all show the plateaus, and can therefore be linked using the four-points caused by the plateaus and the halt times. Using the corner in the data caused by the halt in load application, a first "zero" time reference can be obtained, aligning the data in time. The length of the plateau of data can be used to validate the data sampling rate and similarly used to up-sample or down-sample by simple or interpolative means any or all of the now-correlated data. The second plateau offers two more points against which to correlate or validate the correlation. These second points prove useful if the first two plateau corners are obscured or unclear.

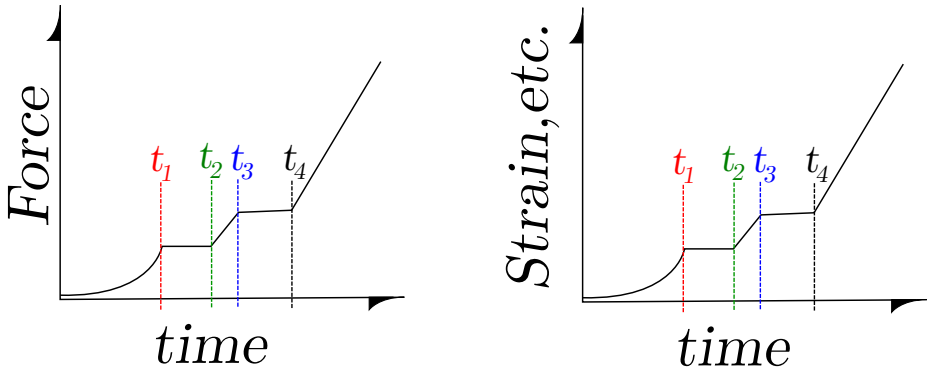

Figure A.1. Merging data from uncorrelated sources

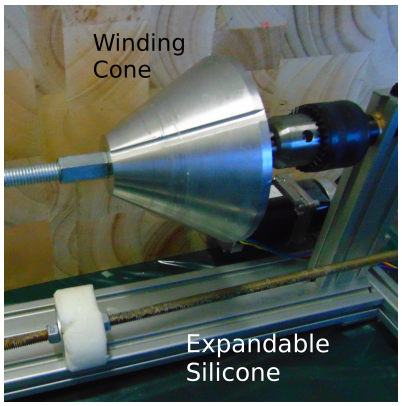

Figure A.2. The 60-degree cone and expandable silicone holder

A.2 Winding Machine Improvements

A.2.1 Winding Mandrel Cones

To increase the flexibility of the machine such that it can accommodate many winding mandrels with a minimum of equipment, 60-degree cones were manufactured for the winding axis. Winding mandrels were machined with matching 60-degree interior tapers. One of the mandrel cones is also machined with a keyway which accepts a set-screw from the mounted mandrel. This keyway–set-screw arrangement prevents the mandrel from slipping on the cone during winding. The cone is shown in Figure A.2.

A.2.2 Expandable Silicone Holders

For mandrels that cannot be mounted on the winding cones described above, silicone plugs can be cast in the appropriate shape for the inner portion of the mandrel. The silicone plugs can be made using a combination of normal silicone sealant and cornstarch to accelerate the sealant curing. These plugs can be compressed between fender washers on screws or threaded rod such that they hold the interior of the mandrel with friction. The holder is also pictured in Figure A.2.

A.3 Cutting Composite Cylinders Accurately

The cylinders manufactured at NPS were required to be cut accurately (perpendicular to the axis and of accurate length) while minimizing fiber tearout. The author devised a method

where the cylinders would be held on a more rigid cylinder whose outer-diameter provides a clearance fit with the inner-diameter of the cylinder to be cut, called a cutting-back. The cutting back was then centered to the rotation of the lathe. To ensure that the cylinder does not slip on the cutting back, the cylinder was wedged onto the back with shim stock.

Once the cylinder was in place, a diamond wheel attached to a die-grinder was held in the toolpost. The cylinder was then turned against the turning diamond wheel, increasing the surface speed during the cut. This method allows parting the cylinder sections while minimizing the opportunity to damage the parted cylinder, minimizing distortion while cutting and ensuring a perpendicular cut.

A.4 Neat Resin Dogbone Specimen Casting

Early efforts in this research were made to characterize the stress-strain response as well as ultimate strength of neat resin. To accomplish this, resin specimen were cast in ASTM D638 dogbone specimen molds. Some improvements were made to the process of casting and testing neat resin dogbones. To ensure decent surface finish as well as reduction in resin meniscus, plastic transparency cells are used both on the bottom and the top surfaces of the dogbone specimen. Transparency cells are best suited to this purpose since they have excellent surface finish, are relatively flexible, and do not distort under heat, unlike other plastics and wax papers.

An additional improvement is the inclusion of swatches of fiber reinforcement in the grip-sections of the dogbone specimens. This allows for the specimen to be gripped in a test machine with significant force without the addition of holding plates on the ends of the dogbones. Previous experiments adhered aluminum shim stock to the ends of the neat samples, requiring an additional step prior to destructive testing. Samples of the dogbones are pictured in Figure A.3.

A.5 High-Data Rate Data Acquisition

In order to enable the acquisition of strain gauge data for many strain gauges in a single experiment NPS/LLNL acquired a National Instruments PXIe system. This system is a high data rate differential analog voltmeter. This differential voltmeter enables the use of a Wheatstone bridge circuit to measure strain. To use this high data-rate acquisition, two

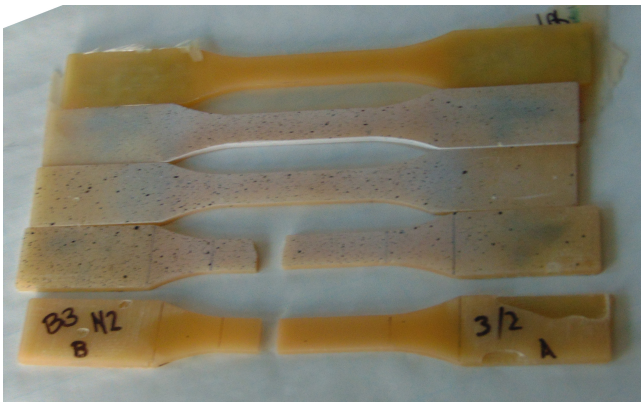

Figure A.3. Neat resin dogbones cast with fiber swatches

8-channel Wheatstone bridge completion modules were built to enable the connection of the strain gauges and the balancing of the circuit.

After initial explosive testing with strain gauges on steel cylinders, the PXIe system's sampling rate of 1.25M Samples per second is insufficient to record the event of interest. In order to improve data collection, a set of simple oscilloscopes (called BitScopes) were purchased. The BitScopes offered 16 differential channels and 10MS/s (as well as other benefits) for a very modest cost in comparison to alternative systems offering similar capture rates. One of eight BitScopes shown in Figure A.4.

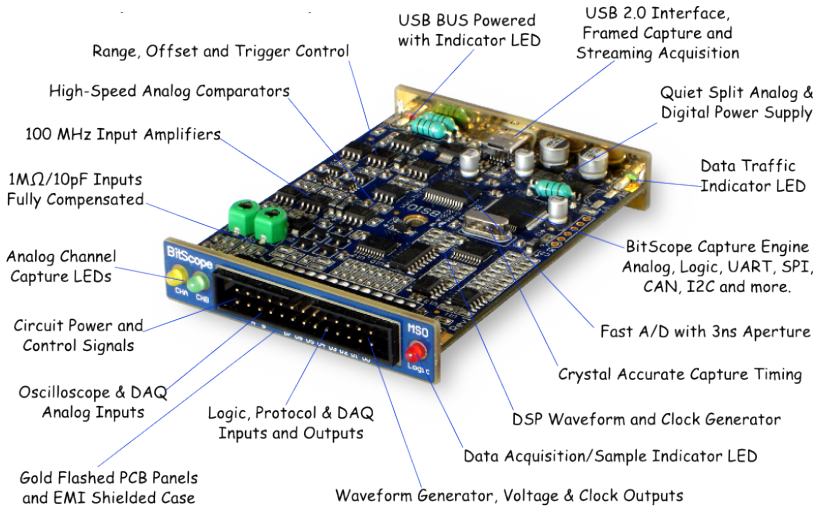

Figure A.4. Bitscope BS10. Source BitScope Designs [34].

Eight of these BitScopes were networked using Raspberry Pi computers and a network switch. This data acquisition system combines eight BitScope ocilloscopes each with two analog channels, eight digital channels and signal/clock generators. The complete system can be used as a high-rate data acquisition (DAQ) system with 16 analog and 64 logic channels at 20M samples per second. These scopes can be controlled remotely through a network as well as by scripts written in C, Pascal or Python, increasing their versatility. A picture of the complete DAQ is shown in Figure A.5.

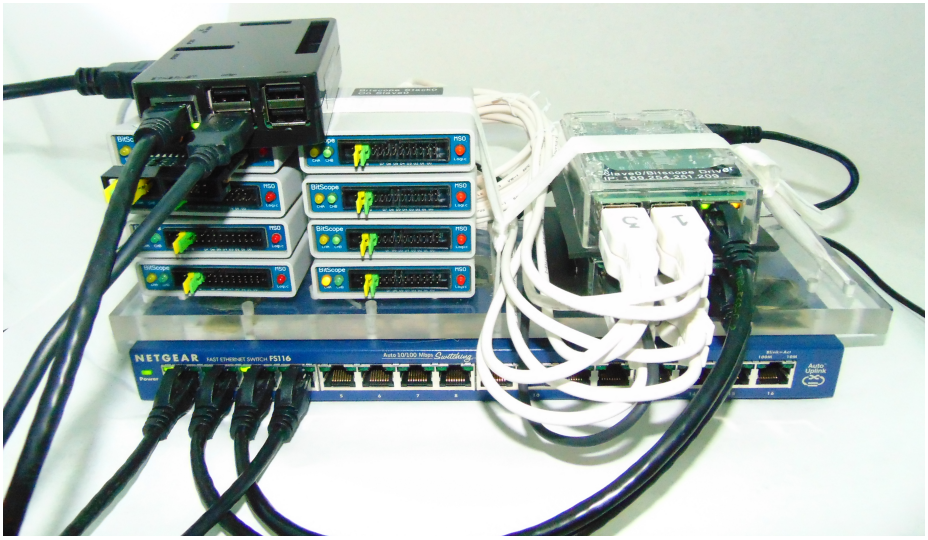

Figure A.5. The BitScope DAQ

The voltage resolution of the BitScopes is not sufficient for measurements on the order of 1mV across a strain gauge Wheatstone bridge in addition to the single-ended nature of the BitScope analog channels. To amplify the strain signals, reject common-mode noise in the bridge circuit and change the differential nature of the Wheatstone bridge measurement to suit a single-ended measurement device, an amplifier array of 16 Texas Instruments INA128P integrated circuit instrumentation amplifiers was assembled. This array is flexible and suitable for amplifying many differential measurement circuits with adjustable gain resistors built into the array. The amplifier array is shown in Figure A.6.

A.6 Shunt Resistor Calibration Box

To calibrate the Wheatstone bridge circuits prior to conducting the experiments, a calibration box was constructed containing a universal connection to precise resistors that are selected

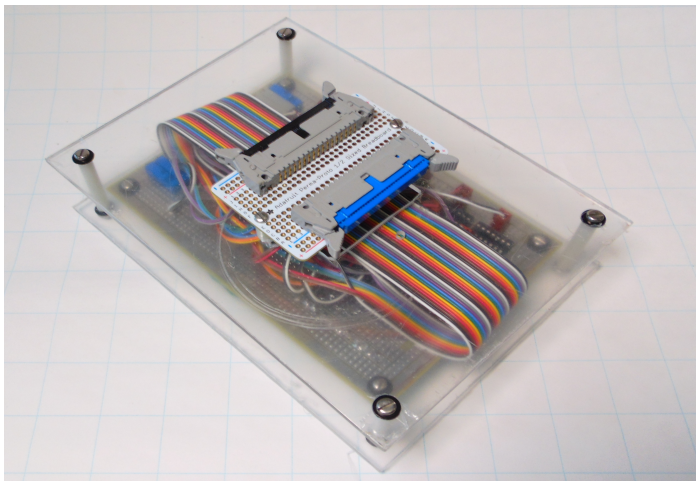

Figure A.6. The INA128P amplifier array

by means of a rotary switch. This switch enables the rapid change between shunt resistors in order to calibrate the circuit under test at five different simulated strain levels. The calibration box is shown in Figure A.7. The box enables switching between an open shunt and resistors simulating 500μ, 2,000μ, 4,000μ, 5,000μ, and 10,000μ for a foil strain gauge with a gauge factor of 2. For other gauge factors, the nomogram in Figure A.8 provides a convenient conversion. The governing equation:

$$\varepsilon_{simulated} = \frac{R_c}{GF\left(R_c + R_g\right)} \tag{A.1}$$

where R_c is the value of the shunt calibration resistor, GF is gauge factor of the strain gauge, and R_g is the resistance of the strain gauge being shunted. The shunt calibration prior to an experiment allows the expected bridge voltages for five different strain levels to be measured for later comparison and validation of experiment data, as well as an in-circuit verification of the resistances of the gauge leads using the voltage-to-strain relationship:

$$\varepsilon = \frac{4\frac{V_b}{V_e}}{GF\left(1 + 2\frac{V_b}{V_e}\right)}\left(1 + \frac{R_l}{R_g}\right) \tag{A.2}$$

where V_b is the voltage measured between the bridge arms, V_e is the bridge excitation voltage, GF is the foil gauge's gauge factor, R_l is the resistance of the strain gauge leads, and R_g is the resistance of the strain gauge.

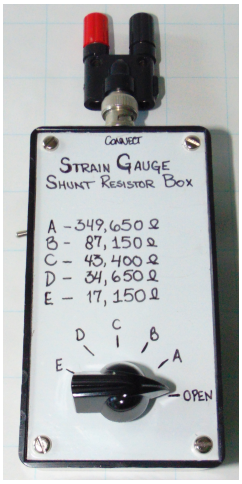

Figure A.7. The shunt calibration resistor box

A.7 High Strain Rate Expander

Additional high-strain rate cylinder burst experiments can be conducted with an apparatus similar to the quasi-static cone-wedge device. The expander would have four quarter-cylinder expander pieces which mate with pyramidal drivers that, when compressed, bear on interior faceted surfaces in the quarter-cylinders, providing a moderately uniform interior pressure.

This device would be sized such that it fits in a split Hopkinson bar test device. The expander would need to be manufactured from a similar material as the Hopkinson split bars and have a hardness marginally less than the incident and transmitted bars such that the expander does not damage the Hopkinson test machine.

Specimen in this test device are expected to be fiber-wound cylinders approximately the diameter of the Hopkinson bars, however they could be any conceivable size or material.

A.8 High Strain Rate Dogbone Mold

In anticipation of conducting strain-rate sensitivity measurements for composites, a mold for Hopkinson Bar dogbone specimen was constructed from aluminum plate. This mold can be used for either neat resin samples or for carefully lain uniaxial samples. The mold is pictured in Figure A.10.

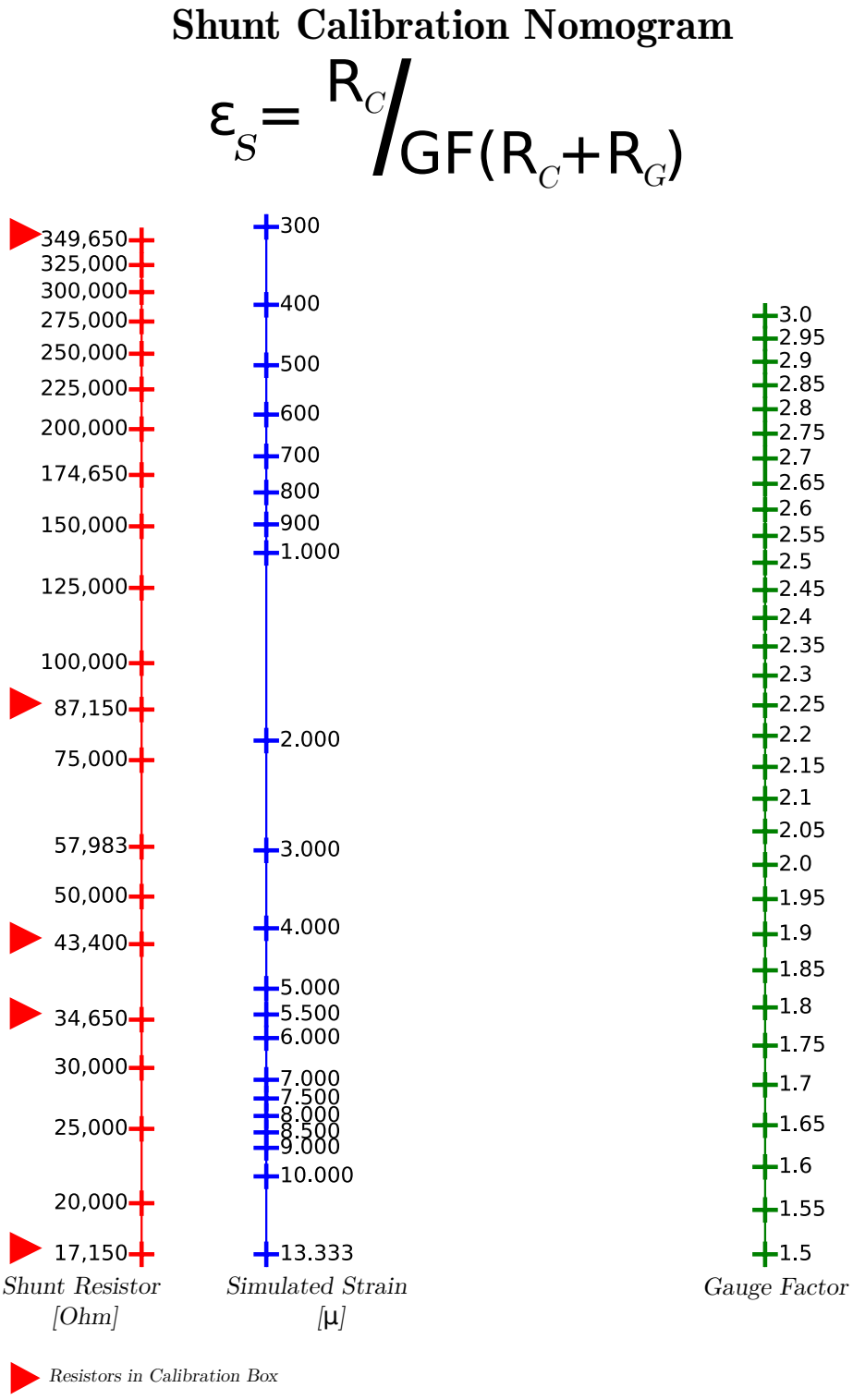

Figure A.8. Nomogram for shunt calibration of 350Ω strain gauge circuit

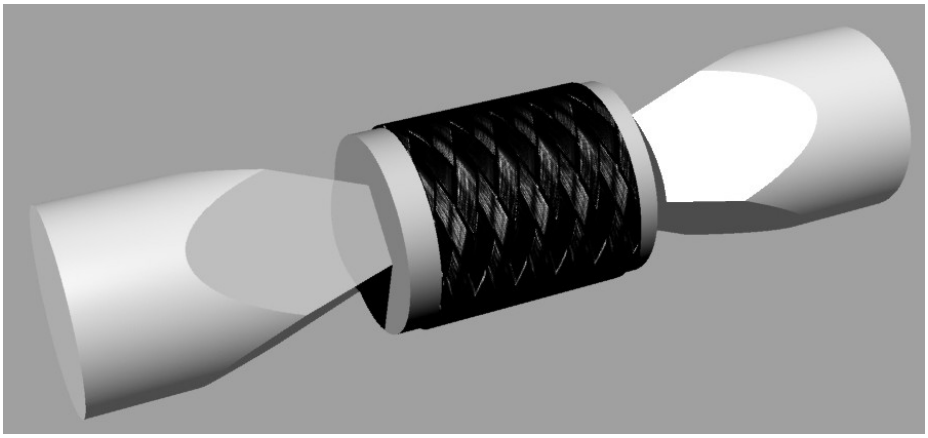

Figure A.9. High strain-rate cylinder expander

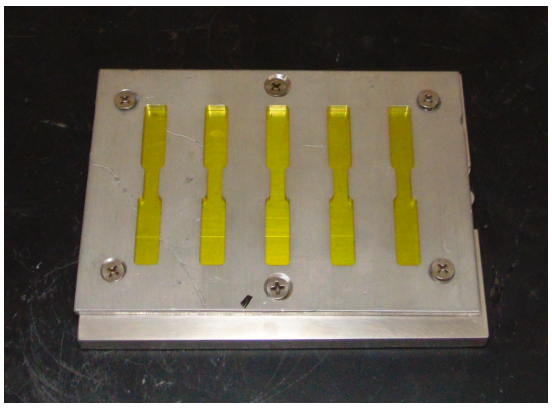

Figure A.10. Hopkinson Bar dogbone mold

List of References

[1] C. Sun, B. Quinn, J. Tao, and D. Oplinger, "Comparative evaluation of failure analysis methods for composite laminates." Purdue University, School of Aeronautics and Astronautics, DOT/FAA/AR-95/109, May 1996.

[2] S. W. Tsai and E. M. Wu, "A general theory of strength for anisotropic materials," *Journal of Composite Materials*, vol. 5, no. 1, pp. 58–80, Jan. 1971.

[3] Z. Hashin and A. Rotem, "A fatigue failure criterion for fiber reinforced materials," *Journal of Composite Materials*, vol. 7, no. 4, pp. 448–464, Oct. 1973.

[4] Z. Hashin, "Failure criteria for unidirectional fiber composites," *Journal of Applied Mechanics*, vol. 47, no. 2, pp. 329–334, June 1980.

[5] C. Chamis, "Simplified composite micromechanics for predicting microstresses," *Journal of Reinforced Plastics and Composites*, vol. 6, pp. 268–289, July 1987.

[6] P. Gotsis, C. Chamis, and L. Minnetyan, "Prediction of composite laminate fracture: Micromechanics and progressive fracture," in *Failure Criteria in Fibre Reinforced Polymer Composites: The World-Wide Failure Exercise*, M. Hinton, A. Kaddour, and P. Soden, Eds. Oxford: Elsevier, 2004, pp. 98–120.

[7] G. González and J. LLorca, "Multiscale modeling of fracture in fiber-reinforced composites," *Acta Materialia*, vol. 54, no. 16, pp. 4171–4181, Sep. 2006.

[8] D. Robbins, "Efficient multiscale modeling of progressive failure in composite laminates," in *49th. AIAA/ASME/ASCE/AHS/ASC Structures, Structural Dynamics and Materials Conference*, 2008.

[9] T. Boghetti, C. Hoppel, V. Harik, J. Newill, and B. Burns, "Predicting the nonlinear response and progressive failure of composite laminate," *Composites Science and Technology*, vol. 64, no. 3-4, pp. 329–342, Mar. 2004.

[10] M. Hinton, A. Kaddour, and P. Soden, *Failure Criteria in Fibre Reinforced Polymer Composites: The World-Wide Failure Exercise*, M. Hinton, A. Kaddour, and P. Soden, Eds. Amsterdam: Elsevier, 2004.

[11] Y. W. Kwon and J. Darcy, "Failure criteria for fibrous composites based on multiscale modeling," *Multiscale and Multidisciplinary Modeling, Experiments and Design*, vol. 1, no. 1, pp. 3–17, Mar. 2018. Available: https://doi.org/10.1007/s41939-017-0002-8

[12] Y. W. Kwon and J. Berner, "Micromechanics model for damage and failure analyses of laminated fibrous composites," *Engineering Fracture Mechanics*, vol. 52, no. 2, pp. 231–242, Sep. 1995.

[13] Y. W. Kwon and C. Kim, "Micromechanical model for thermal analysis of particulate and fibrous composites," *Journal of Thermal Stresses*, vol. 21, no. 1, pp. 21–39, Jan. 1998.

[14] Y. W. Kwon and M. S. Park, "Versatile micromechanics model for multiscale analysis of composite structures," *Applied Composite Materials*, vol. 20, no. 4, pp. 673–692, Aug. 2013.

[15] A. M. Moncada, A. Chattopadhyay, B. A. Bednarcyk, and S. M. Arnold, "Micromechanics-based progressive failure analysis of composite laminates using different constituent failure theories," *Journal of Reinforced Plastics and Composites*, vol. 31, no. 21, pp. 1467–1487, Nov. 2012. Available: http://jrp.sagepub.com/content/31/21/1467

[16] Hexcel Inc, "HexPly(r) 8551-7 epoxy matrix," 2005. Available: http://www.hexcel.com/user_area/content_media/raw/HexPly_85517_us_DataSheet.pdf

[17] Hexcel Inc, "HexTow(r) IM7 carbon fiber," 2016. Available: http://www.hexcel.com/user_area/content_media/raw/IM7_HexTow_DataSheet.pdf

[18] Society of Automotive Engineers, *Composite Materials Handbook*. SAE International on behalf of CMH-17, a division of Wichita State University, 2012. Available: http://www.worldcat.org/isbn/9780768078138

[19] H. Miyagawa, C. Sato, T. Mase, E. Drown, L. T. Drzal, and K. Ikegami, "Transverse elastic modulus of carbon fibers measured by Raman spectroscopy," *Materials Science and Engineering: A*, vol. 412, no. 1, pp. 88–92, Dec. 2005. Available: http://www.sciencedirect.com/science/article/pii/S0921509305009603

[20] *Abaqus 6.13 User Manual*, Dassault Systemes Inc., 2015.

[21] A. C. Ugural and S. K. Fenster, *Advanced Strength and Applied Elasticity*, 4th ed. Upper Saddle River, New Jersey: Prentice Hall, 2003.

[22] S. Swanson, M. Messick, and Z. Tian, "Failure of carbon/epoxy lamina under combined stress," *Journal of Composite Materials*, vol. 21, no. 7, pp. 619–630, July 1987.

[23] J. Jordan, J. Foley, and C. Siviour, "Mechanical properties of EPON 826/DEA epoxy," *Mechanical Time-Dependent Materials*, vol. 12, no. 3, pp. 249–272, Sep. 2008.

[24] Toray Carbon Fibers America Inc., "T700S data sheet, technical data sheet CFA-005," Online. Available: www.toraycfa.com/pdfs/T700SDataSheet.pdf

[25] TCR Composites Inc., "UF3325 TCR resin technical data sheet TCR DS-0003," Online. Available: www.tcrcomposites.com/TechDataSheets/TCR%20DS-0003%20UF3325%20TCRT%20Resin%20Data%20Sheet%20(Rev%2013).pdf

[26] A. Skudra, "Micromechanics of failure of reinforced plastics," in *Failure Mechanics of Composites*, vol. 3, G. Sih and A. Skudra, Eds. Amsterdam: Elsevier, 1985.

[27] D. Cohen, "Multi-axial composite tube test method," *ASTM Special Technical Publication 1416*, pp. 17–29, Jan. 2002.

[28] U. Hütter, H. Schelling, and H. Krauss, "An experimental study to determine failure envelope of composite materials with tubular specimens under combined loads and comparison between several classical criteria," in *NATO AGARD Conference Proceedings*, no. 163, Oct. 1974, pp. 3.1–3.11.

[29] C. Lissenden, C. Pindera, and C. Herakovich, *Response of SiC/Ti Tubes Under Biaxial Loading in the Presence of Damage*. New York, NY: American Society of Mechanical Engineers, 1992, pp. 73–90.

[30] T. D. Ponshock, "Design and analysis of an experimental setup for determining the burst strength and material properties of hollow cylinders," M.S. thesis, NPS, Monterey, CA, USA, 2015.

[31] Y. Kwon and A. Altekin, "Multilevel, micro/macro-approach for analysis of woven-fabric composite plates," *Journal of Composite Materials*, vol. 36, no. 8, pp. 1005–1022, Apr. 2002.

[32] J. Gordis, "Artificial boundary conditions for model updating and damage detection," *Mechanical Systems and Signal Processing*, vol. 13, no. 3, pp. 437–448, Oct. 1999.

[33] M. D. Bouwense, "Experimental validation of model updating and damage detection via eigenvalue sensitivity methods with artificial boundary conditions," M.S. thesis, NPS, Monterey, CA, USA, 2017.

[34] BitScope Designs, MetaChip Pty. Ltd. New South Wales, Australia. [Online]. Available: www.bitscope.com

THIS PAGE INTENTIONALLY LEFT BLANK

Initial Distribution List

1. Defense Technical Information Center
   Ft. Belvoir, Virginia

2. Dudley Knox Library
   Naval Postgraduate School
   Monterey, California